Infrared Photonics for High-Power and Tunable Applications

By

Gregory Reid Holdman

A dissertation submitted in partial fulfillment of the requirements for the degree of

Doctor of Philosophy
(Physics)

at the
University of Wisconsin-Madison
2022

Date of final oral examination: May 6, 2022
This dissertation is approved by the following members of the Final Oral Committee:
Victor W. Brar, Professor, Physics
Mikhail A. Kats, Professor, Electrical and Computer Engineering
Deniz D. Yavuz, Professor, Physics
Jennifer T. Choy, Professor, Engineering Physics

Abstract

Metasurfaces are a new class of optical component that stand to replace conventional optics in many applications. They allow for miniaturization and improved performance. In this thesis, I discuss two projects on the topic of metasurfaces. The first is a highly-reflecting, low-absorption silicon-silica metasurface that could be used as a laser sail to deliver a deep space probe to Alpha Centauri. The thermal stability of the metasurface during the acceleration phase is investigated. It is shown that the nonlinear and temperature-dependent absorption of Si causes thermal runaway to occur. The second project is the development of a frequency-tunable narrowband infrared thermal emitter. Today's sources of tunable MIR light are bulky and expensive. At the same time, there are many applications that would be significantly improved with cheaper or miniaturized sources. In this thesis, I discuss the design, fabrication, and measurement of such a device. By incorporating graphene into a dielectric metasurface, we are able to take advantage of the physics of bound states in the continuum to theoretically show that such a device could perform as required for these applications.

To my parents Donna and James, my sister Laura, and my partner Alexandria.

Acknowledgements

I would first like to thank Victor Brar for his support during my degree. Though he gave me a large amount of autonomy in these projects, his ideas were crucial to their completion. He also taught me an incredible amount about doing great scientific work.

Thank you to Mikhail Kats for advising our work on the laser sail paper and allowing the use of his FTIR spectrometer. These works would not have been possible without that support.

Thank you to Joel Siegel for being someone I could talk to about any technical problem. By learning the topics we studied at the same time, I believe it brought us both to a higher level of mastery.

Thank you to Gabriel Jaffe for being a phenomenal partner on both of our projects. He was able to take over the fabrication any time I could not. Good luck on your career goals, Gabriel!

Thank you to Margaret Fortman for performing the graphene transfers. It is always difficult to have tasks that randomly take your focus away from your own work, but you made another person's work possible. It is truly appreciated.

Finally, I would not have finished this degree were it not for my partner Alexandria. Her unconditional support and understanding kept me going over the four years we have known each other. She is one of the most important reasons why this thesis exists and I have obtained my doctorate.

Table of Contents

Chapter 1

Introduction

Optics and photonics are both studies of the manipulation of light. Conventional optics is generally based on a few ideas: differential phase propagation through a medium with a refractive index higher than air (e.g. lenses), specular reflection (e.g. mirrors), and linear filters and polarizers. It has the capability to manipulate the direction, phase, amplitude, and polarization of light along with other properties. This approach has been enormously successful over the past few hundred years. However, with the maturity of the field, many of its limitations have been realized. Photonics, on the other hand, does not rely merely on the ideas of conventional optics. Rather, more complicated solutions to Maxwell's equations are utilized to move beyond these limitations. Solutions like plasmonic resonances in noble metals,[1] Mie resonances in dielectrics,[2] or collective nonlocal resonances in photonic crystals[3] distinguish photonics from its ancestor.

Some of the devices producing these effects are known as metasurfaces.[4] In this thesis, I will present two projects designing metasurfaces which operate in the mid-infrared region of the electromagnetic spectrum. The first project is a metasurface designed specifically for a high reflection and low absorption application. The second is a frequency-modulated narrowband mid-infrared thermal emitter, a device intended to fill a gap in technology which lasers have not been able to fill. This work describes the theory of operation of both of these metasurfaces and, in the case of the second project, the fabrication and measurement of the device.

1.1 Metasurfaces

The optical properties of materials are captured in the quantities known as the *optical constants*, n and k. Together they form the complex refractive index

$$\tilde{n} = n + ik.$$

These constants are closely related to the relative permittivity ϵ and relative permeability μ via the relation

$$\tilde{n} = \sqrt{\epsilon\mu}.$$

In most materials, these constant are often considered to be fixed. The atoms in a material combine in crystalline or amorphous structures that induce particular electronic and phononic behavior that create ϵ and μ. The field of photonics has discovered that these properties are quite malleable in the far-field. Plasmonic and dielectric materials can be patterned on a length scale equal to or smaller than the wavelength of light in a way that imitates permittivities[2] and permeabilities [5] that are not found in any natural material. If the pattern occurs in a planar array, the device is known as a *metasurface*. The constituents of these patterns are sometimes called *meta-atoms* because they have resonances like the constituent atoms of the material that create ϵ and μ. The term *photonic crystal* is also often used. Although the distinction is somewhat blurred, in general photonic crystals have features on the scale of the wavelength and bestow spectral features rooted in the bandstructure, i.e. *nonlocal resonances*, while metasurfaces bestow features based on the individual contributions of many subwavelength structures, i.e. *local resonances*. Regardless, both of these devices are now being used to perform new optical achievements.

One particular application of metasurfaces is perfect reflection. Conventionally, perfect reflection has been achieved with the use of Bragg reflectors: alternating stacks of two materials with refractive indices n_1 and n_2 with the thickness of each layer tuned to one-quarter of the wavelength of operation. The reflection of such a stack in air is [get rid of

this]

$$R = \left[\frac{n_2^{2N} - n_1^{2N}}{n_2^{2N} + n_1^{2N}}\right]^2 \tag{1.1}$$

which approaches 1 as the number of layers N approaches infinity. However, metasurfaces offer such performance at a fraction of the thickness. A metasurface made of Si blocks only about 400 nm thick demonstrated $> 99\%$ reflection at a 1550 nm.[2] A Bragg reflector with the same performance would have a thickness over 1.5 μm.

Metasurfaces are also being studied for their thermal properties.[6] Coherent light, having a well-defined wavelength, polarization, direction, and phase, is often required for most useful applications. This is what has made lasers so successful. Thermal emission is the light emitted by a substance at a nonzero temperature and is often understood to have no well-defined polarization, wavelength (temporally incoherent), or direction (spatial incoherence). However, metasurfaces offer a means of tailoring thermal emission to endow it with coherence. One early example came from a silicon carbide grating that had been patterned into a periodic array of troughs.[7] The thermal emission was shown to have a narrow bandwidth and to emit in well-defined directions.

Metasurfaces need not only be static devices with unchanging optical properties. By incorporating materials with electrically tunable optical properties, one can create an *active metasurface*. Such materials include VO_2,[8] multiple quantum wells,[9] indium tin oxide,[10–12] and graphene.[13, 14] Often these materials are incorporated with the goal of actively changing the direction of thermal emisison, turning a resonance on and off,[9] or changing the frequency of a resonance[13, 14]. This thesis utilizes graphene to create an active metasurface.

1.2 Thesis Outline

This thesis is divided into two parts in order to present the results of two projects studying the thermal properties of metasurfaces.

Part I will cover the design of a Si/SiO_2 *laser sail* for the Breakthrough Initiative. The overarching goal of this project is to send a laser sail probe to Alpha Centauri at 20% the

speed of light. In order to accelerate it to such a speed, the sail will be illuminated by a GW-scale Earth-based laser. In the vacuum of space, the only mechanism for dissipating the heat absorbed by the laser is thermal radiation. I demonstrate, the nonlinear and temperature-dependent optical properties of Si can cause such a metasurface to enter a state of thermal runaway. This part of the thesis covers the mechanisms behind this phenomenon. The work is generally applicable to Si-based metasurfaces irradiated by a high-powered laser.

Part II covers the design, fabrication, and measurement of a frequency-modulated continuous-wave narrowband thermal emitter operating in the mid-infrared. Such devices are useful for free-space optical communication and trace gas sensing. Laser technology has not yet produced such a device with low size, weight, and power (low-SWaP). By using thermal emission, we hope to provide an alternative to this approach. The project utilizes the physics of bound states in the continuum (BICs) to achieve narrow resonances in a dielectric metasurface while graphene is incorporated as an optically tunable medium which will modulate the frequency of this resonance. Design, fabrication, and measurement of this device are discussed.

Part III is a reprint of early work performed in my doctoral work.[15] It is unrelated to metasurfaces, but concerns bilayer graphene. The work describes scanning tunneling spectroscopic measurements of gated bilayer graphene and the influence of the electrostatics on the resulting spectra.

Part I

Thermal Runaway in Silicon Laser Sails

This chapter has been published as a publication on arXiv as

Holdman G.R., Jaffe G.R., Jang M.S., Feng D., Kats M.A., Brar V.W. Thermal runaway of silicon-based laser sails. arXiv:211006185 [cond-mat, physics:physics] [Internet]. 2021 Oct 12 [cited 2022 Feb 25]; Available from: http://arxiv.org/abs/2110.06185

and is undergoing peer review at a journal.

Chapter 2

Main Text

2.1 Introduction

Sending probes to nearby star systems requires engineering spacecraft that can travel at relativistic speeds. Recently, the Breakthrough Starshot Initiative has proposed to design, construct, and launch 'laser sails' in order to achieve this goal, with an aim of sending a spacecraft towards Alpha Centauri at 20% the speed of light.[16] The proposed propulsion mechanism for these vehicles is the radiation pressure from a ground-based laser array on a reflective 'sail'. Many design challenges must be overcome before such a project can be realized, and amongst the forefront of them is designing the sail, which must have high reflectivity, low mass, low absorption, lateral and rotational stability, and thermal stability. Optical metasurfaces and photonic crystals are ideally suited structures for laser sails because they can be made highly reflective,[2] have low areal densities,[17] and can achieve self-correcting stability when accelerated by a high-powered optical beam.[18, 19] However, absorption of even a tiny fraction of the incoming laser radiation, which will be on the order of $10\,\mathrm{GW\,m^{-2}}$, poses major issues for sail thermal management because thermal radiation is the only mechanism for cooling in space. To prevent the sail from melting, it is crucial to choose materials that balance exceptionally low absorption coefficients at the drive laser wavelength (including the Doppler shift after the sail has accelerated) in the near infrared and high absorption coefficients in the midinfrared to far infrared to increase radiative cooling.[17, 20]

Silicon and silicon dioxide have emerged as two of the most attractive materials for laser sail designs based on metasurfaces, owing to the large contrast in their refractive indices, low material absorption at the proposed driving laser wavelengths ($\lambda_0 > 1.2\,\mu$m),[17] low mass densities, and potential for fast integration with existing industrial silicon fabrication infrastructure.[20, 21] In particular, one study of optimized sail structures found that a one-dimensional Si grating provided superior acceleration performance over any SiN_x metasurface.[22] Previous studies of Si/SiO_2 sails — where the SiO_2 is utilized for radiative cooling — with anywhere from 25 to 400 $\mathrm{GW\,m^{-2}}$ incident laser intensity have predicted equilibrium temperatures below the melting points of the constituent materials assuming that the absorption coefficient of both materials is $< 10^{-2}\,\mathrm{cm^{-1}}$.[20, 21] However, these works did not take into account two important factors that can significantly affect the thermal stability of the sail. First, silicon exhibits a strong temperature-dependent absorption coefficient due to bandgap narrowing that, for example, at a temperature of 800 K and wavelength of 1.55 μm, can reach $>4.5\,\mathrm{cm^{-1}}$.[23] This value is $\sim$6 orders of magnitude higher than at room temperature.[24] Second, two-photon absorption (TPA) introduces additional absorption in silicon with a TPA coefficient of $\beta = 1.35\,\mathrm{cm\,GW^{-1}}$ at 1550 nm, which would cause the absorption of the sail to increase with laser power even at low temperatures.[25] For laser-phased arrays operating at intensities on the order of $I_0 \approx 10\ \mathrm{GW\,m^{-2}}$, TPA adds about $1.35\times10^{-3}\,\mathrm{cm^{-1}}$ to the absorption coefficient of Si, well above any absorption measured in Si at room temperature for low laser intensities. In this work, we show that these two properties can cause thermal instabilities in the sail during its acceleration phase.

To investigate the limits of thermal stability, we analyzed a Si/SiO_2-based metasurface laser sail that is designed to have a reflection coefficient of >99% at the laser wavelength of 1.55 μm and that exhibits a low areal mass density of $<1\,\mathrm{g\,m^{-2}}$.[16] In order to model the thermal characteristics of the sail, we assembled detailed models of the spectral and temperature-dependent absorption coefficients of both Si and SiO_2 from literature sources and used these in our simulations. We then used full-wave, finite element simulations to calculate the precise temperature dependence of the emissivity and absorptivity, and we

balanced these two factors to determine the stable sail temperature. We found that, even when using the lowest absorption coefficients ever demonstrated on the wafer scale, this metasurface sail has no equilibrium temperature for laser intensities I_0 >4.8 GW m^{-2}. The mechanisms behind this are TPA in Si at low temperatures and free-carrier absorption augmented by a decreasing bandgap at high temperatures also in Si. For laser intensities I_0 <4.8 GW m^{-2} we found that the sail can exhibit a stable equilibrium temperature, but fluctuations above a higher unstable equilibrium temperature could lead to thermal runaway regardless. While any Si/SiO_2 sail will exhibit this behavior, we demonstrate that a design which lowers the electric field in the Si, and therefore reduces the total absorption, can provide significant improvements to this limit.

2.2 Sail and Material Models

A schematic of the metasurface laser sail design used in this work is shown in Figure 2.1. Our Si/SiO_2-based metasurface consists of 430-nm-wide by 450-nm-tall Si blocks on a 200-nm-thick SiO_2 substrate, with a total areal mass density of 0.96 g m^2. This structure is based on a previously published broadband perfect reflector geometry that uses Mie resonances to achieve perfect reflection.[2] For this work, we have re-optimized that structure to account for a finite-thickness silica layer, and achieved a reflectivity of 99.5 % at a driving laser wavelength λ_0 =1550nm and >95 % from 1350 nm to 1605 nm.

Our simulations included models of the complex refractive indices of both materials. We assumed a constant real refractive index of Re[n_{Si}]=3.42 for Si as the index varies very little over the wavelength range of interest 1-100 μm. The real refractive index of SiO_2 Re[n_{SiO_2}] has been extensively studied.[26] The imaginary parts of the refractive indices require more care. In order to calculate the equilibrium temperature of a laser-heated Si/SiO_2 metasurface sail, comprehensive models of the temperature and wavelength dependence of the Si and SiO_2 absorption coefficients $\alpha = 4\pi \mathrm{Im}[n]/\lambda$ are needed. These models must be valid in the range of the expected equilibrium temperatures spanning 50–800 K, and cover both the Doppler-broadened laser wavelength range of 1.55–1.90 μm and the bandwidth of the thermal emission

from 2–100 μm. We found no single literature source that provided absorption values over such a broad range of wavelengths and temperatures. We therefore assembled a composite absorption model for each material from multiple literature sources.

Our model can be seen in Figure 2.2. There are four different processes that contribute to the infrared absorption of Si. The total absorption, $\alpha_{Tot}(\lambda, T, I)$, at a particular wavelength λ, temperature T, and local intensity $I = c\epsilon_0|E|^2/2$, can be modeled as the sum of the absorption contributions from each absorption mechanism as

$$\begin{aligned}\alpha_{Tot}(\lambda, T, I) = \alpha_{BG}(\lambda, T) \ + \ \alpha_{FC}(\lambda, T) \ + \\ \alpha_{TPA}(\lambda, I) \ + \ \alpha_L(\lambda).\end{aligned} \tag{2.1}$$

Here, α_{BG} is the coefficient of the bandgap absorption caused by the excitation of electrons in the valence band into the conduction band, and α_{FC} is the coefficient of the free-carrier absorption, which involves the transfer of photon energy to thermally excited free carriers in conduction or valence bands. The two-photon absorption coefficient is α_{TPA}, and α_L is the coefficient for the lattice absorption through multiphonon processes.

The composite absorption model for Si that we developed includes tabulated values of the total absorption coefficient between 0.25–1.45 μm,[27] a free-carrier absorption model spanning 1.45–5 μm,[23] and a second free-carrier model for the range of 4–100 μm[28] for which we assume the intrinsic-carrier concentration follows the model of Couderc et al.[32] We also include the multiphonon absorption bands from 7–100 μm[29, 30] as well as tabulated coefficients for TPA which has a broad step near 2 μm.[25] The TPA process is a particularly important mechanism to consider when modeling metasurfaces designed to operate at high intensities. In Si at 300 K, the TPA at 1.55 μm is greater than the combined free-carrier and single-photon bandgap absorption for fluences >900 kW m^{-2}. Further information regarding interpolation between models and the fits to the multiphonon modes is available in the supporting information.

The amorphous SiO_2 absorption model we assembled includes the extensive collation of room temperature wavelength-dependent absorption measurements of SiO_2 glass in the range 0.015–100 μm.[26] The room-temperature values are used at all sail temperatures in our

models because the absorption of SiO_2 exhibits only a weak temperature dependence from 300–1100 K between 1–7 μm.[33–35] We note that the growth conditions, defect density, and concentration of hydroxyl groups are known to have a strong effect on the absorption of SiO_2 in the infrared and are responsible for the significant variation in the reported absorption of SiO_2 at 1.55 μm. Films of SiO_2 grown via wet oxidation of Si followed by a 24 hour dry oxidation at 1000 °C have demonstrated absorption as low as $4.1\times10^{-5}\,\mathrm{cm}^{-1}$ on the wafer scale.[31] This absorption value is three orders of magnitude smaller than the typical value of $2.4\times10^{-2}\,\mathrm{cm}^{-1}$.[26] Even lower values of absorption have been demonstrated in optical fibers, but have yet to be realized at the wafer scale. We refer to the above absorption coefficients at 1.55 μm as "Hero" and "Typical", respectively, and they are denoted in Figure 2.2 by grey diamonds. To our knowledge, the ultra-low Hero SiO_2 absorption has only been demonstrated in a single experiment.

2.3 Simulation of Metasurface Thermal Balancing

During the acceleration phase, the sail absorbs energy from the driving laser while the only mechanism for losing energy is thermal radiation. The absorbed laser power will raise the temperature of the sail until it reaches an equilibrium temperature T_i, at which point the absorbed intensity I_A and thermally emitted intensity I_E are equal. Perturbations may drive the sail above or below T_i, but if a rising temperature causes $I_E(T)$ to exceed $I_A(T)$, the equilibrium temperature will be stable because excess emission cools the sail. Likewise if $I_A(T)$ increases above $I_E(T)$ with T, then T_i is an unstable equilibrium as the sail absorbs more energy than it can emit and it undergoes thermal runaway. It is possible that $I_A(T) > I_E(T)$ for a large range, possibly even all values of T. In this case, the temperature will increase until the sail melts or is otherwise destroyed. In this work, we predicted the equilibrium temperatures of the sail in Figure 2.1a by calculating $I_A(T)$ and $I_E(T)$ for a large range of temperatures and then identified the T_i where $I_A(T_i) \approx I_E(T_i)$.

We computed the quantities $I_A(T, I_0)$ and $I_E(T)$ in different ways. Absorbed intensity $I_A(T, I_0)$ at the driving laser wavelength 1.55 μm was calculated by using a full-wave FDTD

simulation (Ansys Lumerical) to obtain the local field distribution, exporting the data, and performing the following volumetric integration:

$$I_A(T, I_0) = \frac{\omega_0}{A} \int \mathrm{Im}\{\epsilon[\omega_0, T, I(\boldsymbol{r})]\}|E|^2 dV. \tag{2.2}$$

where A is the area of the unit cell, $\omega_0 = 2\pi c/\lambda_0$, ϵ is the permittivity of the constituent materials, and $I(\boldsymbol{r})$ is the local intensity. The permittivity acquires a dependence on $I(\boldsymbol{r})$ in the Si due to TPA. For $I_E(T)$, it is computationally challenging to calculate the exact thermal emission of the metasurface structure using full-wave simulations given that light is emitted over a broad bandwidth (λ ~2-100 μm), over all angles, and with both s and p polarizations. Thus, to calculate $I_E(T)$, we approximated the Si layer as a material with an effective index $n_{eff} = F \times n_{Si}$ where $F = 430^2/670^2 \approx 41\%$ is the fill factor of the Si in our metasurface design, and n_{Si} is the bulk Si refractive index. This approach leverages the fact that the characteristic length scale of the metasurface is much smaller than the emission wavelengths. We confirmed the validity of this method by comparing full-wave simulations of the metasurface to the approximated structure for a few chosen angles (see Supplement). We then implemented a transfer matrix method to calculate reflection and transmission which were used to derive absorptivity $A = 1 - R - T$.[36] Emissivity was then calculated via Kirchhoff's law of thermal radiation, equating emissivity to absorptivity, and the overall thermal emission was calculated by integrating over the Planck distribution in wavelength, angle, and polarization.[6]

Figure 2.3(a-c) displays $I_A(T, I_0)$ and $I_E(T)$ for the total structure as well as the constituent materials. At all temperatures, SiO_2 dominates thermal emission and roughly follows a T^4 power law. When the metasurface is made with Hero SiO_2, an incident intensity of $I_0 = 1\,\mathrm{GW\,m^{-2}}$ yields two equilibrium temperatures of 189 K and 512 K with the former being stable and the latter unstable. Above 512 K, thermal runaway occurs as the sail absorbs more energy than it can emit. Increasing the incident intensity to $I_0 = 10\,\mathrm{GW\,m^{-2}}$, we found no equilibrium temperature exists in Hero SiO_2, and thermal runaway occurs at all temperatures. For metasurfaces using Typical SiO_2 and $I_0 = 1\,\mathrm{GW\,m^{-2}}$, the SiO_2 absorption

dominates over the TPA in Si at low temperatures. We found that the stable and unstable equilibrium temperatures are very close at 423 K and 477 K. This means a small fluctuation in incident intensity could put the sail into the thermal runaway region and cause it to melt. Figure 2.3d displays the difference in emissive intensity I_E and absorptive intensity I_A as a function of both T and I_0 for the case of Hero SiO_2. There is a large region where this value is positive indicating the sail will cool to the stable equilibrium temperature, provided the initial temperature is below the unstable equilibrium temperature. We found that no stable equilibrium temperature exists for I_0 >4.8 GW m^{-2} implying that the temperature will increase until it melts, evaporates, or otherwise fails.

The existence of a maximum laser intensity set by the thermal limits we calculate here also place limits on the maximum achievable acceleration of the sail. Laser sail designs in other works assumed I_0 ≈25 GW m^{-2},[20, 21] whereas our work demonstrates that a particular Si/SiO_2 metasurface sail will be limited to I_0 <4.8 GW m^{-2} using the best materials available. A commonly used figure of merit for sail performance is the smallest possible acceleration distance (AD) for a given incident intensity and target speed:[17, 22, 37]

$$AD = \frac{c^3}{2I_0}\rho \int_0^{\beta_f} \frac{h(\beta)}{R[\lambda(\beta)]} d\beta \tag{2.3}$$

where ρ is the sail areal density, $\beta = v/c$ is the velocity normalized to the speed of light and $h(\beta) = \beta/(1-\beta)^2\sqrt{1-\beta^2}$ accounts for relativistic corrections. We assume a constant laser intensity I_0 and use the reflection spectrum in Figure 2.1c, along with the areal density, to calculate the AD for the sail studied here, which we found to be 26 Gm for a laser intensity of $I_0 = 25$ GW m^{-2}. However, using a thermally limited laser intensity of $I_0 = 4.8$ GW m^{-2} yields an AD of 148.9 Gm, a penalty of a factor of ∼6. We note that our metasurface sail was initially chosen to maximize reflectivity at 1550 nm, not minimize the AD. However, as shown in the supplementary materials, a rudimentary optimization of this design for minimal AD can be performed by scaling the dimensions proportionally. We find that increasing the dimensions by 5% yields a slightly lower AD of 126.5 Gm, largely due to increased reflectivity over the Doppler-shifted wavelength range of the laser. Alternative designs that maintain

high reflectivity while minimizing the electric field concentration in the Si could potentially reduce AD further by allowing for higher laser intensities. This topic is explored further in the next section.

2.4 Thermal Balance of Bragg Reflector

As is clear from Figure 2.1b, the highly reflective metasurface we studied concentrates the incident field in the high index Si blocks. Considering that the two-photon nonlinear absorption in the Si scales as $|E|^4$, a design which concentrates the field outside of the Si would, theoretically, improve the thermal stability of the sail. A Bragg reflector, which operates by destructive interference of the electric field inside the structure, is an example of such a design.

In order to explore the comparative thermal stability of Bragg reflectors to dielectric metasurfaces we modeled Bragg reflector structures that consist of alternating layers of Si and SiO_2 of thicknesses 113.3 nm and 269.1 nm, respectively, corresponding to the quarter wavelength condition for 1550 nm light. The electric field magnitude of normally incident 1550 nm light is shown in Figure 2.4a for 1 to 4 layers of Si/SiO_2. In contrast to the metasurface, the Bragg reflector reduces rather than concentrates the field. Each successive layer also reduces the field by roughly an order of magnitude, so extra layers will not significantly add to the total absorption. The reflection spectrum is broadband for all layers (Figure 2.4b) and increases with the number of layers. Thus, the Bragg reflector is a strong candidate for providing low values of AD by allowing for large incident laser intensities.

We calculate the maximum intensity I_{Max} and resulting (AD) for 1 to 4 layers using the methods described in the previous section. An example of the calculation of I_{Max} for one layer is shown in Figure 2.4c. Our results are shown in Table 2.1. Increasing the number of layers raises the areal mass density proportionally while only slightly raising I_{Max} and reflection. We therefore find that one layer is optimal providing an AD of 18.4 Gm.

We note that while the Bragg reflector improves the performance of Si/SiO_2 sails in terms of minimum AD, this is achieved by allowing for order-of-magnitude larger laser intensities,

Layers	Density [$\mathrm{g\,m^{-2}}$]	I_{Max} [$\mathrm{GW\,m^{-2}}$]	AD [Gm]
1	0.98	38.1	18.4
2	1.96	39.5	20.7
3	2.94	40.9	27.0
4	3.92	43.6	33.0

Table 2.1: Resulting areal mass density, I_{Max}, and AD for various numbers of layers of the Bragg reflector.

which would significantly raise the overall cost of the project. In fact, the optimal single layer Bragg design is only ∼50% reflective, and would waste large amounts of power. Moreover, a Bragg reflector design would not be compatible with passive stability schemes that are possible with metasurface sails[18, 19, 38, 39] and would not enable the use of flat optics for focusing of communication lasers to relay signals back to Earth, as has been proposed for metasurfaces. [18]

2.5 Discussion

The thermal runaway of the sails that we predict at high temperatures is caused by the increasing free-carrier absorption of Si with temperature. This absorption mechanism strengthens with increasing temperature because the band gap of Si shrinks and the population of thermally excited carriers increases. At low temperatures, if the low-loss Hero SiO_2 is used, TPA in Si dominates the absorption of the sail. Since TPA increases linearly with incident power, the absorbed power of the sail increases with the square of the incident power, i.e. $I_A \propto I_0^2$. Strong TPA at low temperatures is sufficient to raise the temperature of the sail to the point where the increasing free-carrier and bandgap absorption cause a thermal runaway. In principle, it would be possible to avoid TPA by choosing a laser wavelength longer than $2\,\mu$m, but phonon-mediated absorption in both Si and SiO_2 will increase, as will free carrier absorption in the Si. Detailed modeling beyond $2\,\mu$m, however, is inhibited by a lack of

absorption data in Hero-quality SiO_2 and Si at those wavelengths. Below $2\,\mu$m, all laser sail designs containing Si must contend with TPA.Through the Bragg reflector example, we have shown that one approach to solving the thermal runaway problem may be to use a sail design that concentrates the electric field outside of the Si layer.

Our work provides an optimistic upper bound on the maximum intensity I_{Max} that a Si-based sail could survive. There are other effects that could increase the absorption of the sail, further reducing this maximum survivable intensity. For instance, strain is known to decrease the bandgap of silicon, which will significantly increase absorption at the proposed laser wavelengths.[40] In addition, dangling bonds at defects in Si exhibit strong absorption peaks in the midinfrared.[41] There is also the danger that small localized transient temperature fluctuations, caused by impact events with gas molecules and dust, could lead the entire sail into thermal runaway.[42]

The total emission of the sail could be increased to counteract the effects of TPA. Laser cooling of rare-earth ions[43], nanoparticle laminate films[44], and multiscale segmented designs [45] have been proposed. Additionally, the emission spectrum of coupled resonators has been shown to be highly tunable,[46] and such techniques could be applied to increase the emission of a sail incorporating SiO_2.

It is possible that light sails constructed of a different material, such as SiN_x, would not exhibit the thermal runaway behavior of Si sails. However, detailed studies of the absorption behavior of most materials at high laser intensities and high temperatures, including SiN_x, are lacking. In the case of Si_3N_7, TPA has been shown to be negligible at 1550 nm, yet exceeds that of Si at 1060 nm, another potential driving laser wavelength.[47] Additionally, some materials could exhibit effects not seen in Si, like stoichiometric instabilities, which could also lead to similar thermal runaway behavior despite reduced free carrier absorption and bandgap narrowing effects.[48] Thus, our results highlight the need to measure the optical constants of all candidate materials with ppm sensitivity in high-temperature and high-intensity conditions where non-linearities can occur.

We note that the constraints outlined in this work are emergent effects that occur in the

presence of high laser intensities, and thus do not eliminate Si/SiO_2 solar sails from being constructed. [42] In addition, the intensity constraint is well below the threshold needed for interplanetary laser sail missions.[16]

2.6 Conclusion

In this work, we demonstrated that a Si/SiO_2 metasurface floating in vacuum and exposed to a $1.55\,\mu$m laser with an intensity above a threshold I_{Max} will melt, regardless of starting temperature. Equilibrium temperatures will exist at lower incident laser intensities; however, a thermal runaway process will melt the sail if the sail temperature reaches the 400–500 K range. The use of high quality SiO_2 with low absorption will increase the thermal stability of the sail to a point, but ultimately the absorption will be dominated by two-photon absorption in Si. Thus, the potential for thermal runaway must be taken into account when designing a laser sail that incorporates a temperature-dependent absorptivity such as Si. It is possible that other candidate materials for the Breakthrough Starshot Initiative project could exhibit this behavior as well. Where the data is not available in literature, measurements must be performed to characterize the materials.

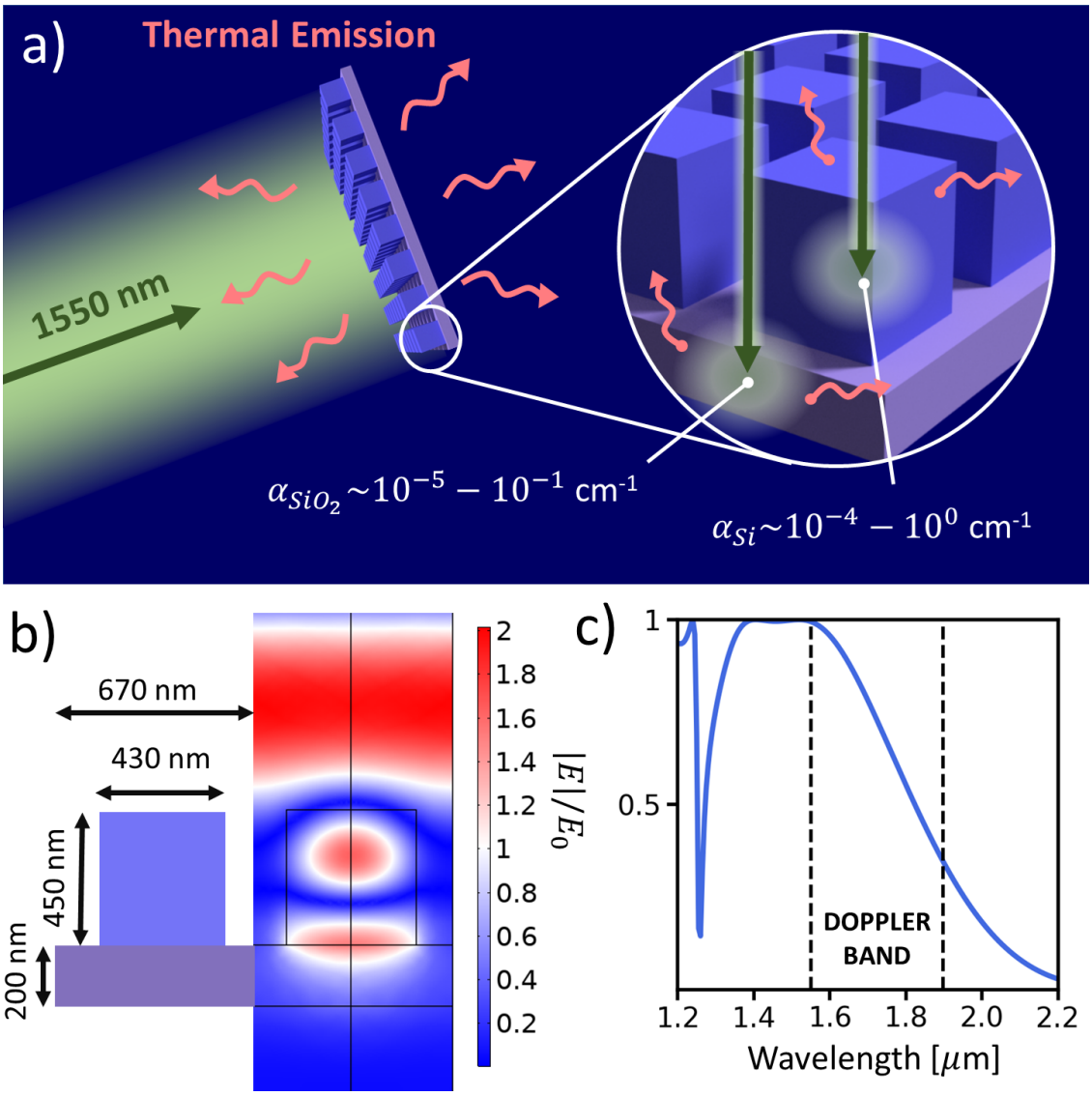

Figure 2.1: a) Laser-sail probe being accelerated toward Alpha Centauri. Laser light is absorbed in the structure, which can only cool via thermal emission. Absorption coefficients at 1.55 μm are labeled. There is wide variability in these materials for different qualities, temperatures, and intensities. b) Diagram of the metasurface used in this work consisting of 430-nm-wide by 450-nm-tall Si blocks (dark blue) with a pitch of 670 nm on a 200-nm-thick SiO_2 substrate (light purple). The colormap shows the electric field magnitude within the structure normalized to the incoming 1550 nm laser intensity. Note, field enhancement within the resonator causes the field intensity to exceed that of the incoming plane wave in localized regions. c) Reflection spectrum of the metasurface.

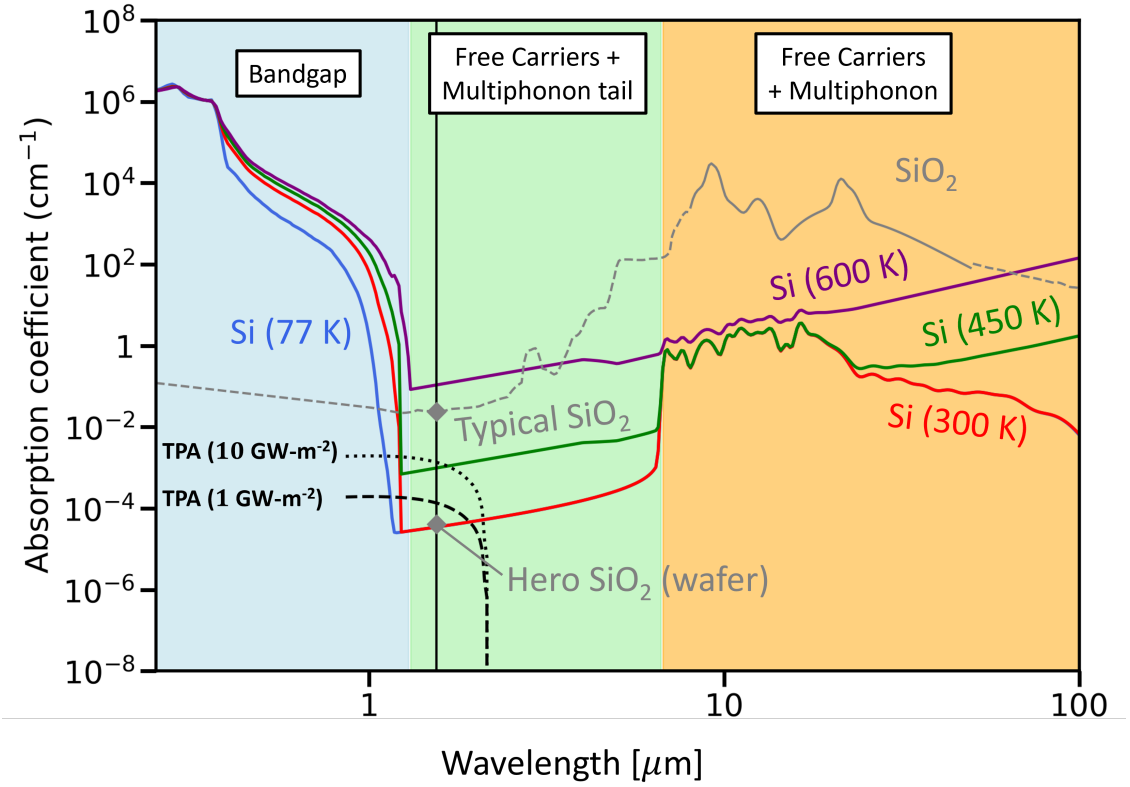

Figure 2.2: A composite model from multiple literature sources of the absorption coefficient of Si as a function of wavelength at various temperatures (colored lines) and amorphous SiO_2 at room temperature (grey line).[26] The blue, green, and orange shaded regions indicate the dominant absorption mechanisms for each wavelength range for Si. The model is composed of bandgap absorption,[27] free-carrier absorption,[23, 28] and multiphonon absorption.[29, 30] Two-photon absorption (TPA) at intensities 1 $GW\,m^{-2}$ and 10 $GW\,m^{-2}$ are included as dashed black lines.[25] The data point labeled "Hero" indicates the lowest demonstrated absorption value of SiO_2 at a wavelength of 1.55 μm in a wafer.[31] The vertical line indicates the laser wavelength of 1.55 μm. Further details regarding the Si composite absorption model are available in the supporting information.

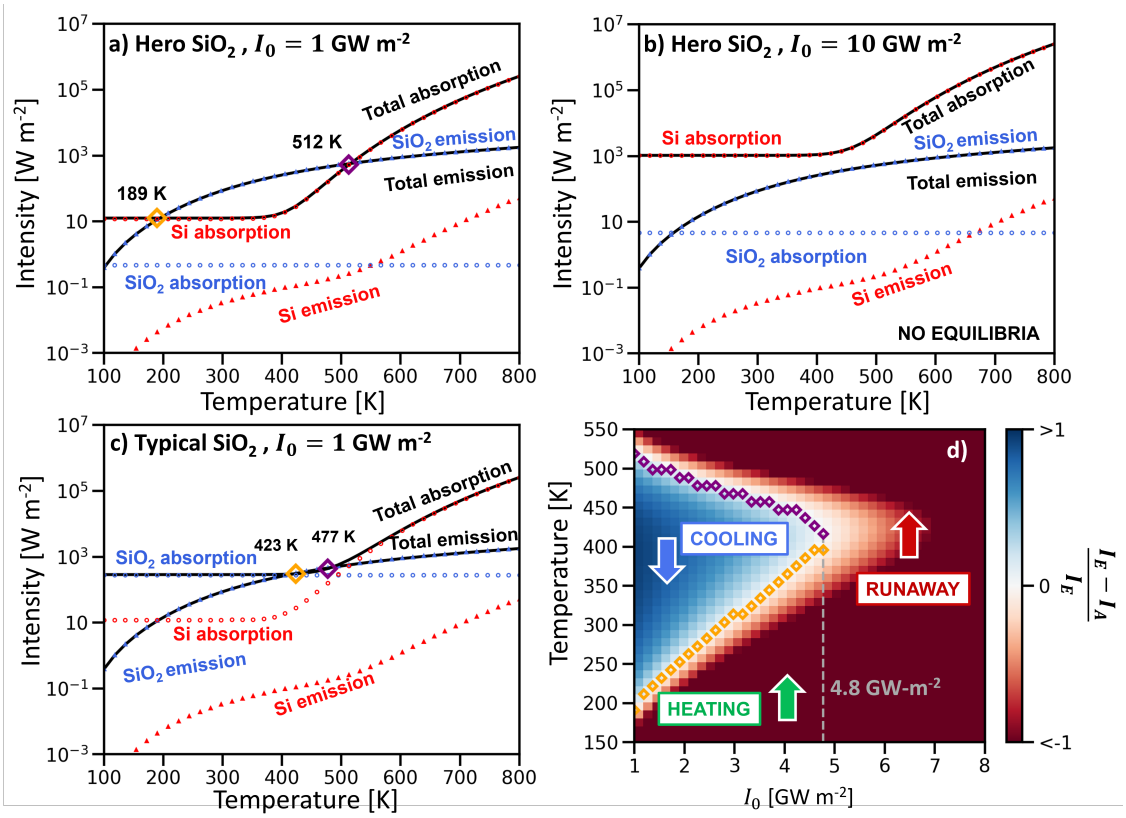

Figure 2.3: (a-c) Absorbed and thermally emitted intensities versus temperature for the Si/SiO_2 metasurface depicted in Figure 2.1 made from either Hero or Typical SiO_2 and illuminated with an incident laser intensity I_0. Stable (orange) and unstable (purple) equilibrium temperatures are labeled as diamonds. Note, there is no equilibrium temperature for Hero SiO_2 at $I_0 = 10\,\mathrm{GW\,m^{-2}}$. Absorbed and emitted intensities for the complete laser sail are shown in black while the contribution of the Si and SiO_2 layers are shown in red and blue, respectively. Dotted lines are used to indicate the Si absorption and SiO_2 emission because they overlap with the total absorption and emission. (d) Normalized difference in emissive intensity and absorptive intensity as a function of temperature T and incident intensity I_0 for a sail made with Hero SiO_2. Stable and unstable equilibrium temperatures are indicated as orange and purple diamonds, respectively. The blue and green arrows indicate the zones where the sail will either cool or heat to a stable equilibrium temperature below $I_0 \approx 4.8\,\mathrm{GW\,m^{-2}}$. Otherwise, thermal runaway occurs.

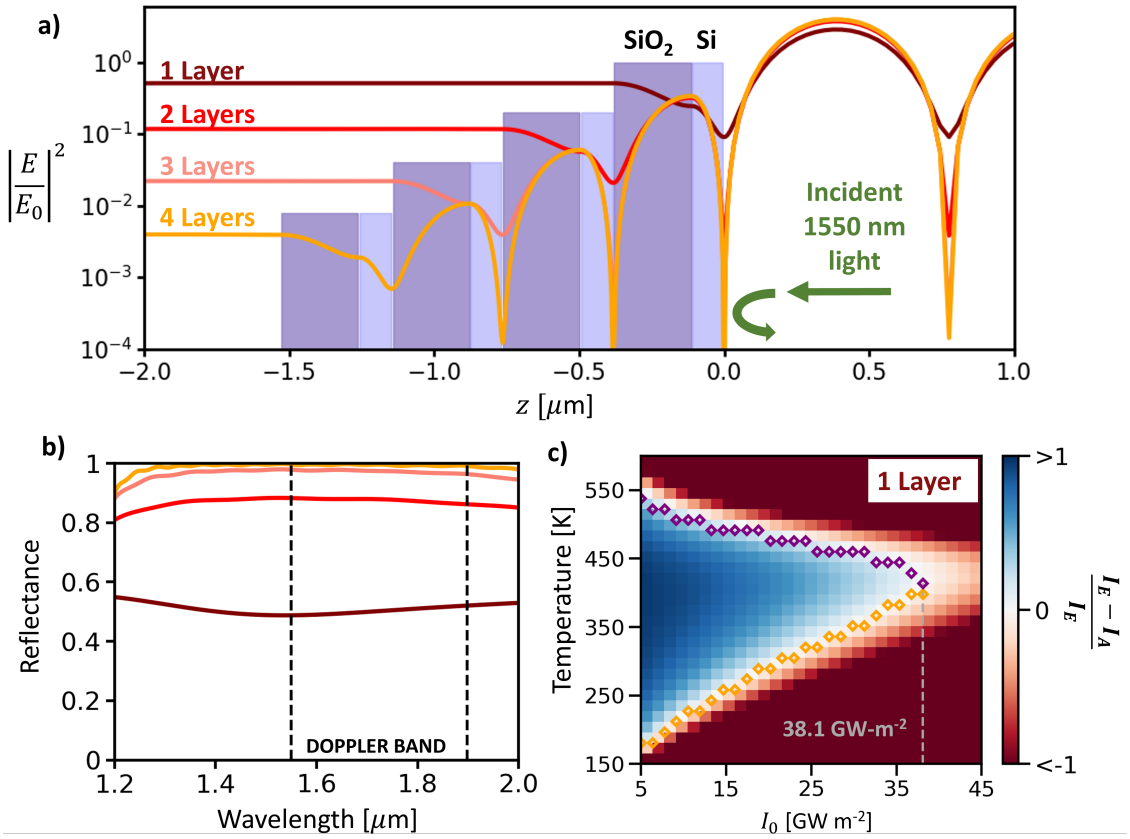

Figure 2.4: a) Side view of Bragg reflector showing electric field magnitude normalized to incident field $|E/E_0|^2$ as a function of distance above surface of Bragg reflector for various numbers of layers. Silicon and silicon dioxide are 113.3 nm and 269.1 nm thick respectively. b) Reflection spectra of Bragg stacks for various numbers of layers. Red corresponds to the Doppler band. c) Normalized difference in emissive intensity and absorptive intensity as a function of temperature T and incident intensity I_0 for single layer Bragg reflector made with Hero SiO_2.

Chapter 3

Supporting Information

3.1 Modeling of the Si absorption coefficient

The composite absorption model for Si presented in Fig. 2 of the main text includes two different models of the free carrier absorption coefficient, α_{FC}. The model from Ref. [23]] is used for wavelengths of 1.45-4 μm, the model from Ref. [[28]] is used from 5–100 μm. Because both models appear to be equally good and we expect the wavelength dependence of the free-carrier absorption to be a smooth function, we perform a linear interpolation between the two models from 4–5 μm in order to avoid an unphysical discontinuity. These models are shown in Fig. S3.1 without the interpolation as dashed black lines. The thin solid black line denotes the absorption below 1.45 μm from Ref. [[27]] and the thick black line is the multi-phonon absorption data from Ref. [[29, 30]]. To our knowledge, the lowest demonstrated absorption of Si at 1.55μm is $4.28\times10^{-6}\,\mathrm{cm}^{-1}$ and is denoted in Fig. S3.1 as a solid black circle and labeled as 'Hero Si'.[24] The absorption of Si from 7–100 μm, which at room temperature is dominated by multi-phonon absorption, has been measured; however, the tail from these absorption bands at wavelengths shorter than 7 μm has not.[29, 30]

We fit the multiphonon absorption peaks with Lorentzian lineshapes in order to extrapolate between the short-wavelength edge of the multiphonon data at 7μm and the measured absorption at 1.55 μm. First, the absorption contribution from free carriers is subtracted from multiphonon resonances. A least-squares fit is performed using Lorentzians centered at each of the allowed two- and three-phonon absorption peaks, and the carbon impurity

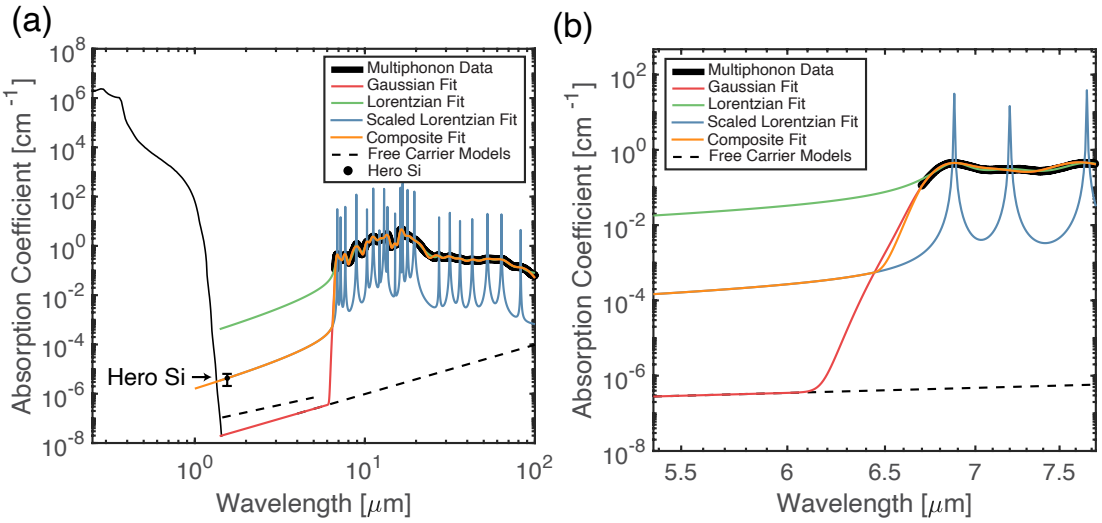

Figure S3.1: (a) The absorption of Si as a function of wavelength. Literature data and models of the absorption are shown as black lines and circles.[23, 24, 27–30]. Fits to the multi-phonon data assuming either Lorentzian or Gaussian peaks are shown in green and red, respectively. Note, the orange, green and red curves overlap at wavelengths >7 μm. Scaling the Lorentzian fit peak widths such that the tail passes through the Hero Si data point at 1.55 μm produces the blue curve. The composite model used in the calculations in the main text consists of the scaled Lorentzian fit at short wavelengths and the Guassian fit at long wavelengths and is shown in orange. The orange and blue curves overlap below 6.43 μm. (b) The absorption data and fits pictured in (a) over a narrower wavelength range. The composite fit (orange) linearly interpolates between the scaled Lorentzian fit (blue) and Gaussian fit (red) from 6.43–6.70 μm.

peak.[30, 49] Additional absorption peaks at 20, 27, 32, 36, 43, 53, 64, and 82 μm were included in the fit to better match the absorption features seen in the data at long wavelengths. We note that these energies are too small to arise from multi-phonon absorption processes and that the multi-phonon and carbon impurity peaks are the dominant contributors to the absorption tail at 1.55 μm. The tail of the best fit Lorentzian model (green curve in Fig. S3.1) predicts absorption several orders of magnitude above the measured Hero Si absorption. This indicates that the width of the peaks in the multiphonon data is the result of inhomogeneous broadening. The broadened Lorentzian peaks will appear Guassian near the center of each peak. A fit using Gaussian lineshapes instead of Lorentzians (red curve) matches the data well near the peaks but decays too rapidly at short wavelengths to capture the expected long tail behavior of Lorentzians. We therefore scale the widths of the peaks in

the best fit Lorentzian model until the tail passes through the Hero Si absorption data point at 1.55 μm (blue curve). The model for the multi-phonon absorption coefficient, $\alpha_L(\lambda)$, as a function of wavelength, λ, used in the main text consists of the scaled Lorentzian fit for λ <6.43 μm, the best fit Gaussian model for λ >6.70 μm, and then a linear interpolation between the two fits from 6.43–6.70 μm. This composite fit is shown in orange in Fig. S3.1.

3.2 Comparison of the emission and absorption of the metasurface to a continuous slab

In the main text, we showed that a particular highly reflective metasurface will experience thermal runaway at all incident intensities $I_0 > 5.4\,\mathrm{GW{\cdot}m^{-2}}$. In this section, we perform the same analysis on a heterostructure of 450 nm of Si on 200 nm of SiO2. The layer thicknesses of this heterostructure are identical to those of the the metasurface we analyzed in the main text; however, the Si layer in the heterostructure is a continuous slab instead of individual blocks. We find that the heterostructure geometry also exhibits the thermal runaway behavior of the metasurface, and has an even lower maximum I_0, above which no equilibrium temperature exists.

The emission intensity I_E is calculated in the same way as described in the main text while absorption I_A is now calculated analytically, since the surface is translationally invariant. We plot the results in Fig. S3.2. We see that for the high-quality Hero SiO_2 and $I_0 = 1\,\mathrm{GW{\cdot}m^{-2}}$, the stable temperature has risen to 203 K from the 177 K of the metasurface, while the unstable temperature has lowered to 495 K from 516 K. In Fig. S3.2d, we see this also has the effect of lowering the incident intensity limit to $I_0 = 4.1\,\mathrm{GW{\cdot}m^{-2}}$. The heterostructure is less thermally robust than the metasurface because the total absorption in the Si has risen slightly from the increased surface coverage.

The AD of the heterostructure sail design suffers for two reasons. First, as seen in Fig. S3.2d, the maximum I_0 the heterostructure can withstand is lower than that of the metasurface in the main text. Second, it is far from being highly reflective across the Doppler band of interest. Using the reflectivity spectrum and $I_0 = 4.1\,\mathrm{GW{\cdot}m^{-2}}$, we calculate the AD

to be D =532 Gm. This is more than 4 times larger than the 120 Gm AD of the metasurface in the main text.

3.3 Effective Medium Approximation in Mid-Infrared and beyond

The calculation of $I_E(T) = I_E^s(T) + I_E^i(T)$, requires performing an integration over all wavelengths, angles, and polarizations of interest using the formula

$$I_E^i(T) = \int_{\lambda_1}^{\lambda_2} d\lambda \int_0^{2\pi} d\phi \int_0^{\pi} d\theta \quad \epsilon_i(\lambda, \phi, \theta, T) \frac{hc^2}{\lambda^5} \frac{1}{\exp(hc/\lambda k_B T) - 1} \cos\theta \sin\theta, \quad (i = s, p). \tag{3.1}$$

The emissivity $\epsilon_i(\lambda, \theta, \phi)$ $(i = s, p)$ varies as a function of λ, θ, ϕ, and i. To perform this calculation by sweeping the parameters in COMSOL would be extremely computationally intensive.

To simplify this calculation, we approximate the emissivity by replacing the blocks of Si with a slab of equal thickness 450 nm and refractive index $n_{eff} = n_S i \times FF$ where $FF = (430^2)/(670^2)$ is the filling factor. The geometry in this approximation is then a stack of two unpatterned slabs which has an analytical solution for the absorptivity $\alpha_i(\lambda, \phi, \theta, T)$ using transfer matrices. Using Kirchoff's law of thermal radiation, we obtain $\epsilon_i(\lambda, \phi, \theta, T) = \alpha_i(\lambda, \phi, \theta, T)$ analytically.

At mid-infrared to long-wave infrared wavelengths (2-100 μm where thermal emission occurs), this approximation is valid. We have checked the validity of this approximation by comparing Python-based transfer matrix code with full-wave COMSOL simulations of the metasurface. We used indices $n_{Si} = 11.7 + i10^{-5}$ and $n_{SiO_2} = 2.1 + i10^{-5}$ for Si and SiO_2, respectively. Simulations were performed at incident angles $\theta = 0°$ and 60°, polarizations s and p, and from $\lambda = 1$ to 50 μm. The reflection, transmission, and absorption were recorded as shown in Fig. S3.3. It is clear that the approximation aligns closely with the simulated result. Some deviation occurs below 2 μm in wavelength, but this does not significantly affect the calculation of $I_E(T)$ because the blackbody spectrum is quite weak at those wavelengths.

3.4 Trade off in scaling of structure

As discussed in the main text, an important figure of merit for a light sail is its acceleration distance (AD).[22] This number is influenced not only by the maximum intensity the sail can survive, but also by the mass of the sail and the reflection spectrum over the Doppler band (1550 nm to 1900 nm). Prior to our analysis demonstrating the existence of a maximum survivable intensity, the metasurface geometry presented in the main text was chosen to maximize its reflectivity at 1550 nm. Here we optimize for the shortest possible acceleration distance by scaling the original structure and calculating how the reflectivity, mass, and maximum survivable intensity vary with structure geometry.

The scaling is shown in Figure S4a. All dimensions of interest are scaled by a factor x where $x = 1$ is the original structure shown in the main text. The electric field changes with the structure as seen in Figure 4b. At $x = 1.05$ ($x = 0.95$) the magnitude of the field increases (decreases). In Figure S4c, we can see that this is caused by a shift in the spectral position of the resonance near 1300 nm. Scaling up shifts the resonance toward the driving laser wavelength of 1550 nm increasing the absorption. Simultaneously, the reflection plateau shifts into the Doppler band providing higher reflection. While the increased reflection ought to decrease the AD, the increased absorption will decrease the maximum intensity raising the AD. At some value of x is a minimum AD.

In Figure S4d, we show the impact of scaling the structure on both I_{Max} and the AD. As expected, I_{Max} decreases due to the increased absorption. Changes in the mass due to scaling are also accounted for, but not plotted here. The AD exhibits a minimum at $x = 1.05$, showing that the structure presented in the main text was close to optimal. The AD reduces from 148.9 Gm to 126.5 Gm when scaling the structure to be 5% larger, corresponding to a period of 703.5 nm, Si block height and width of 472.5 nm and 451.5 nm, and SiO_2 thickness of 210 nm. This demonstrates that the structure shown in the paper can not be improved much without performing an optimization in a much larger parameter space. Such work, however, is beyond the scope of this paper.

3.5 Perfect Blackbody Emission

Thermal runaway will still occur, even in the ideal case where the sail is able to thermally radiate as a perfect blackbody. While SiO_2 exhibits strong emission in the mid-infrared, the thickness of the SiO_2 layer in the geometry we consider in the main text is too thin to provide perfect blackbody emission. Layer thicknesses on the order of the wavelength of emission ($\sim$10 μm) would be needed to achieve anything close to perfect blackbody emission. As an example, if we assume a 10 μm thick film with an absorption coefficient of 10^3 cm^{-1}, this yields a total emission of I_{BB}/e where I_{BB} is the blackbody emission. This is about 50 times thicker (and therefore 50 times heavier) than the SiO_2 in the design reported in the main text.

Figure S3.5 shows the thermal stability analysis assuming the SiO_2 in the metasurface emits as a perfect blackbody (grey line). Performance does improve; the stable equilibrium temperature lowers to about 100 K and the unstable equilibrium temperature rises to 650 K. Furthermore, Figure S3.5b shows that the maximum survivable intensity I_{Max} rises to 18.8 GW m^{-2}. These gains in thermal stability and maximum survivable incident intensity would be offset by the significant increase in sail mass need to achieve such a large emissivity.

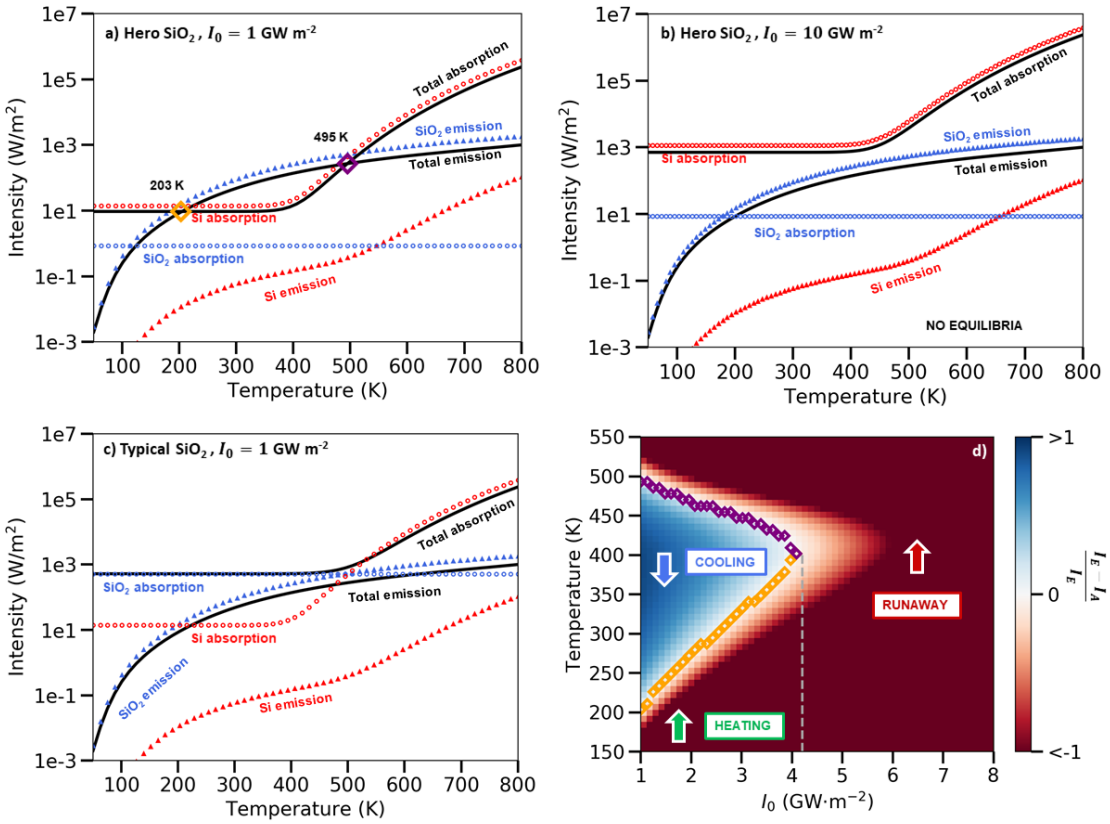

Figure S3.2: Replication of Fig. 3 in the main text, but for a Si/SiO_2 heterostructure with a solid layer of 450 nm Si on 200 nm SiO_2. (a-c) Absorbed and thermally emitted intensities versus temperature for the Si/SiO_2 heterostructure made from either Hero or Typical SiO_2 and illuminated with an incident laser intensity I_0. Stable (orange) and unstable (purple) equilibrium temperatures are labeled as diamonds. Note, there is no equilibrium temperature for Typical SiO_2 at $I_0 = 1\,GW{\cdot}m^{-2}$ or Hero SiO_2 at $I_0 = 10\,GW{\cdot}m^{-2}$. Absorbed and emitted intensities for the complete laser sail are shown in black while the contribution of the Si and SiO_2 layers are shown in red and blue, respectively. Dotted lines are used to indicate the Si absorption and SiO_2 emission because they overlap with the total absorption and emission. (d) Normalized difference in emissive intensity and absorptive intensity as a function of temperature T and incident intensity I_0 for a sail made with Hero SiO_2. Stable and unstable equilibrium temperatures are indicated as orange and purple diamonds, respectively. The blue and green arrows indicate the zones where the sail will either cool or heat to a stable equilibrium temperature below $I_0 \approx 4.1\,GW{\cdot}m^{-2}$. Otherwise, thermal runaway occurs.

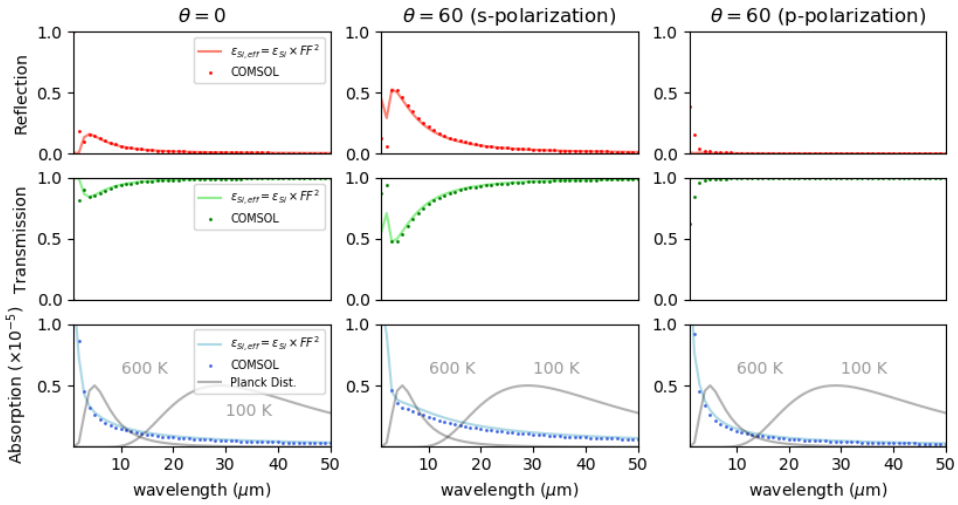

Figure S3.3: Comparison of the reflection, transmission, and absorption spectra of the metasurface using the analytic approximation (i.e. assuming Si to be a solid slab with an effective index) and full-wave simulations in COMSOL. For wavelengths longer than 2 μm, the agreement is very good, implying that this approximation is valid for calculations of the metasurface's emissivity.

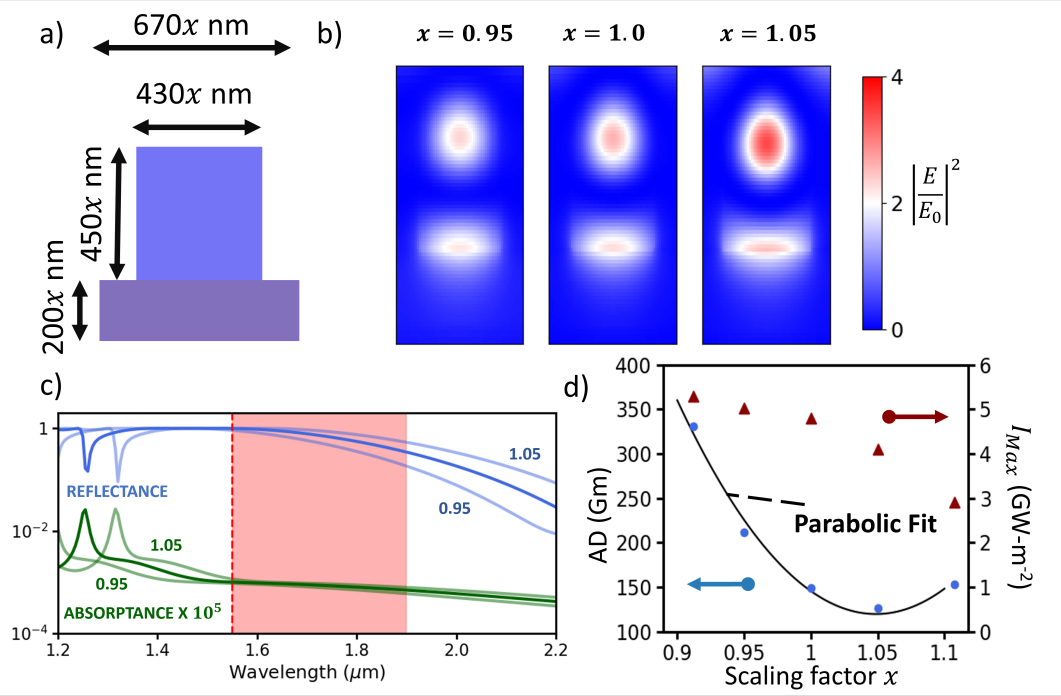

Figure S3.4: a) Schematic of the scaling of our metasurface. The scale factor x applies to all dimensions, including the out-of-plane width of the Si block ($430x$) and period ($670x$). b) Squared electric field magnitude at 1550 nm of the metasurface at different scaling factors. Field magnitude increases at higher scaling factors. c) Reflection and absorption spectra of the metasurface at different scaling factors. Absorption coefficient of silicon is chosen to correspond to $I_0 = 1$ GW·m^{-2} and $T = 300$ K. Scaling the structure simply shifts the spectrum. d) AD versus scaling of the metasurface in the main text of the paper. Scaling the surface to by 5% larger results in an optimal AD of 126.5 Gm.

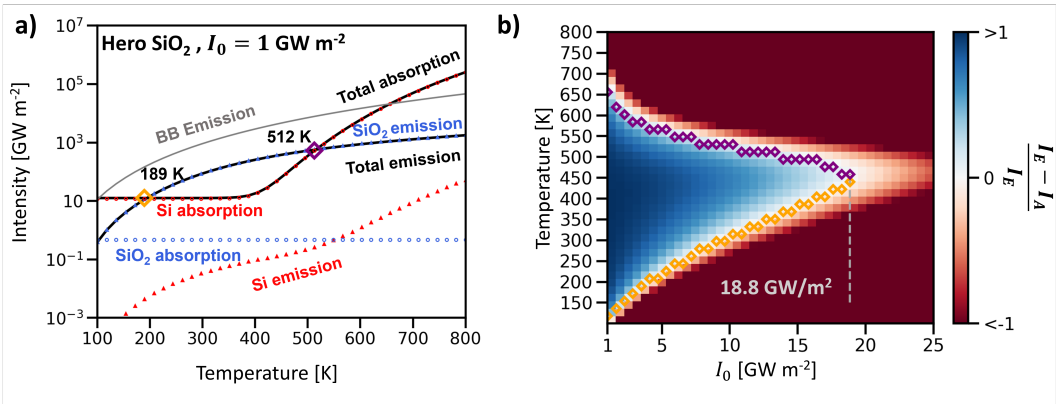

Figure S3.5: Thermal stability analysis for theoretical metasurface using Hero SiO2 for absorption, but assuming perfect blackbody emission for radiative cooling. (a) calculation of the thermal runaway temperature (650 K) and equilibrium temperature (100 K) for a perfect blackbody emitter. (b) Calculated regions of thermal runaway heating (red) and equilibrium cooling (blue) for the metasurface, indicating a maximum laser intensity of 18.8 GW m^{-2}. Purple and orange dots represent thermal runaway and equilibrium temperatures, respectively.

Part II

Tunable Narrowband Mid-Infrared Thermal Emission

Chapter 4

Introduction

4.1 Mid-Infrared Optical Systems

The mid-infrared (MIR) region of the electromagnetic spectrum spans roughly from 2 μm to 25 μm in wavelength. Physical investigation of this region requires a full optical system: sources, detectors, and filters among other components. Historically, optical systems operating in the MIR have been underdeveloped compared to the visible, ultraviolet, near-infrared, and radio frequencies.[50] This latency is particularly evident for a class of components known as tunable narrowband MIR sources. As it stands, such components are either too expensive or too bulky to be practical for many applications. Applications that are commonplace outside in the visible to NIR consequently are not as common in the MIR. Yet there are many reasons to put effort toward developing these special emission sources.

To understand tunable narrowband sources, it is helpful to picture a laser with a modifiable output wavelength. This optical component has an emission frequency ω_0 (wavelength $\lambda_0 = 2\pi c/\omega_0$) with a narrow linewidth $\delta\omega_0 \ll \omega_0$ ($\delta\lambda_0 \ll \lambda_0$), as shown in Figure 4.1a. Unlike conventional lasers, this frequency can be altered even after the laser has been built. In the visible and NIR, this technology is readily available in many forms, mostly notably as tunable diode lasers.[51, 52] External cavity III-V diodes lasers (ECDLs), for example, are available below 2 μm in low-SWaP packaging and operate at room temperature.[52] Such lasers have extremely narrow emission spectra (linewidths on the order of 10^{-4}cm^{-1}) and can be tuned at a rate $\sim 1\ \text{cm}^{-1}\text{K}^{-1}$ by changing the temperature. For faster tuning, current

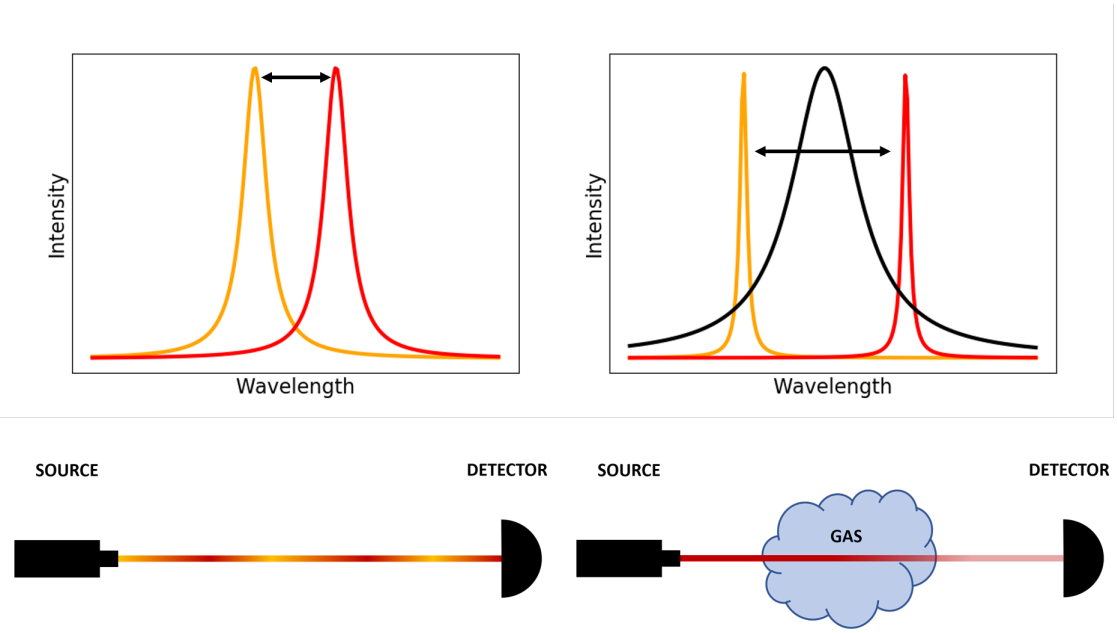

Figure 4.1: Applications of frequency-tunable MIR sources a) FSOC application. Center wavelength is tuned to encode information. Since the tuning is larger than the FWHM, the detector is able to distinguish the two center frequencies. b) Optical gas-sensing application. Narrowband emission passes through a gas with a particular absorption line. The center wavelength is scanned over the peak. A narrower emission linewidth better resolves the peak.

modulation is used at 5×10^{-3} mA^{-1} at a rate of about 10 kHz.[51] There are tunable MIR sources available, and while they may match or exceed the performance of many visible and NIR sources, they tend to be much more expensive and bulky limiting their applicabilty.

Tunable MIR sources include CO_2 lasers, quantum cascade lasers (QCLs), interband cascade lasers (ICLs), IV-VI lead-salt diode lasers, and many others.[52] Each technology has some combination of issues that limits its applicability: cryogenic operation, poor tunability, low power at frequencies of interest, being restricted to pulsed operation, or tuning via temperature changes which couples frequency and output power.[52] For example, lead-salt diode lasers must operate below 120 K which limits applicability.[51] While many applications of tunable MIR sources can often find a solution, the perfect tunable MIR source does not exist today.[52]

Today, QCLs and ICLs are the most widely applicable tunable MIR sources. Development began in 1987, when band-gap engineering was developed.[53] This subsequently led to the

demonstration of the quantum cascade laser (QCL) in pulsed operation in 1994.[54] By 2002 the technology reached a maturity that allowed continuous wave (CW) operation at room temperature.[55] Now QCLs operate at wavelengths between 3-25 μm with linewidths as low as 200 Hz at room-temperature and exhibit large tunability.[50] They are a mature technology being manufactured by many companies. However, they remain expensive due to the many-layer semiconductor layers required. This cost keeps MIR laser light from being practical for certain uses.

Many molecules of interest have their fundamental absorption lines in the MIR. These include CO, CO_2,NO, N_2O, NO_2, NH_3, C_2H_4.[56] Absorption spectroscopy measures the concentration of these gasses by passing light through a sample. By modulating the output frequency, higher sensitivities can be reached.[57] A schematic is shown in Figure 4.1b. Tunable lasers are used for this purpose with techniques known as wavelength modulation spectroscopy (WMS) and frequency modulation spectroscopy (FMS).[57, 58] With WMS/FMS, rather than measuring the absorption at a single wavelength, the emission wavelength is rastered across an absorption line to detect the amount of gas in a sample. In the visible and NIR, WMS and FMS are capable of detecting gasses to part-per-million levels. The absorption lines detected by these setups are actually overtones of fundamental resonances in the MIR. All else equal, this make MIR spectroscopy quite a bit more sensitive. MIR WMS regularly reaches ppb detection.[52] However, despite this utility it is still impractical for many applications due to the cost of QCLs.

The first room-temperature gas spectroscopy with a QCL was performed in 1998.[59] Since then, QCLs have been shown to detect CO,[60], NO[61], and NH_3[62] to part-per-billion levels. These experiments were performed in laboratory settings. For use in a field environment, an open-path detector is needed. However, such systems are bulky with one example weighing 15 kg.[63] The goal of this thesis is to create a source that is many times lighter and cheaper than a QCL.

Free-space optical communication (FSOC) is another application where narrowband frequency-tunable MIR sources could be of use. Encoding information in light requires that the source

have two states. These states can either be on-off like AM radio, or the source may switch between two frequencies like FM radio. This communication scheme is known as *keying*. When sending light through the atmosphere, it is necessary to avoid absorption lines. The atmosphere has transmission windows in the mid-IR at 3-5 μm and 8-14 μm [64]. Being higher in frequency, and therefore having a larger bandwidth, MIR sources have an advantage over much of the RF spectrum. MIR sources have already been shown to transmit Gbps data rates in labratory settings.[65, 66] Furthermore, MIR light carries an advantage over optical because it is less prone to Rayleigh scattering [65, 67] Much stands to be gained by opening this region of the electromagnetic spectrum to FSOC.

With all of these engineering challenges surrounding MIR laser sources, it is ironic that MIR light is plentiful in the form of thermal radiation. It is clear that the idea of pumping on a gain medium to generate narrowband emission is unlikely to yield the technology we are after, i.e. emission that is simultaneously narrowband and frequency-tunable in a package that is compact and cheap. The goal of this thesis is to develop a technology to fill this space using thermal radiation. Despite the broadband nature of thermal radiation, subwavelength patterned structures can reduce the bandwidth to extremely narrow values. This mimics the emission seen from a laser. In order to endow such a device with frequency tunability, one can incorporate optically tunable materials. The next sections describe the effort that has gone into developing such a device thus far.

4.2 Efforts to Create a Tunable Narrowband MIR Thermal Emitter

In order to address the need for MIR frequency-tunable light sources, plasmonic metasurfaces with optically tunable materials were first investigated. The ability of noble metals to confine light on small scales in local surface plasmons (LSPs) made them attractive materials for altering thermal emission spectra. Optically tunable materials investigated for this purpose include phase-changing materials,[68] ITO,[10–12] multiple quantum wells,[9] and microelectromechanical systems.[69] Many of these materials have issues that make them

impractical for this application. In this thesis, we cover the use of graphene.

It was Liu et al. that first introduced the idea of using plasmonic metasurfaces to alter thermal emission spectra.[70] They demonstrated that placing an array of cross-shaped gold resonators on a surface could create narrow resonance that could easily shift in frequency by scaling the size of the crosses. They also demonstrated that Kirchoff's Law of Radiation was obeyed. Though an important demonstration that thermal emission spectra are controllable, the spectrum could not be altered once the device was fabricated. For the purposes of a tunable mid-infrared source, optically tunable materials are required.

Graphene is one of the most promising optical materials for tuning resonances. After the demonstration by Liu et al., work showed that the presence or absence of graphene altered the optical properties of a similar plasmonic device.[71] No effort was made in this paper to electrically tune the device after fabrication, however. Not long after in 2011, Ju et al. utilized an ionic gel to demonstrate that graphene's optical properties could be dynamically tuned by an applied voltage. [72] This opened the door to altering the thermal emission spectra of plasmonic metamaterials even after fabrication. Li and Yu suggested using graphene to tune gold nanoresonators on a surface.[73] Later Yao et al. demonstrated the electrical tunability of gold nanoresonators. This resonance tuned 0.8 times the full-width half maximum.[13] They later demonstrated a new design that achieved larger absolute tuning at the expense of full-width half maximum [14]. This design was also used to theorize modulation rates of up to 20 GHz. [74]

While large absolute tuning was demonstrated with plasmonic materials acting as the antennae, the resonance in these works were simply too broad. In all instances, the resonance was unable to tune more than a full-width half maximum. This is in large part due to their large absorptive losses at mid-infrared frequencies. It was clear that plasmonic materials would be unable to provide the narrow linewidths needed to achieve high tunability. In order to achieve narrow resonances and enhanced tunability, different materials altogether must be used. It has become clear that high-index dielectric materials such as Si and Ge can be patterned to produce modes with the same field enhancements as plasmonic materials,

but with much lower absorptive loss.[75] The first electrical control of graphene on a Si photonic crystal was demonstrated in 2013.[76] This work demosntrated that the reflective magnitude of a resonance could be electrically tuned. Another work demonstrated a similar device.[77] However, these devices used ionic gels for tuning the graphene and, furhtermore, operated at telecom wavelengths ($\lambda \sim 1500$nm). A device using hot electrons in graphene on a Si photonic crystal has been reported operating in the mid-infrared. [78] However, the frequency tuning is related to temperature, and therefore the power, so it is not an ideal device. Graphene tuning of a Si photonic crystal cavity operating near 4.5 μm was demonstrated but only with a tunability of about 0.82.[79] The emission was also quite weak limiting applicability. The reason for the weak emission was the lack of a backreflector. One issue with these devices was the inability to control the radiative coupling. In this thesis, we build on these devices by incorporating graphene into a device that has easily controlled radiative coupling and a backreflector for enhanced emisison.

Chapter 5

Background

In this section, we cover the background material required to understand tunable metasurfaces in general.

5.1 Thermal Emission

Any object at nonzero temperature T exhibits thermal emission: electromagnetic radiation originating from the random motion of the molecules and atoms comprising the object. The maximum possible intensity of emission per unit wavelength λ per steradian Ω is described by Planck's Law[6]

$$I_{BB}(\lambda, T)d\lambda\, d\Omega = cu(\lambda, T)d\lambda\, d\Omega = \frac{8\hbar\pi c^2}{\lambda^5}\frac{1}{e^{hc/\lambda kT} - 1}d\lambda\, d\Omega \tag{5.1}$$

where $u(\lambda, T)$ is the energy density in the object. The theoretical object that matches this intensity is known as a blackbody. Wien's law provides the wavelength of peak emission $\lambda_W \approx \frac{1}{T}(2898\mu\text{m-K})$, of this spectrum. At room temperature (T =300 K), the intensity of this radiation peaks at $\lambda_W = 9.66\mu$m. This places the emission squarely in the MIR, which is perfect for our thermal emission device. Via Wien's law, it would seem that temperature T is the only method of choosing the wavelength of peak thermal emission. However, Eqn. 5.1 describes a perfect blackbody, which does not exist. In reality, at every wavelength a structure will emit slightly less intense radiation than stated by Planck's Law. We introduce the emissivity[6]

$$E_i(\lambda, \theta, \phi, T; \beta) = \frac{I_i(\lambda, \theta, \phi, T; \beta)}{I_{BB}(\lambda, T)} \leq 1, \tag{5.2}$$

where I is the true intensity of radiation. The quantity I is dependent polarization ($i = s$ or p), polar angle θ and azimuthal angle ϕ. We also include dependence on other parameters in β. As we will see, this will allow us to tune the emissivity and therefore tune the thermal emission.

Given a metasurface, direct calculation of E can be quite difficult. Methods such as the Thermal Discrete Dipole Approximation are based on the fluctuation-dissipation theorem and require simulating large numbers of dipole sources at various positions in a structur.[80] Such methods can be extremely computationally intensive and are more appropriate for near-field thermal radiative transfer. In the far field, however, Kirchoff's law of thermal radiation provides a solution. The theorem states that under certain easily satisfied conditions, it is equivalent to calculate the absorptivity of the structure.[81] More specifically,

$$E_i(\lambda, \theta, \phi, T; \beta) = A_i(\lambda, \theta, \phi, T; \beta). \tag{5.3}$$

Algorithms such as Finite-difference time domain (FDTD) and Finite Element Method (FEM) can easily calculate A by simulating the injection of a plane wave and recording the reflectivity R and transmissivity T. The remainder $A = 1 - R - T$ is the absorptivity. Additionally, one may run the simulation recording the electric field and perform a volumetric integral to obtain the absorption.[82] This opens the possibility of using certain commercially available softwares such as Lumerical (FDTD) or COMSOL (FEM) with which we will simulate the injection of a plane wave and subsequent absorption by the structure.

There is a long history of research efforts to engineer E in the MIR. In 1988, Hesketh et al. fabricated grooves in a doped Si membrane [83]. Greffet et al. fabricated grooves in a SiC membrane to create highly directional emissivity.[7] However, this design was based on a photonic crystal which limited the sharpness of the resonance. The first demonstration of a metamaterial engineered to have an emission spectrum narrower than a blackbody came

in 2011 from Liu et al. [70]. They found experimental agreement with Kirchoff's law thus beginning the engineering of metamaterial thermal emitters.

5.2 Optically Tunable Materials

As implied by Eqn. 5.1, all materials exhibit tunable thermal emission by modification of their temperature T. However, this method is slow being limited by thermal conductivity to about 100 Hz.[84] The goal of this thesis is to develop a device with tuning rate on the order of 10-100 MHz. For this reason, we restrict our attention to materials that can tune the emissivity E.

Some emissivities are tunable by changes in phase induced by changes in temperature T. These changes can be much faster than the time scales set by thermal conductivity making phase changing materials a strong candidate for this type of emissivity modulation. Materials include germanium-antimony-tellurium[85] and vanadium dioxide.[8] However, none of these are not quite appropriate for frequency tuning as the change in temperature couples the emitted power to the frequency. Our ideal tunable thermal emitter would have consistent power at all frequencies.

Other materials have issues as well. Inoue et al. used GaAs/GaAlAs multiple quantum wells in conjunction with a photonic crystal in order to tune emissivity.[9] Indium tin oxide (ITO) is a plasmonic material that has been used to tune plasmonic antennas[10, 11] as well as dielectric resonators. [12] [more info on why these aren't good?]

Finally, graphene is a strong candidate for the optically tunable materials of the device and the subject of this thesis. It is an atomically thin layer of carbon atoms arranged in a Bravais lattice with two atoms per unit cell (Figure 5.1a). This crystalline structure leads to a linear bandstructure with slope $E = \hbar v_F$ as seen in Figure 5.1b.[86] The quantity $v_F = 10^6$ m/s is known at the *Fermi velocity* and it is the "speed" of the carriers in the graphene. The carrier concentration is highly tunable which in turn alters the optical properties, particularly strongly in the mid-infrared. In addition, being an allotrope of carbon, graphene is a highly durable material capable of withstanding temperatures as high as 2000° C in inert

atmosphere. The electrical and optical properties of graphene are reviewed in Appendix A.

The properties of graphene most significantly influencing its permittivity are the mobility μ and the Fermi level E_F. The mobility μ, not to be confused with the permittivity μ, can be thought of as the quality of the graphene and has units cm^2/V-s. A high mobility ($\sim 10,000$ cm^2/V-s) is desirable as this corresponds to a low density of defects.[86] There are methods for achieving high mobility graphene, but in general it is difficult to control this value. In this thesis, mobility is assumed to be about 650 cm^2/V-s. Tuning of E_F is much simpler. The quantity is the energy of the highest energy electron (Figure 5.1b). Tuning this value is equivalent to injecting charge carriers and is the most important way to change the permittivity of graphene. Units of E_F are typically given in eV. Conversely to μ, there are many methods for tuning E_F, although they carry trade-offs in their speed, reliability, structural requirements, and the range of E_F achievable.

First, chemical doping is a useful method for creating a large Fermi level. After transferring to a substrate, graphene is placed in a furnace along with a boat of Iron (III) Chloride ($FeCl_3$).[87] The ions donate carriers to the graphene raising its carrier concentration as high as $n = 10^{14}$ cm^{-2}, equivalent to $E_F = \hbar v_F \sqrt{\pi n} = 1.17$ eV. While the range of Fermi level tuning is great, the method creates a static Fermi level and is therefore not useful for dynamically tunable light sources.

A more dynamic method for tuning E_F is ionic gels. These are liquid gels with suspended ions which donate or accept electrons. This was the method first used to demonstrate dynamic tuning of graphene's optical properties.[72] With this method, E_F may reach >1 eV. However, the presence of a liquid makes it impractical to package.

Finally, there is electrostatic tuning. A sheet of graphene is capacitively coupled to a conductor and a voltage bias V is applied. Graphene may be electrostatically tuned in this parallel plate capacitor geometry (Figure 5.1c). A spacer layer of dielectric separates a backgate from graphene. The spacer is typically silicon dioxide (SiO_2) but silicon nitride (Si_3N_4), hafnia (HfO_2) and other dielectric compounds are often used. This geometry is our choice because it is dynamic, practical to analyze, can be engineered for fast switching, and

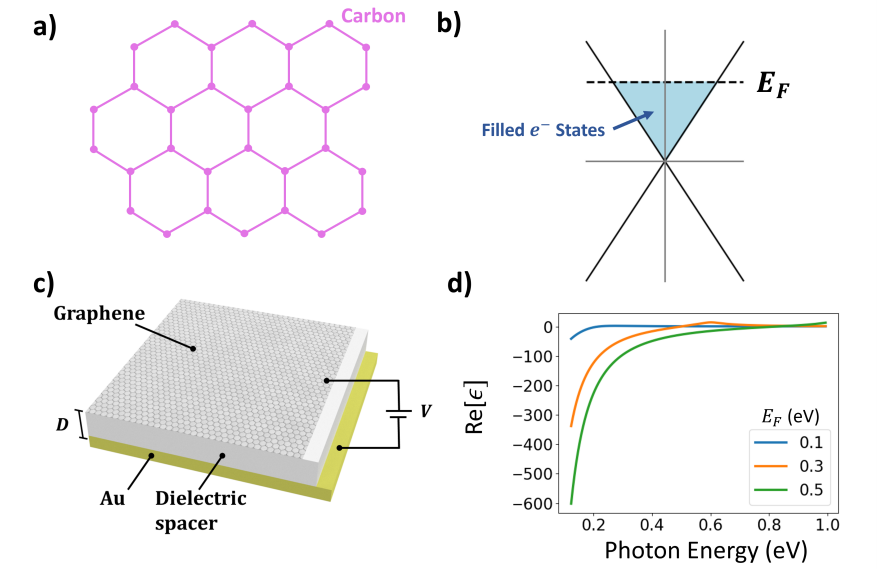

Figure 5.1: a) Crystalline structure of graphene, a Bravais lattice of carbon atoms. b) Bandstructure of graphene. The lines have a slope $\pm\hbar v_F$ and the energy of the highest filled state if denoted by E_F. c) Parallel plate capacitor geometry used to tune E_F electrostatically. Electrical contact is made to both "plates", the graphene and Au, and a bias V is set up between them. A dielectric spacer of thickness d separates the plates. d) Changes in the real part of the permittivity ϵ of graphene.

is readily compatible with basic fabrication techniques. The real part of the permittivity for various E_F is shown in Figure 5.1d.

Recall that in a parallel-plate capacitor geometry the charge per unit area is given by

$$q = CV \tag{5.4}$$

where the capacitance per unit area is given by

$$C = \kappa\epsilon_0/D,$$

with κ being the dielectric constant of the spacer. In Appendix A, we show charge per unit area is related to the Fermi level by

$$q = \frac{eE_F^2}{\pi\hbar^2 v_F^2}. \tag{5.5}$$

Combining Eqn. 5.4 and and Eqn. 5.5 yields

$$E_F = \left(\frac{\kappa\epsilon_0\pi\hbar^2 v_F^2}{e}\frac{V}{D}\right)^{1/2} \sim \sqrt{V}. \tag{5.6}$$

This equation implies that simply by changing the voltage, one is able to modify the Fermi level of the graphene and therefore modify its optical properties.

In practice, the parallel plate geometry has some limitations. Achieving a large Fermi level can be difficult with the principal reason being dielectric breakdown. For example, SiO_2 has a dielectric constant of $\kappa = 3.6$ and experiences dielectric breakdown at a rate of roughly $V/D = 10$ MV/cm which limits the Fermi level to $E_F \approx 500$ meV. However, the rate of dielectric breakdown can vary and is larger for oxides which are thick or of higher quality. For this reason, this thesis assumes E_F can reach as high as 600 meV. In addition, note that V/D appears in Equation 5.6. This implies that a thicker oxide simply means higher voltages are required to achieve the same Fermi level, so there is not much to be gained from an electrical point of view by increasing the the thickness of the spacer layer.

We will use this geometry and put a photonic crystal on top of it. This will modify the emissive properties of the structure.

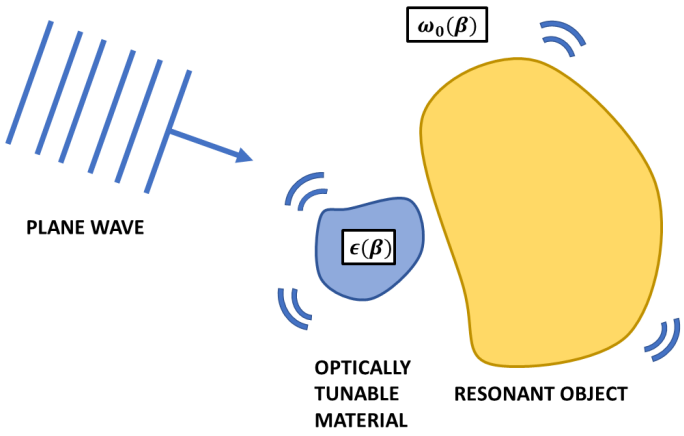

Figure 5.2: Optical system consisting of a resonant object near optically tunable material. The resonant frequency of the system ω_0 is a property of the entire system due to the electrical proximity of the two object. It is therefore dependent on the parameter β that tunes the optically tunable material.

5.3 Resonance Tuning

Once fabricated, a device may exhibit some resonance frequency ω_0 which manifests itself in the emissivity $E(\omega)$ and in turn the thermal radiation spectrum. The geometry being determined, the only means of modifying ω_0 is some active change in the optical properties of its constituent materials. The inclusion of an optically tunable material (Sec. 5.2) is therefore essential to the development of our device.

To begin, let's assume the existence of some optically tunable material with a permittivity $\epsilon(\omega;\beta)$ where β is some parameter that changes the permittivity. Placing this material in the neighborhood of a resonant object, the system has a resonant frequency ω_0 with a full-width at half-maximum γ, both of which are dependent on β such that $\omega_0 = \omega_0(\beta)$ and $\gamma = \gamma(\beta)$. The tunability we define as the absolute shift in resonant frequency normalized to its average full-width half maximum $\bar{\gamma} = (\gamma(\beta_1) + \gamma(\beta_0))/2$.

$$\frac{\Delta\omega_0}{\gamma} = \frac{\omega_0(\beta_1) - \omega_0(\beta_0)}{\bar{\gamma}} \tag{5.7}$$

To begin, the shift in resonant frequency can be expressed exactly as [88, 89]

$$\frac{\omega_0(\beta_1) - \omega_0(\beta_0)}{\omega_0} = \frac{-\iiint_V dV\ (\Delta\epsilon \cdot E) \cdot E_0^*}{\iiint_V dV (\mu H \cdot H_0^* + \epsilon E \cdot E_0^*)} \tag{5.8}$$

where $\Delta\epsilon = \epsilon(\beta_1) - \epsilon(\beta_1)$ is the difference in permittivity matrix. If $\Delta\epsilon$ is small enough, the fields will not change much either such that $E \approx E_0$ and $H \approx H_0$. This allows the denominator of this equation to be written as the sum of magnetic and electric energies in the resonance such that

$$\frac{\omega - \omega_0}{\omega_0} = -\frac{\iiint_V \Delta\epsilon_\perp |E_\perp|^2 + \Delta\epsilon_\parallel |E_\parallel|^2}{W_m + W_e} \tag{5.9}$$

where we have assumed $\Delta\epsilon$ to be diagonal and decomposed the resulting dot product into its parallel and perpendicular components. Graphene's permittivity only changes for the in-plane component and therefore $\Delta\epsilon_\perp = 0$. Recall that this shift is due to some parameters β. Expressing in terms of differentials with respect to β,

$$\frac{1}{\omega_0}\frac{\partial\omega_0}{\partial\beta} = -\frac{\iiint_V (\partial\epsilon_\parallel/\partial\beta)|E_\parallel|^2}{W_m + W_e} \tag{5.10}$$

In addition, perturbation theory provides an expression for the width of the resonance [89]

$$\gamma/\omega_0 = Q^{-1} = \frac{\iiint_V dV\epsilon"|E|^2}{W_m + W_e} \tag{5.11}$$

Let's consider the expression

$$\frac{1}{\gamma}\frac{\partial\omega_0}{\partial\beta} = \frac{1}{2(\gamma_{rad} + \gamma_{abs} + \gamma_{imp})}\frac{\partial\omega_0}{\partial\beta} \tag{5.12}$$

where γ_{rad} is the free-space coupling rate, γ_{abs} is the absorption rate, and γ_{imp} is imperfection rate due to fabrication errors. This decomposition is possible according to temporal coupled mode theory.[90] We will name this quantity the *differential tunability*. Note that we wish to minimize all components of γ in order to maximize the tunability. We wish to choose materials with low absorption such that γ_{abs} is small in a geometry such that γ_{rad} can be tuned easily. We also wish to have high-quality fabrication such that γ_{imp} is low. In section 5.5, we discuss why a geometry known as *dimerized high-contrast gratings* are ideal for this purpose.

We'll now derive a limit to the differential tunability. Equation 5.12 comes from dividing Eqn. 5.10 by Eqn. 5.11, i.e. normalizing to the width of the resonance. Limiting to the case that $\gamma_{imp}, \gamma_{rad} \ll \gamma_{abs}$, then in terms of integrals, it is expressed as

$$\frac{1}{\gamma}\frac{\partial\omega_0}{\partial\beta} = \frac{\iiint_{V_{OTM}} dV(\partial\epsilon_\parallel/\partial\beta)|E_\parallel|^2}{2\iiint_V dV\epsilon_\perp"|E_\perp|^2 + \epsilon_\parallel"|E_\parallel|^2} \tag{5.13}$$

where we've restricted the upper integral to the volume of the optically tunable material V_{OTM}, since $\partial\epsilon_\parallel/\partial\beta = 0$ elsewhere. From this expression, we can obtain a limit to the differential tunability. First of all, maximizing this value requires maximizing the in-plane field $E_\parallel$. This can be achieved by using TE-polarized light, in which the electric field is in-plane by definition. If $\epsilon_\parallel|E_\parallel|^2 \gg \epsilon_\perp|E_\perp|^2$, the perpendicular component will be negligible and we will find

$$\frac{1}{\gamma}\frac{\partial\omega_0}{\partial\beta} = \frac{\iiint_{V_{OTM}} dV(\partial\epsilon_\parallel/\partial\beta)|E_\parallel|^2}{2\iiint_{V_{OTM}} dV\epsilon_\parallel"|E_\parallel|^2 + \iiint_{V\ V_{OTM}} dV\epsilon_\parallel"|E_\parallel|^2} \tag{5.14}$$

where we've split the integration over V_{OTM} and everywhere else. The first integral is absorptive losses occuring in the OTM. The second integral is losses occuring elsewhere. Now it is clear that maximizing differential tunability means minimizing the losses in the materials which are not optically tunable. In the limit that the rest of the materials are lossless, we have

$$\frac{1}{\gamma}\frac{\partial\omega_0}{\partial\beta} \leq \frac{\iiint_{V_{OTM}} dV(\partial\epsilon_\parallel/\partial\beta)|E_\parallel|^2}{2\iiint_{V_{OTM}} dV\epsilon_\parallel"|E_\parallel|^2} = \frac{1}{2\epsilon_\parallel''}\frac{\partial\epsilon_\parallel}{\partial\beta} \tag{5.15}$$

which is valid because the permittivity is constant over the tunable material. This result is extremely useful because given the permittivity of any optically tunable material, we now have an absolute limit to the differential tunability. This limit relies on the assumption of a single isolated resonance. It can be breached by using two coupled resonances. This limit and a discussion on exceeding it appear in the following paper.[91]

5.4 Bound States in the Continuum

An optimally tunable metasurface requires a structure with particular qualities. Increased tunability can be found via high-quality fabrication or by decreasing both free-space coupling

γ_{rad} and absorption γ_{abs}. This is the result of Eqn. 5.12. Metasurfaces satisfying all of these conditions can be found in the form of *dimerized high-contrast gratings*. These are dielectric metasurfaces supporting optical states known as bound states in the continuum (BICs). As we shall see, dielectric materials such as Si and Ge are some of the best candidate materials for supporting this resonance. They are characterized by having high indices while maintaining low loss in the mid-infrared.

BICs as a concept were originally introduced in quantum mechanics by von Neumann and Wigner [92]. In this paper, the authors constructed a quantum potential and demonstrated the existence of states that remained completely bound despite having energies within the continuum of free particles. This defied conventional wisdom as all bound states ought to either leak energy to radiation or have energies outside the continuum. However, the concept applies to all fields of wave mechanics including optics [93]. Many systems with symmetry support BICs.

True BICs are theoretical constructs that do not exist. Only infinitely large structures support BICs. Real structures must be finite in size and contain imperfections. Both of these qualities increase the free space coupling. By slightly breaking the symmetry of the structure, the modes obtain a small free-space coupling. The modes in these metasurfaces are an example of quasi-bound states in the continuum (qBICs).[93, 94] They are ideal for our purposes in which we want to control the free-space coupling.

Symmetry-protected BICs are characterized by a small parameter δ that describes the magnitude of the symmetry breaking. A nonzero δ corresponds to a broken symmetry. It can be shown that this produces a coupling to free-space radiation $\gamma_{rad} \propto \delta$ [94]. By temporal coupled mode theory, the quality factor Q is proportional to γ_{rad}^{-2} and thus [95]

$$Q_{rad}^{-1} \propto \gamma_{rad} = C\delta^2 \tag{5.16}$$

where C is some constant determined by the geometry of the structure. By selecting the magnitude of δ, one can tune γ_{rad} and maximize tunability. In addition, if high emission power is desired, one can match the radiative and absorptive rates in what's known as the

critical coupling condition $\gamma_{rad} = \gamma_{abs}$.

The first BIC modes were observed in a Si_3N_4 metasurface.[96] BIC modes have been demonstrated in silicon metasurfaces and photonic crystals.[97, 98] BIC modes have been used for molecular identification.[99] In addition, some of the highest Q free-space modes have been demonstrated with BICs fabricated from monocrystalline silicon.[100] BICs have even been used for lasing.[101] There is precedence for being able to use BICs for a practical application.

5.5 Dimerized High-Contrast Gratings

One of the simplest metasurfaces supporting BICs is the high contrast grating (HCG). The HCG is a grating of rods made of high-index material (Si or Ge) in a low-index environment. These gratings are known to support a multitude of interesting modes whose frequencies, wavevectors, and field profiles can be solved for analytically [102]. HCGs have been used to make extremely narrowband transmission filters [103]. The BICs in this structure are symmetry-protected and can be accessed by investigating light incident slightly off normal [103, 104] or by perturbing every second rod in the grating [95, 105]. In the latter case, the unit cell doubles in size and the structure becomes known as a dimerized high contrast grating (DHCG). There are two easily fabricable methods for making this perturbation. If the width (gap) of the rod is perturbed, it is known as a w-DHCG (g-DHCG). Being a symmetry-breaking BIC, the small parameter δ is the magnitude of the change in rod width (rod position). Both of these DHCGs are studied in detail by Overvig et al [95]. Here, we review the same concepts using a fabricable structure with a backreflector and comment on how the physics changes.

Overvig et al. considered DHCGs isolated in free space. Here we will investigate the physics of DHCGs in the context of a fabricable structure. Figure 5.4a shows a high contrast grating made of silicon separated from a Au backreflector by a spacer layer of SiNx. We fix the spacer layer at 2 microns. By varying the spacer thickness D, we see that there are modes dispersing in the structure.

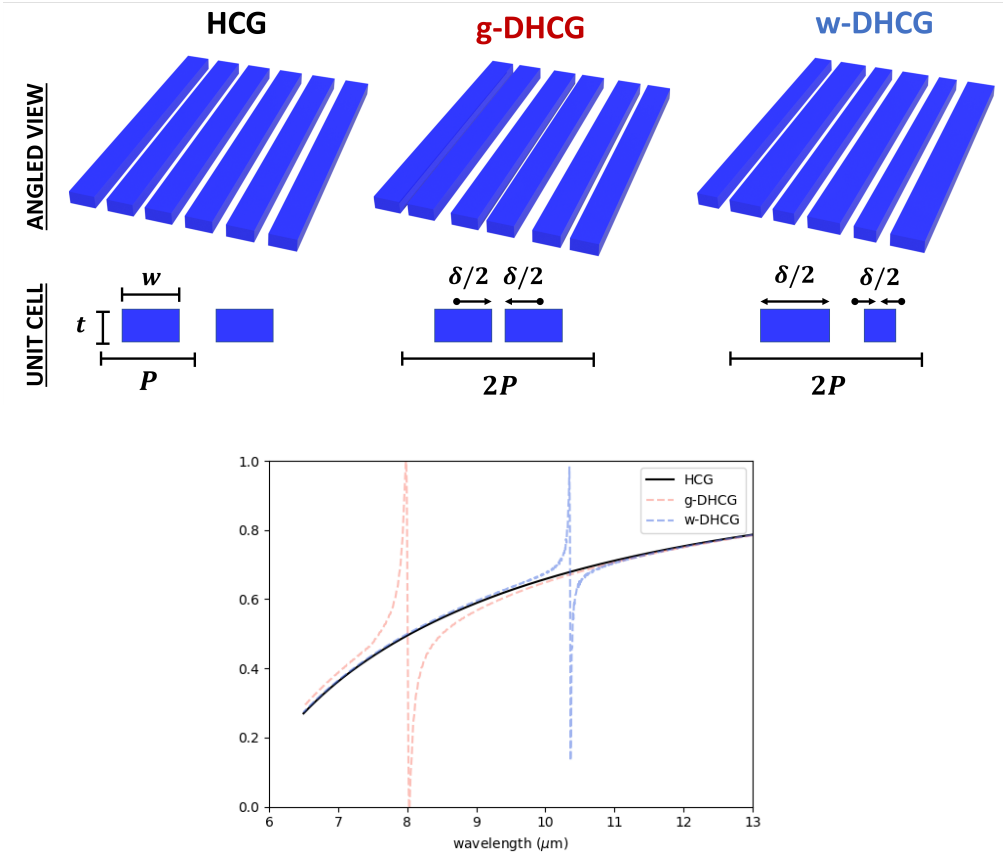

Figure 5.3: a) High-contrast grating (HCG) of period P, rod width w, gap size $g = P - w$, and rod height t compared to the two types of dimerized high-contrast gratings (DHCGs). Period has doubled due to perturbation of every other rod. For g-DHCGs each rod moves by $\delta/2$. For w-DHCGs, one rod widens by $\delta/2$ and the other shrinks by $\delta/2$. b) Simulated reflection spectrum of normally incident TE polarized light on gratings made of silicon. ($P = 3.75$ μm, $w = P/2$, $t = P/10$,$\delta = P/10$)

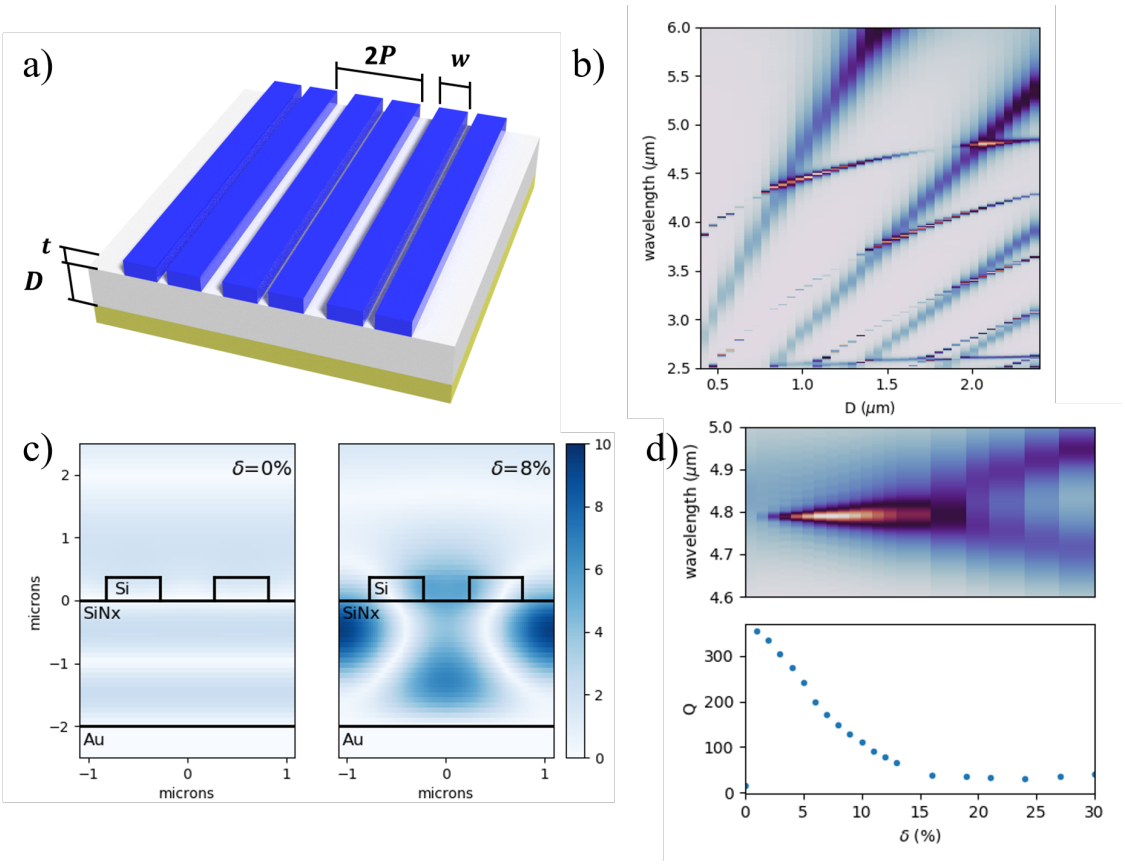

Figure 5.4: a) Fabricable DHCG consisting of Si grating on SiNx spacer and Au backreflector. Si handle wafer not shown. b) Absorption spectrum as a function of D when $\delta = 8\%$. c) Electric field magnitude $|E|$ of the modes at $\lambda = 4.807$ μm for $\delta = 0\%$ and $\delta = 8\%$

The tunability of DHCGs was explored theoretically by Overvig et al. in the form of a refractometric sensing device [95]. In this work, a simulated device of a Si DHCG on a SiO_2 substrate was shown to detect a change in refractive index of the surrounding medium of $\Delta n = 0.0008$. The peak shifted one full width.

In TE polarization, this structure hosts two types of modes (5.4b), broad Fabry-Perot modes and waveguide modes. The Fabry-Perot mode disperses linearly with D. The waveguide modes follow a square root dependence. The field profile (Figure 5.4c) for both $\delta = 0\%$ and $\delta = 8\%$ shows that the dimerization causes a coupling from free-space to a waveguide mode. Notice that for $\delta = 0\%$, the incident light hardly interacts with the structure, reflecting nearly 100% efficiency. For $\delta = 8\%$ we see a strong mode excited by the coupling with free space.

Operating in TE polarization provides an advantage by lowering the loss. As can be seen, the field at the Au backreflector is zero. There is therefore no opportunity for loss in this material. Though we would like to avoid using plasmonic materials, this configuration allows us to avoid any absorption in the material.

Figure 5.4d shows the absorption spectrum while varying δ. Varying δ while measuring the Q, the characteristic δ^{-2} dependence is apparent up until $\delta = 8\%$. At larger δ, the small perturbation assumption begins to break down. At smaller δ, the absorption in the structure dominates and sets a limit to the Q.

Chapter 6

Tunable Symmetry-Protected Dielectric Metasurfaces

6.1 Design Considerations

The previous sections discussed the theoretical properties of DHCGs. This section discusses the fully fabricable and tunable DHCGs. We begin by considering the material and design choices, then move to the fabrication and its associated challenges. We end with reports of FTIR spectroscopy measurements of successfully fabricated devices.

6.1.1 Spacer Material Choice

As discussed in the previous chapter, DHCGs are made of a high-index material ($n > 2.5$) yet require a low-index ($n < 2$) near-field environment. This precludes the idea of directly etching DHCGs into a Si or Ge wafer. Such a structure simply does not support BICs and rather is known as a low-contrast grating (LCG).[95] Therefore supporting the DHCGs on a low-index dielectric substrate is crucial. In addition, in order to maintain a narrow linewidth of the BIC, the spacer must have low loss as can be seen in Eqn. 5.12. The graphene must also be physically separated from the back gate in order to form the parallel plate capacitor. All of these criteria may be solved by placing the DHCGs on a low-index spacer layer. Many oxides and nitrides satisfy the criteria. Possible materials include SiO_2, Al_2O_3, HfO_2, Si_3N_4, and TiO_2. The choice of spacer material comes down to two criteria: loss and ease of fabrication.

Loss will set the range of possible operating wavelengths. All of these dielectrics have a phonon in the MIR which causes significant loss at longer wavelengths. This loss reduces the maximum tunability of the final structure and it is therefore preferred to operate at a shorter wavelength (see Section 5.3). For silica (SiO_2), the loss begins around 7.9 μm.[106] We would therefore expect a silica spacer to only work at wavelengths shorter than 7.9μm. Silicon nitride (Si_3N_4) begins to have significant loss at around 5 μm would therefore have a much more limited range of operation.[106] Conversations with collaborators at the Naval Research Laboratory revealed that HfO_2 has its loss beginning near 9 μm. This thesis uses SiO_2, but to move deeper into the MIR, different spacer materials would be needed.

All of these low-index dielectrics are compatible with different fabrication processes and have varying qualities after fabrication. Evaporation can be used to deposit SiO_2, Al_2O_3, and TiO_2. This is generally a dirty process leaving many pinholes which will short the graphene to the backgate. Atomic layer deposition is a valid method for SiO_2, Al_2O_3, HfO_2, and TiO_2. However, our designs will require spacers on the scale of microns making the slow ALD process impractical in most cases. For example, HfO_2 deposits the fastest at 1 μm/day. Plasma-enhanced chemical vapor deposition (PECVD) is a valid method for both SiO_2 and Si_3N_4. However, the resulting films can be low in quality. High-quality membranes of SiO_2 and Si_3N_4 can also be purchased from Norcada, Inc. However, SiO_2 is only available with membranes 50 μm in diameter. In summary, with evaporation being too dirty and ALD being too slow, this left only SiO_2 deposited via PECVD or Si_3N_4 purchased as a membrane. In this thesis, SiO_2 was the spacer of choice. The relatively low loss leaves a large range of possible operating wavelengths. The compatibility with Si in fabrication processes is favorable. If in the future this device requires operation at longer wavelengths, choosing a different spacer will be crucial.

6.1.2 Backreflector and Backgate

As described in Sec. 5.2, a conducting substrate is required to form the parallel plate capacitor which tunes the graphene. The material choices for this back gate are either doped Si or

a noble metal such as Au. Both carry advantages and disadvantages. Using a silicon back gate offers the opportunity to use thermally-grown SiO_2 which is of higher quality and can have a higher breakdown voltage than SiO_2 spacers deposited with other methods. It is also smoother, which is important for the incorporation of graphene, as discussed in Section 6.2.3. However, the proximity of the Si handle wafer does not support BIC modes.

Consider the fabricable DHCG in Figure 6.1a. The dimensions of this BIC were chosen such that the Si was thin enough for practical fabrication and the BIC would be resonant at wavelengths shorter than the phonon peak in SiO_2. In Figure 6.1b we show the absorptance spectrum of normally incident TE light as simulated in Lumerical FDTD. A BIC mode is visible at $\lambda = 5\,\mu$m for SiO_2 thicknesses $D \geq 600$ nm. However, when $D = 300$ nm, this mode is all but gone. This highlights the need for BICs to have a low-index near-field environment. In Figure 6.1c is the absorptance for various δ at $D = 1200$ nm. We see that changing δ does not provide enhanced absorption. It appears that in this structure, the absorption maximizes around 2%. This can be significantly improved.

Enhanced absorbed is found using a Salisbury screen-like geometry. This geometry places a two-dimensional material one quarter wavelength away from a conducting plane.[107] It was proposed in Ref. [108] and later demonstrated in Ref. [109] that such a geometry could significantly enhance the absorption in graphene. In our case, we can use a backreflector of Au. Placing a dimerized grating on top will alter the exact optimal spacer thickness D, but we know that it will need to be on the scale of microns.

This geometry has a second advantage of supporting stronger BIC modes. Being a reflector, the Au "hides" the Si. It allows for the *critical coupling condition* to occur, in which the radiative rate is equal to the absorptive rate.[90] In this thesis, we therefore choose to use a Au backreflector and back gate.

6.1.3 Optimizing for Tunability

The design choices made above were made with tunability in mind. We've chosen a structure exhibiting narrow resonances using low loss materials in a geometry that can be used to gate

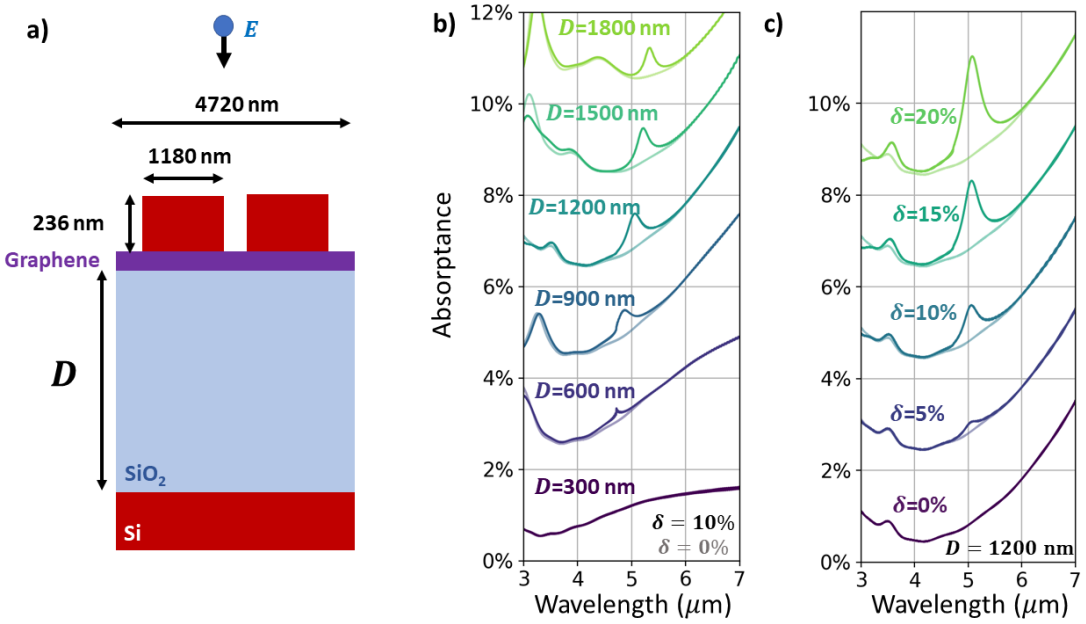

Figure 6.1: Fabricable DHCG demonstrating weak absorptance with a Si back gate. Graphene assumed to have mobility μ =650 cm/V-s and $E_F = 0.05$ eV. a) Schematic of the unit cell of a fabricable dimerized gratings on SiO_2/Si substrate with graphene. Light is normally incident at TE polarization. TM light did not exhibit a BIC mode for this device. b) Absorptance spectra for various thicknesses t and $\delta = 0\%$ or 10%. Solid (pale) lines indicate $\delta = 10\%$ ($\delta = 0\%$). Proximity of Si destroys the BIC mode at $\lambda = 5\mu$m. c) Absorptance spectra for various δ assuming $D = 1200$ nm. Absorptance increases with δ, but still remains low at about 3%.

graphene. Choosing the exact parameters for the DHCGs is next. With many factors at play determining the tunability of the device, it was prudent to use an optimization algorithm to determine the optimal parameters.

A parameterization of the structure is shown in Figure 6.2a. Recall that the parameter to be optimized, or figure of merit (FOM), is the tunability T defined as

$$T = \frac{\Delta\omega_0}{\gamma} = \frac{\omega_0(\beta_1) - \omega_0(\beta_2)}{\gamma} \tag{6.1}$$

as discussed in Section 5.3. Most optimization algorithms define a FOM and differentiate it with respect to the parameters to use gradient descent alrogithms. In this case, the FOM is not easily differentiable. Colleague Juho Park of the Korean Advanced Institute of Science and Technology (KAIST) used an optimization algorithm known as *Bound Optimization by Quadratic Approximation.*[110] For this optimization, graphene was assumed to have a mobility of $\mu = 650$ cm^2/V-s and to tune from $E_F = 0.05$ eV to $E_F = 0.6$ eV. Period was P was bound to 2-4 μm so that the resonant wavelength would fall between 4-8 μm, appropriate for SiO_2. Perturbation δ was bound to 0-30% and the smallest gap was bound to be >100 nm. This optimization resulted in Design 1 in Figure 6.2b. It resulted in a tunability $T = 2.0$. This is a strong result as it allows for fabrication imperfections while still maintaining a tunability above 1.

In the course of developing the fabrication process, it was found that the Si would need to be limited to <250 nm (see Section 6.2.3). For this reason, another optimization was run that held the Si thickness at 220 nm. This value was chosen it is below 250 nm and allowed for the possibility of using standard 220 nm SOI membranes. Since the MW2 had already been fabricated, we also held $D = 1778$ nm since the substrates had already been fabricated. This still allowed P, W, and δ to vary. The optimization resulted in Design 2 with a tunability of 1.84. This design was used in the sample known as **Tunable Test Device 1**. See Section 6.3.3 for measurement results.

It turns out TTD 1 did not show any BIC modes. The culprit appeared to be the low index of Si. We therefore performed a third optimization using an index of $n = 2.6$. This

a)

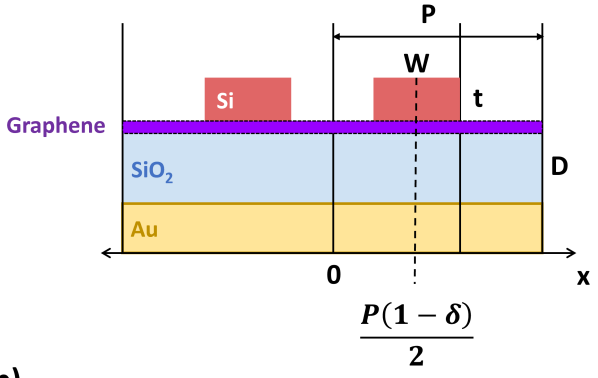

b)

Design	P (nm)	D (nm)	t (nm)	w (nm)	δ (%)	Tunability
1	2160	1778	595	1520	4.22	2.00
2	2360	1778	220	2030	5.50	1.84
3	2550	1778	220	1630	10.2	1.57

c)

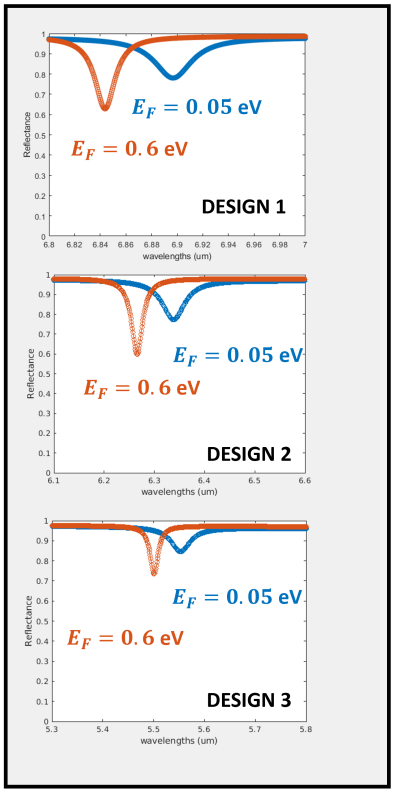

Figure 6.2: Optimization of a tunable DHCG structure. a) Schematic of the unit cell used in the optimization of the structure b) Table of parameters for the optimal structures. Optimization of Design 1 allowed Si thickness t to range from 50 nm to 2 μm. Optimization of Design 2 restricted t to 220 nm. Optimization of Design 3 changed $n_{Si} = 2.6$. c) Reflection spectra at TE polarization for Design 1, Design 2, and Design 3 at different E_F.

resulted in Design 3 and the sample called **Tunable Test Device 2**. Section 6.3.3 has FTIR measurement results.

6.2 Fabrication

The final device is shown in Figure 6.3. The parameter variable names are the same as those defined in Figure 6.2. We also include two optically insignificant 10 nm layers of Al_2O_3 to enhance the dielectric breakdown voltage. In this section, we cover the entirety of the fabrication process and the details behind the decisions made. We also cover steps in the process that failed and what was changed to overcome those challenges. A step-by-step instruction list is available in Appendix B.

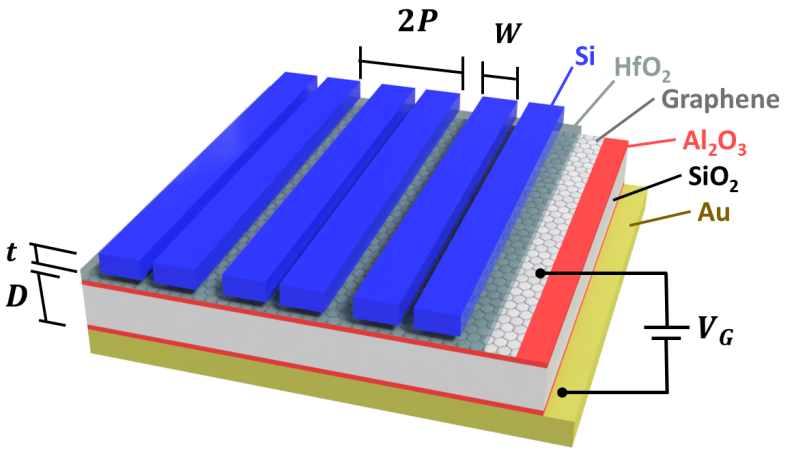

Figure 6.3: Schematic of the final device. Parameters used are either from Design 1 or Design 2. Layers of Al_2O_3 are only 10 nm and are optically insignificant.

6.2.1 Master Wafers

The fabrication of the Au backreflector and most of the Al_2O_3/Au/Al_2O_3 spacer layer can be done on an entire wafer. For this project, two *master wafers*, referred to as MW1 and MW2, were fabricated to provide these substrates. Fabrication begins with a 100 mm Si(100) handle wafer as this orientation allows for square dicing later on. The wafer is first cleaned in a spin-rinse-dryer (SRD). After being blown dry to remove any potential water or dust, the wafer is placed in a metal evaporator for deposition of the Au backreflector. First, a 2 nm thick layer of Ti is deposited as an adhesion layer. Next, a 150 nm layer of Au is deposited. Finally, this is capped with another 2 nm Ti adhesion layer. This layer is crucial for the subsequent layer to stick.

The spacer layer fabrication now begins. The wafer is placed in an atomic layer deposition (ALD) tool and a recipe of thermal Al_2O_3 is run at 250°C for 96 cycles resulting in a nominal thickness of 10 nm. This ALD layer offers a cap that ought to prevent pinholes in the spacer that could cause shorts to the backgate. The bulk of the spacer layer is made of SiO_2. This was deposited via plasma-enhanced chemical vapor deposition (PECVD). The PECVD was run using the recipe *Si Oxide* for 1135 seconds for MW1 targeting 1180 nm and 1835 seconds for MW2 targeting 1775 nm. This step ends the parallel processing.

The wafers are then diced into 1 cm x 1 cm squares on the Disco Dicing Saw. An image of MW1 after dicing is shown in Figure 6.4a. Each die from MW1 and MW2 had its SiO_2 thickness measured in a reflectometer, the results of which are shown in Figure 6.4b-c. For both wafers, there is variation in the thickness of over 100 nm. On die for which the thickness is too large, a plasma etch is necessary. The reactive ion etcher (RIE) has a recipe *50CHF3*: CHF_3 at 50 sccm, O_2 at 20 sccm, at an RF power of 150 W and etch pressure of 100 mT . This recipe will etch the SiO_2 at a rate of about 25 nm/min. We etch the die to 10-30 nm below their final intended thickness. This leaves space for the capping layer of Al_2O_3. This is then put on top to the desired final thickness D, in this case 1778 nm. If the SiO_2 thickness begins below the target, the RIE etch is skipped and the ALD capping layer is performed to the desired thickness. It's often prudent to run etch and ALD steps in parallel on many die similar thicknesses of SiO_2. After this stage, the die are ready for graphene.

6.2.2 Graphene, Bondpads, and Hafnia protective layer

The graphene is placed on the die once the ALD capping layer of Al_2O_3 has been deposited. Graphene is grown in a CVD oven on Cu foil and transferred.[111] Once the graphene is placed, bond pads may be evaporated. A hard mask is used for this step, rather than performing a EBL step. The middle two columns of holes are masked off with kapton tape leaving only the edge pads. Kapton tape is used to hold the sample on the stage. The hard mask is placed over the sample, taking care to rest it on the tape such that it does not touch the sample, and to align the open holes to the edges of the graphene. Then 2 nm of Ti and 100 nm of Au are evaporated on the die. After venting, the hard mask is removed and the bondpads are complete.

Our methods of depositing Si gratings require plasma etches (see Section 6.2.3). Graphene would be destroyed if exposed to the plasma for any amount of time. For this reason a protective layer is required. Just 5 nm of Hafnia (HfO_2) was found to be an ideal protective layer. To test its durability, an etch test was performed (see Figure 6.5). Two samples from MW1 were placed in the ALD and 20 nm of HfO_2 was deposited. Next, a 20 nm layer of Cr

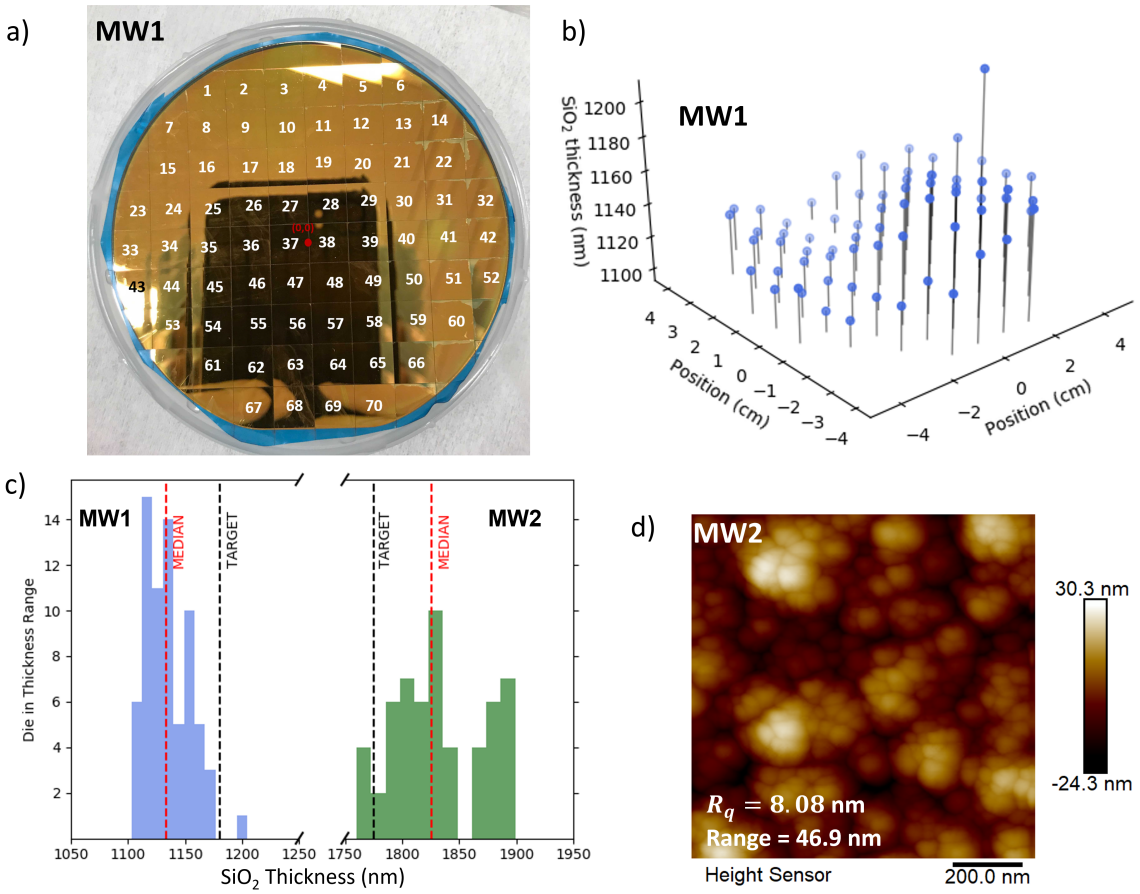

Figure 6.4: Resulting PECVD SiO_2 deposition on master wafers. a) Image of MW1 with all 70 die labeled. b) Thickness of SiO_2 on each 1 cm die on MW1 as a function of position on the wafer as measured on a reflectometer. c) Histogram of thicknesses for MW1 and MW2. d) AFM image of PECVD SiO_2 sample from MW2.

was deposited with the clip forming a mask. This left some HfO_2 exposed. The samples were then placed in a RIE using the recipe which would later be used to etch the Si. This recipe (*SiTemp25*) has an etch pressure 8 mT, RF power 25 W, 42 sccm of SF_6, and 5 sccm O_2. The thickness of the Cr/HfO_2 step edge was measured before etching, after a 3 minute etch, and after another 5 minute etch. In this way, we were able to determine the etch rate difference between Cr and HfO_2. Since Cr is known not to etch in most plasmas, we assumed the etch of Cr to be zero. In summary, it was found that HfO_2 had an etch rate of <1 nm/min using the recipe *SiTemp25*. Another test revealed that Si etches at >20 nm/min. This selectivity of at least 20:1 makes HfO_2 ideal as a protective layer for the graphene.

In addition to this etch test, it was prudent to ensure the graphene would still be conductive after experiencing a plasma, even with the protective layer. Bondpads were deposited on a sample of graphene on a SiO2/Si. It was confirmed that the graphene conducted and that the Si back gate was operational. Next, the sample was placed in the RIE with recipe *SiTemp25* for 1 minute. The graphene and back gate were still operational after this test. With 5 nm HfO_2 identified as a strong protective layer, we began using this on the samples.

6.2.3 Silicon Grating Deposition

After the graphene is fully protected by the hafnia, deposition of Si gratings is the next step. There are many possible methods for putting patterned Si on the surface. Low-pressure chemical vapor deposition (LPCVD) can produce high quality Si and has even been used to demonstrate BIC modes.[99] However, the process requires temperatures in excess of 500°C. This would cause the Au back reflector to sinter and crack. Another silicon deposition method is PECVD. However, this requires 100% silane which is not suppported by UW-Madison's facilities.

Another method involves transferring silicon membranes from a silicon-on-insulator wafer.[112] This method is tempting because the silicon is monocrystalline. Such silicon has demonstrated some of the highest Q BIC modes.[100] Attempts to fabricate the device using the transfer method were unsuccessful, however. Physical vapor deposition (PVD) methods

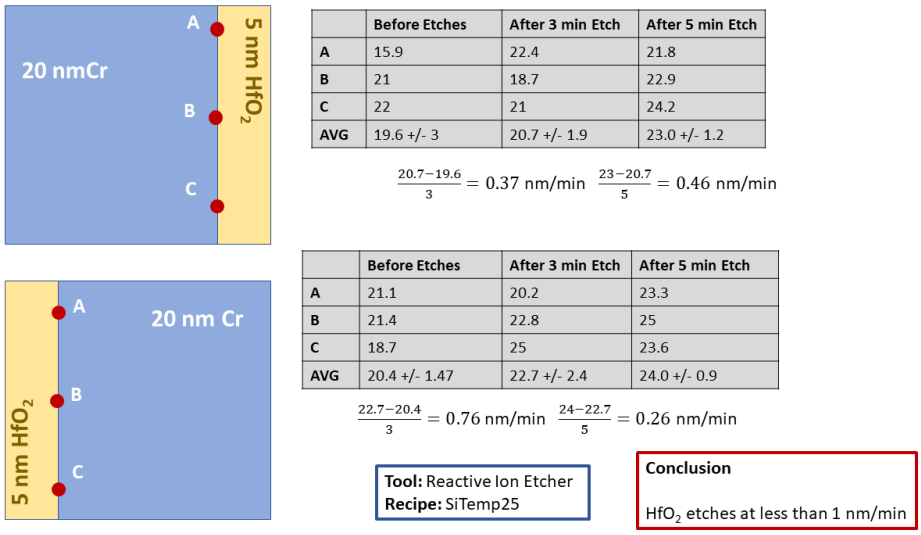

Figure 6.5: HfO_2 etch test. Atomic layer deposition was used to deposit 5 nm of HfO_2 on top of a SiO_2/Au substrate from MW1. A 20 nm Cr layer was then deposited on top with the clip leaving a step layer leaving some HfO_2 exposed. The samples were placed in a reactive ion etcher (RIE) for 3 minutes and then 5 minutes with the step height being measured at each stage. It was found that HfO_2 had a minimal etch rate.

such as sputtering and electron-beam evaporation are the final possible methods. Sputtering was not attempted in this work. In the rest of this section, two different electron-beam evaporation-based methods we call *Blanket Si* and *Liftoff Si*.

Blanket Si

Blanket Si refers to the deposition of Si on an unpatterned substrate followed by the patterning of a resist on top of the Si to define the grating. A layer of Cr is then deposited in a metal evaporator on top of the resist and lifted off to define a hard mask. Subsequently, the Si is etched with a plasma and the Cr is then stripped using an etchant. The Blanket Si process is shown in Figure 6.6. This process was successful on samples without graphene.

One device fabricated with this method was named the **Non-tunable Test Device (NTTD)**. No graphene was incorporated into this structure, hence referring to it as "non-tunable". It was designed to have a doubled period $2P = 4\,\mu$m, bar width $W = 1200$ nm, and perturbation $\delta = 10\%$. This pattern covered a full 4 mm by 4 mm area on the chip. It was fabricated with a die that came from MW1 (see Section 6.2.1). The thickness of SiO_2

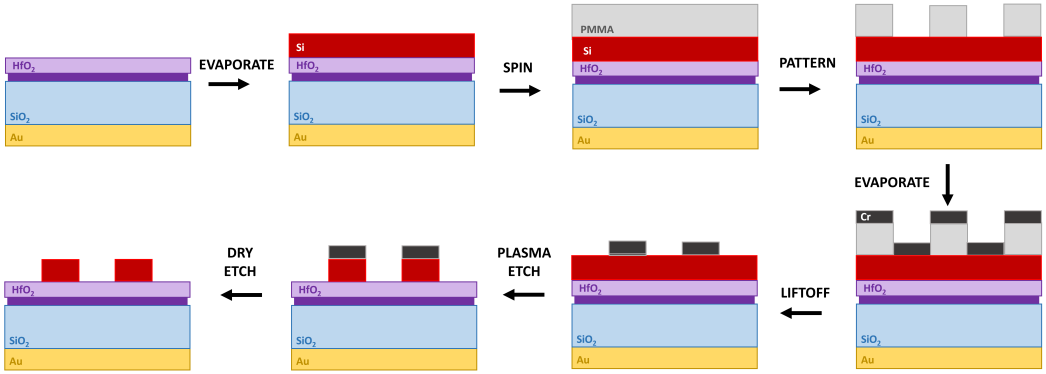

Figure 6.6: The Blanket Si procedure. A layer of Si is deposited directly onto the HfO_2 coating the graphene. A layer of PMMA is then patterned on top and Cr is deposited above creating a hard mask. The Si is then etched in a RIE and Cr is etched in a chrome etchant.

was measured at 1108.5 nm. After the evaporation step, the Si thickness was measured at 331 nm via profilometry. A two-layer stack of PMMA was used for patterning: PMMA 495 spun at 4000 RPM for 1 minute with a 90 second bake at 180° C followed by PMMA 950 with the same treatment. For e-beam lithography, a 5 nA current was used. Development was done in a 3:1 IPA:MIBK mix for 90 seconds with a 15 second IPA rinse followed by a blow-dry. A 20 nm Cr layer was deposited with e-beam evaporation and was lifted off using a 1 hour acetone soak at 40° C. It was then etched in the RIE with recipe *SiTemp25*, and the Cr was stripped with Transene 1020 Chrome Etchant for 80 seconds at 60° C.

SEM and AFM images of the NTTD are shown in Figure 6.7. Despite some large grains, the silicon appears to be of high quality. At the base of each bar, a small platform is visible. This is likely due to overetching. The SiO_2 surrounding the bars appears to have been etched slightly. Optical measurements of this sample are discussed in 6.3.2.

With the success of the NTTD, work moved ahead to creating a similar device incorporating graphene. As we discovered, Si naturally becomes highly strained when evaporated. This led to two major issues. First, it causes the quartz crystal monitor to underestimate the Si thickness during depostion. This leads to the deposition of excess Si if one is not careful to take this into account. However, this is generally solved by characterizing the deposition rate and adjusting the final thickness accordingly. The second problem is crinkling of Si.

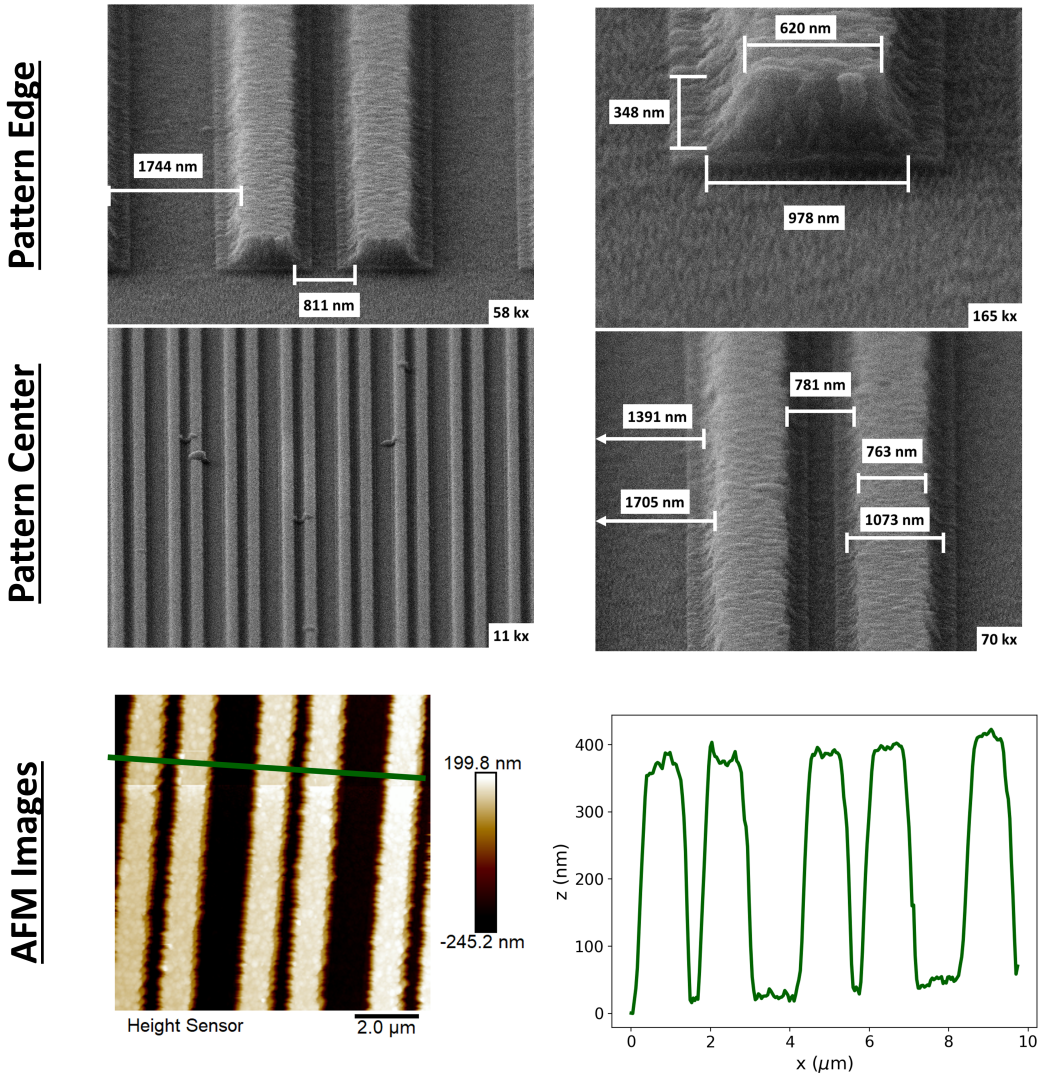

Figure 6.7: SEM and AFM images of completed NTTD which used the Blanket Si fabrication process. Overetching occurred during the Si etch, which is visible by the step edge surrounding the bars. SEM and AFM images agree thickness is about 350 nm.

Figure 6.8 shows evaporated Si on graphene with two different substrates, both of which have graphene. Figure 6.8a is a substrate from MW1 (i.e. SiO_2 deposited by PECVD) and graphene on top of this layer. In Figure 6.8b, it is clear that there is crinkling in a rectangular area. This area is exactly where the graphene is located. Clearly, DHCGs can not be fabricated on such a sample. We performed the same experiment on another substrate of thermally grown SiO_2 with graphene on top (Figure 6.8d-e). We see that crinkling is still present but improved. The Si does not crinkle over the entire area, and when it does, the magnitude is much lower. Graphene is known to adhere poorly to surfaces, especially rough surfaces.[113] In Figures 6.8d and f are AFM images of the PECVD SiO_2 from MW1 and the thermal SiO_2. Note that the PECVD-grown SiO_2 has 10 times the surface roughness. This appears to be the ultimate culprit for the difficulties depositing Si. Graphene simply does not adhere well to rough surfaces.

This problem needed to be solved in order to fabricate the final device. One approach could have been to develop a substrate with lower surface roughness. Atomic layer deposition of Al_2O_3 or some other low index dielectric is an obvious choice which could provide surface roughness lower than that of the PECVD SiO_2. But the crinkling on the thermal SiO_2, a nearly ideal substrate, indicates the problem wouldn't be fully resolved. We therefore chose to reduce the strain in the Si.

There were many possible routes for strain reduction. One theory was that the Si was too hot during and after deposition and that cooling the substrate would reduce differential strain. One quick fix attempt was to add a thermal mass of roughly 1 kg of Cu on the back of the sample carrier during deposition. This failed to fix the problem. However, since this step was inexpensive, all depositions after this used the thermal masses. Another theory was that slow deposition would work better by reducing strain. A sample had Si deposited at 1 Å/s but failed to adhere to the graphene as well. In addition, the slow evaporation increased the time and caused the sample to heat up. A 20 minute cooling period was insufficient as the sample would still be to touch after venting. It appears that a longer evaporation time allows the sample to rise to a higher temperature.

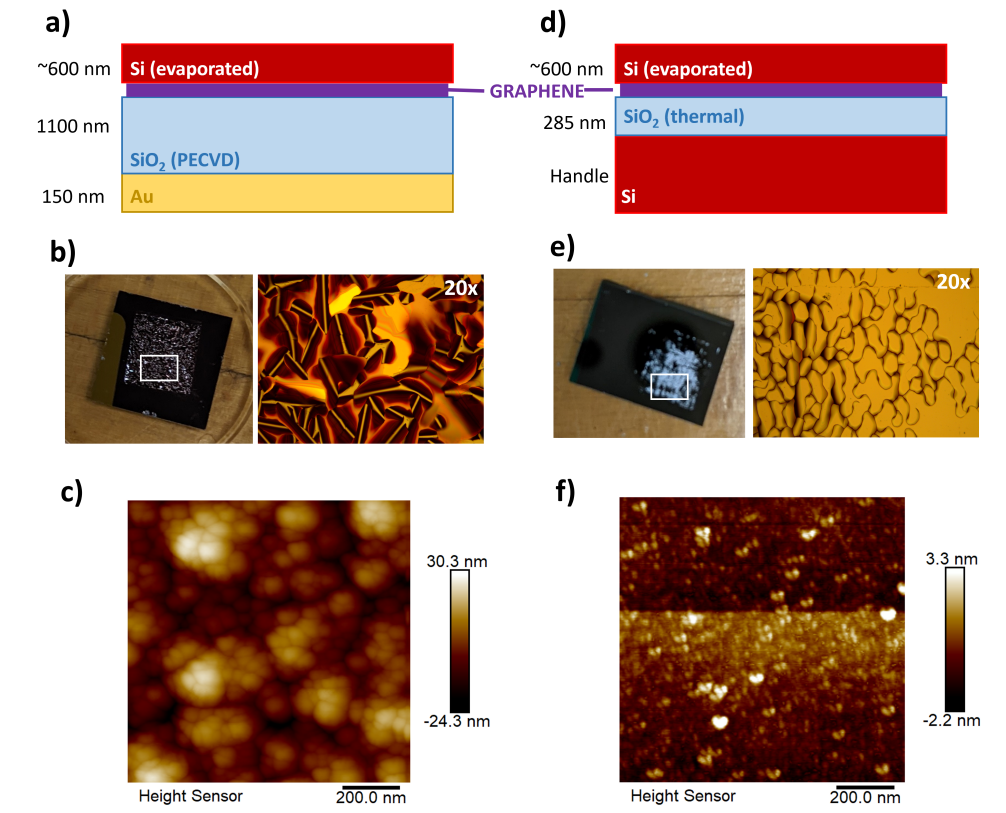

Figure 6.8: Comparison of Si deposition on samples containing graphene. On the left, graphene rests on a PECVD SiO_2 substrate which is about 10 times rougher than the thermal Si substrate on the right. The crinkling is noticeably worse on the left.

Another theory for the Si strain issue was that the cooling from a high temperature was causing a contraction creating the buckling. A possible approach to solving this is to evaporate in bursts. This means evaporating for a short time, allowing the sample to cool, and evaporating again. On a sample from MW2 containing graphene, silicon was evaporated 100 nm at a time four times in a row allowing a full 30 minute cooling period between each round. The chamber was also vented in between each round. Each evaporation was done at a rate of about 2.7 Å/s taking only 11-12 minutes. A profilometer measurement revealed that the final thickness was 502.3 nm. The sample did not crinkle after the final venting of the chamber, and so 500 nm of Si was successfully deposited on the graphene where it would have crinkled before. However, after approximately 48 hours, the Si begin showing large millimeter-scale defects. It was clear that the Si strain was reduced by this method, but not entirely.

With the relative success of the Si burst technique, two more samples were fabricated from MW2. On these samples, the burst technique was used doing three Si depositions of 100 nm, 125 nm, and 125 nm as read by the QCM. All depositions were performed at 2.8 Å/s and allowed for a full 30 minutes of cooling. At the end, the samples measured at 497.3 nm and 470.9 nm, respectively. The first sample was put in for a fourth deposition of 98 nm. The samples appeared to survive. However, once PMMA was spun on, the Si crinkled. It seems that liquid underneath the surface of the Si is a major culprit in initiating the crinkling.

Discussions with Professor Max Lagally made it clear that the thickness of Si was causing excess strain. We switched from Design 1 to Design 2 as described in Section 6.1.3. A sample was made to test this. Si was evaporated at 2.8 A/s. The fast evaporation kept the sample cooler. This evaporation also used an Alloy QCM.The evaporation was run under the assumption that the Alloy QCM would accurately measure the Si thickness, so the evaporation was stopped at 220 nm on the QCM. A profilometer reading revealed that the final thickness was 355 nm. A 2 minute and 30 second etch using *SiTemp25* reduced the thickness to 223 nm. The sample was patterned for Design 2 with a bilayer stack of PMMA 495 A4 then 950 A4 each spun at 4000 RPM and baked for 90 seconds at 180° C. A Cr

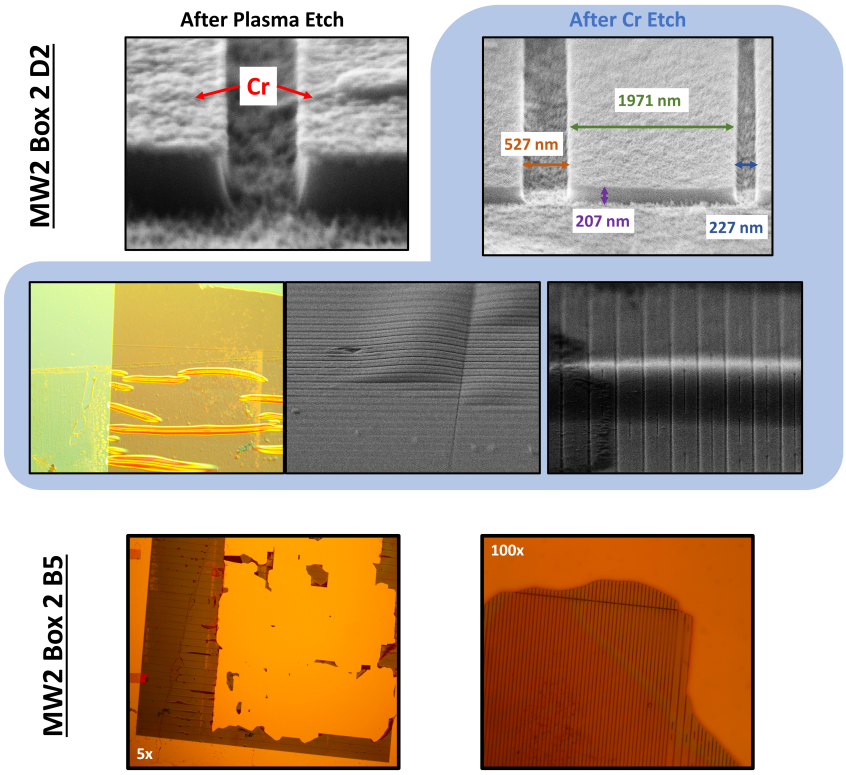

Figure 6.9: Images of the MW2 Box 2 D2, the first sample which used Design 2. Si bars looked good except for delamination caused by longitudinal strain.

layer was evaporated and lifted off to define the hard mask. The sample was dry-etched for a total of 5 minutes and 40 seconds before having the Cr etched. After Cr etching, wrinkles appeared in the Si. This can be seen in the top section of Figure 6.9. Some fluid is also visible underneath the wrinkles. The wrinkles are much longer perpendicular to the bars indicating longitudinal strain is the culprit. It appears that either the Cr was keeping the Si bars down, or the liquid encountered during the dip caused the release of the Si bars from the surface.

The next sample (MW2 Box 2 B5) used the same recipe but with measures to reduce the strain. A slower evaporation at 0.5 Å/s was performed. In addition, breaks were added to the bars every 100 μm. These measures only had the effect of lowering the adherence of the Si to the surface (lower section of Figure 6.9). The bars ripped off.

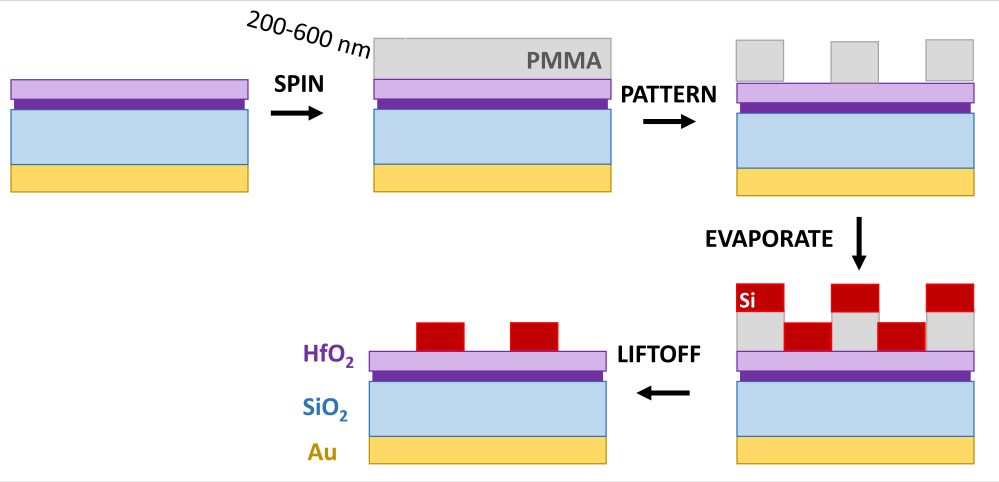

Figure 6.10: Liftoff Si procedure. Varying numbers of PMMA layers were used.

Liftoff Si: PMMA Only

With this issue seemingly unresolvable, we switched to a new method, *Liftoff Si*. Instead of depositing a blanket layer of Si directly on the HfO_2, this recipe calls for patterning the surface first with PMMA and depositing the Si on top. Anywhere from one to three layers of PMMA were used with varying levels of success. In this procedure, it was important that the Si thickness be less than the PMMA thickness so that liftoff in an acetone batch was possible.

With the measurement of the dimensions of MW2 Box 2 D2, we attempted to correct the overdosing by altering the design such that the small gap would be 80 nm larger and the large gap 120 nm larger. This is equivalent to changing $W \rightarrow 1930$ nm, a small gap of 280 nm, and a large gap of 580 nm. For fabrication, this sample used two layers of PMMA 495 A4 (spun at 2000 RPM for 1 minute and baked at 180° C for 90 seconds) followed by a layer of PMMA 950 A4 spun at 4000 RPM for 1 minute and baked at 180° C for 90 seconds. The dose test used six doses from 900 to 2400 $\mu C/cm^2$. After Si evaporation (245 nm at 0.5 Å/s) and liftoff (RT acetone for 1.5 hours, 2 minute sonication), doses 1200 and 1500 $\mu C/cm^2$ looked best as SEM images revealed (Figure 6.11). The former appeared lower in quality, possibly due to insufficiently developed PMMA remaining in the gap before Si evaporation. The slight liftoff of the bars in the SEM images hints at this as well. The latter dose (1500

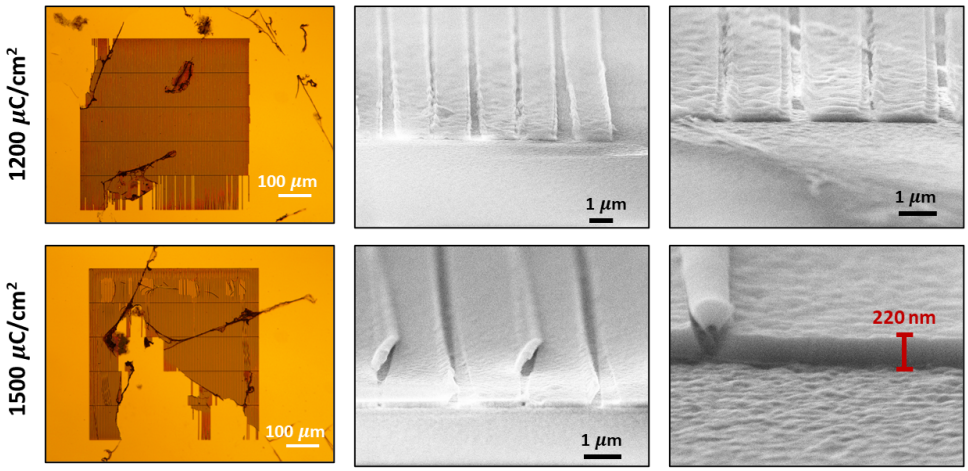

Figure 6.11: Results of the dose test on MW 2 Box 2 C3.

μC/cm^2) appeared to have higher quality Si, but the increased dose seems to have caused the small gap to close too much. It appears some material is still stuck in the gap. It is unclear whether this is PMMA or Si.

The SEM images of MW 2 Box 2 C3 in Figure 6.11 revealed further reduction of the bar width was required. For this next sample, the small gap was widened by 110 nm from the previous CAD file to a width 390 nm while the large gap was shrunk by 100 nm from the previous to 470 nm. The same spin recipe was used, although the PMMA 950 A4 was spun at 2000 RPM to thicken it and promote liftoff. Six doses from 1300 to 1550 μC/cm^2 were used.

We reduced the width of the bars a third time and switch to a single layer of PMMA 950 A4 spun at 1700 RPM (300 nm). During evaporation, the deposition rate became unstable and the evaporation was abandoned. The final thickness was measured at 177 nm in the SEM. The small gaps had some material (likely Si) stuck inside. After this sample, it was clear that PMMA alone would not be the method for depositing Si bars with a liftoff method, and a new method would be needed.

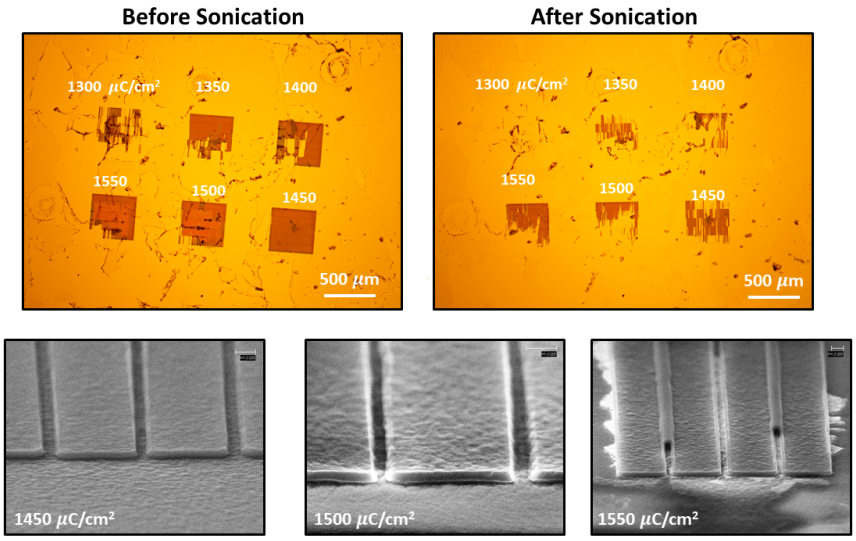

Figure 6.12: Results of MW 2 Box 2 C6 dose test.

Liftoff Si: HSQ on PMMA

After attempting to successfully create a device solely with PMMA we moved to a new type of Liftoff Si inspired by Ref. [114]. A schematic is shown in Figure 6.13. Instead of using only PMMA, we add a layer of HSQ on top. This layer is patterned and the PMMA underneath is etched with a plasma. We then evaporate Si and lift it off just as in the previous section. This procedure has a few benefits. First, HSQ is much thinner than PMMA and requires a lower dose. Second, most of our patterns have smaller gaps than bars, and this procedure calls for exposing the gaps instead. This reduces the change of overdeveloping due to backscattered electrons. Third, this procedure allows for a thicker PMMA layer without increasing the undercutting due to differential dosing of multiple layers. Finally, the etch of the PMMA is a softer etch which is less likely to breakthrough the protective HfO_2. Using this procedure, we were able to fabricate two devices with graphene.

The second device we call **Tunable Test Device 1 (TTD 1)**. SEM images are shown in Figure 6.14. The intended dimensions were those of Design 2. This device did include graphene, but did not exhibit any BICs or tuning. The device TTD 1 was the first sample with graphene on which Si gratings were successfully deposited. The substrate came from

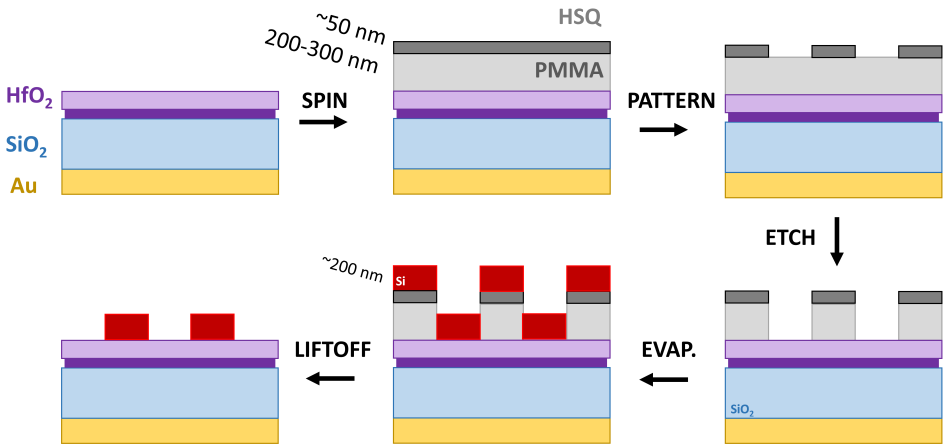

Figure 6.13: Fabrication process which led to successful deposition of Si bars on graphene.

MW2 (Section 6.2.1) and employed the HSQ on PMMA technique for Si deposition (Section 6.2.3). Optical measurements are discussed in Section 6.3.3.

The third device, and the second to successfully incorporate graphene, used the dimensions of Design 3 and is shown in Figure 6.15. We call this **Tunable Test Device 2 (TTD 2)**. AFM measurements showed that the final width of the bars was W =1812 nm as opposed to the intended 1630 nm. However, SEM images measured approximately 1560 nm. It's likely that the AFM tip caused broadening of this measuremement. A dimerization of $\delta = 9.8\%$ was found instead of the 10.2% in Design 3. Optical measurements of this sample are discussed in Section 6.3.3.

6.3 Measurements

6.3.1 Setup and Procedure

The emissivity, absorptance, transmissivity, and reflectivity of these devices can be measured via infrared spectrsocopy in an FTIR. Transmissivity is irrelevant for this thesis due to the presence of the backreflector. For this work a Bruker FTIR attached to a Hyperion 2000 microscope was used for spectroscopy measurements. For all measurements, a MCT detector was cooled with LN2 and allowed to reach equilibrium before operation. Reflection measurements occured on a microscope stage with light being collected through an objective

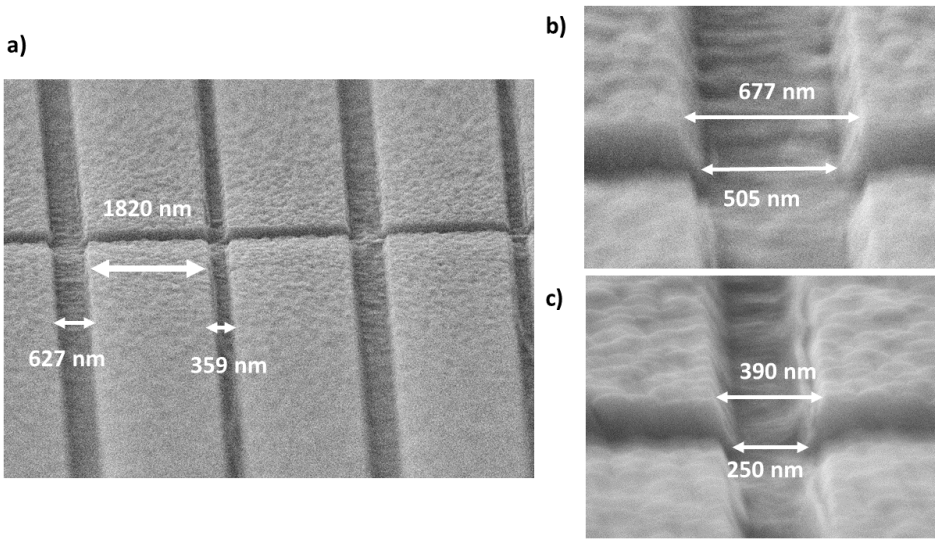

Figure 6.14: The TTD 1.

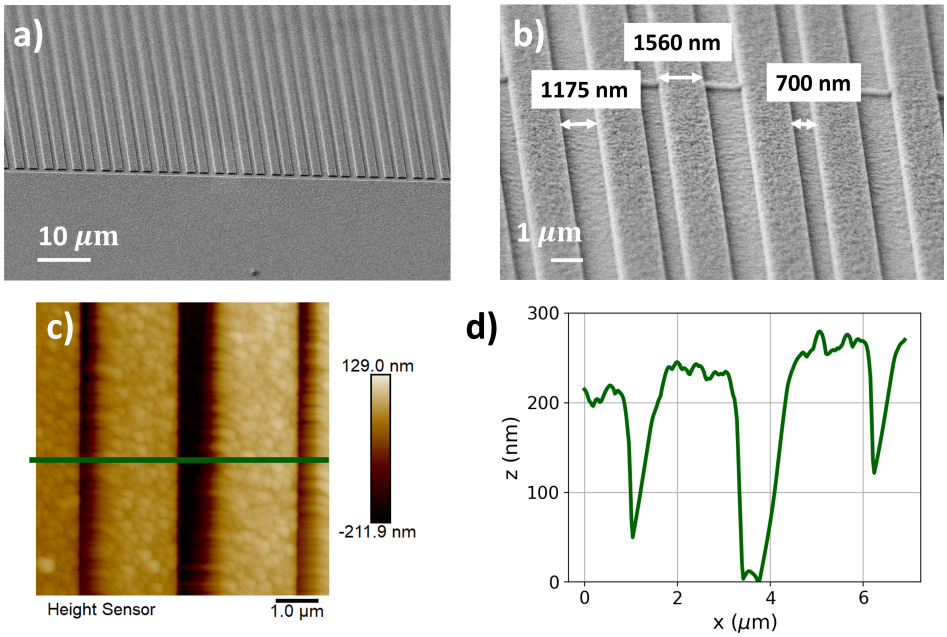

Figure 6.15: Images of the TTD 2. a) SEM image of the edge of the patterned Si of TTD 2. b) SEM image of the center of TTD 2. The bars were measured about 1560 nm. The gaps were measured at 1175 nm and 700 nm. The horizontal line is a stitching error and was not written into the pattern. c) AFM image of the TTD 2. d) AFM linecut showing height of 237 nm.

of NA=0.4. Light from 0° to 4° is rejected and so the objective collects light between 4° and 23°. Emission measurements occur by placing the sample in the chamber of the FTIR, in line with the optics. The sample is placed on a heating stage and heated to a temperature of $T = 150 - 300$°C. The resulting thermal emission is then collected by the optics and detected by the same MCT detector. In this section, we describe in further detail the measurements

Purging

The devices in this thesis operate in the same wavelength range as absorption lines for many common gasses in air. The most prevalent absorption lines are those of CO_2 near 4.2 μm and H_2O in the range of about 5 μm to 7.5 μm.[56] Sometimes, the system is purged with N_2 in order to remove these molecules. This is done by running tubing from a liquid nitrogen dewar to a port on the FTIR which allows gaseous N_2 into the system. A door opening to the FTIR chamber is sometimes forced to remain open due to wires leading to the heating stage. In this case, a plastic bag is taped over the opening. Similarly, the optical path passes through the microscope objective which sits in open air. A plastic bag is also used to cover this area and a line of gaseous N_2 is inserted.

Reflection Measurements

Reflection measurements provide a quick confirmation that the sample exhibits the desired spectral features. However, these measurements are often insufficient for the purposes of this project. Kirchoff's Law of Radiation states that absorptivity and emissivity at a particular wavelength and incident angle are equal, i.e. $E(\lambda, \theta, \phi) = A(\lambda, \theta, \phi) = 1 - R(\lambda, \theta, \phi) - T(\lambda, \theta, \phi)$. For this project, $T = 0$ due to the presence of the Au backreflector, and we have $E(\lambda, \theta, \phi) = 1 - R(\lambda, \theta, \phi)$. Unfortunately, the reflection and emission measurement setups collect different solid angles. The reflection setup uses a collector which accepts light at 4-23 degrees (NA=0.4). The emission aperture has an NA of about 0.05, according to discussions with Professor Mikhail Kats, which collects 0-3 degrees. We therefore cannot make any direct comparison between reflection and transmission measurements.

Above the objective, a polarizer can also be placed. This allows us to observe the TE and TM modes of the structure. There is freedom of choice for orienting the sample on the measurement stage. But for vertically oriented gratings, a polarizer position of $\theta = 0°$ ($\theta = 90°$) aligns with TM (TE) polarization.

Thermal Emission Measurements

As the ultimate purpose of this device is to provide a source of infrared light in the mid-infrared, we must perform thermal emission experiments. For these measurements, a sample is placed on a heating stage in the main chamber of the FTIR and the optics collect the resulting *total emission*. If instead *emissivity* is desired, a sample of carbon nanotubes (CNTs) is used as a blackbody reference and the signal is normalized to it.

Initial alignment of the measurement setup is important. Once the detector has been cooled, the CNT blackbody sample is placed in the measurement setup and heated to some elevated temperature. The total emission power is measured and displayed on a computer screen. We align the optics by maximizing the signal from the blackbody. The first alignment step is that of the microscope's transmission aperture located below the microscope stage. Due to internal misalignments, the blackbody signal is not maximized when this aperture is in focus. While watching the blackbody emission power, the focus and position of the aperture are adjusted until the blackbody signal is maximized. Next, the position of the blackbody itself is adjusted until the signal is maximized.

Measurement of the sample comes next. After alignment of the optics, the blackbody sample is often taken off and replaced with the sample. This is often done if one is uncertain whether a spectral feature. This saves the time of needing to do the blackbody measurements if there is no spectral feature present. Once the sample is placed on the heating stage, it is aligned and the spectra are measured. Once the signal of the sample is collected, blackbody measurements are required to measure emissivity. We repeat the above procedure with the blackbody ensuring that as little changes as possible.

Polarized measurements are required for observing the TE and TM modes. A polarizer

is put in the same slot in the microscope as for reflection measurements. However, while the reflection measurement polarizer is nicely aligned with the stage, this is not so for the emission measurements. An experiment was performed to determine the orientation of the polarization exiting the FTIR chamber relative to the microscope polarizer (see Appendix C). It was found that a polarizer orientation of $\theta = 37^\circ$ ($\theta = 127^\circ$) is aligned with vertically (horizontally) polarized light exiting the FTIR chamber. If the grating is oriented such that the bars are vertical, this corresponds with TE (TM) light.

DHCGs are know to exhibit a dispersive bandstructure.[95] That is, the resonant wavelength will vary with incident angle. By observing at specific angles, we can resolve this bandstructure. Spatially filtering (Figure 6.16) is a technique that provides more information about the angular dependence of the modes. By placing an iris near the exit port of the FTIR chamber, we can filter out light emitted at undesired angles. By moving the iris, we observe light emitted at different angles. Part of the work in this thesis was developing this technique.

After initial alignment of the internal optics using the blackbody, the iris is placed in the path of emission. The horizontal and vertical positions of the iris are modulated until the blackbody signal is once again maximized. Due to the reduced aperture size caused by the placement of the iris, this signal is much lower. The position of the iris is then recorded. Measurement of the sample then proceeds by moving the iris to different positions and taking spectra.

6.3.2 Measurement of Non-tunable Test Device

Work toward the fabrication of the final tunable device began with the NTTD described in Section 6.2. As described in that section, a nontunable device was chosen because evaporated silicon, while convenient, may have properties potentially detrimental to the perform of a photonic structure based on BICs. As we would later find out, depositing silicon on top of graphene is quite challenging in itself (see Section 6.2.3). Therefore, before measuring tunable dimerized grating emission, which carries the added challenge of incorporating the

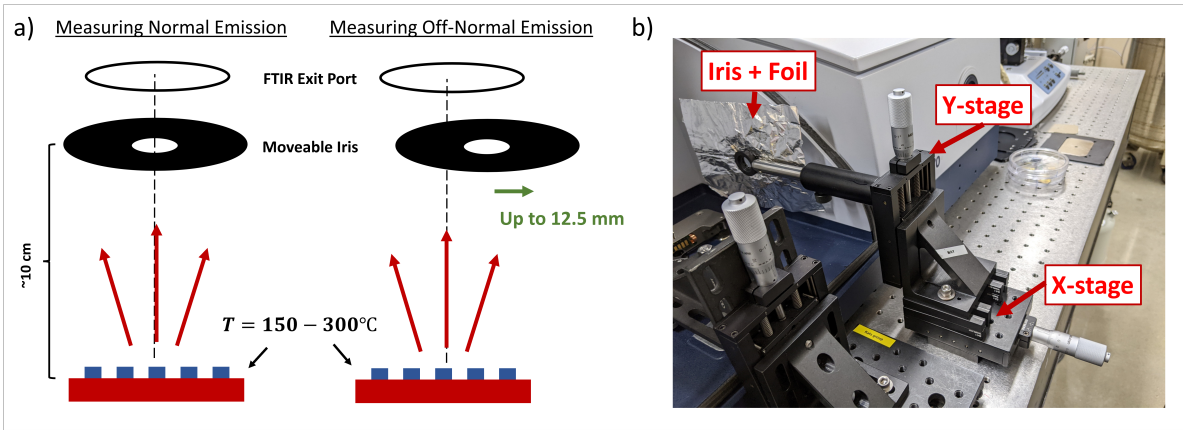

Figure 6.16: a) Schematic of spatial filtering. Thermal emission b) Image of iris set up on xy-stage. Two x-stages are put together at 90-degree angles to provide motion in both x and y. A piece of aluminum foil with a hole is placed on the backside of the iris to block thermal emission at greater angles.

graphene, it was prudent to test whether evaporated Si patterned into DHCGs would even support BIC modes. This section describes measurement of that device.

SEM images of the NTTD are provided in Fig. 6.7. This sample was measured using a non-purged reflection measurement as described in 6.3.1. Resulting spectra are shown in Figure 6.17. A mode is visible at 4.0 μm and is maximized when the polarizer is set to $\theta = 90°$.This orientation corresponds to TE polarization. Another TE mode is visible near 5.0 μm, with a mode visible in both TE and TM polarization at 5.4 μm. These results show qualitatively that a BIC modes are supported. Emission measurements will allow us to more accurately identify these modes.

Emission measurements are more easily matched with simulations. Spatially filtered emission measuresments were performed and we report on those in Figure 6.18. In TE polarization, two features are clearly visible at 4.1 μm and 5.0 μm, respectively. At an iris position of $x = 14.5$ mm, the feature at 4.1 μm appears maximized. The mode at 5.0 μm is a single peak at $x = 14.5\,\mu$m, but splits at other iris positions. Simulations were also performed at various angles of incidence and refractive indices for Si n_Si. Based on the wavelength of the secondary TE mode, it appears the index of the Si is between 2.2 and 2.4 with the closest match being $n_Si = 2.3$. The first TE mode does not match as well, but this could be due to

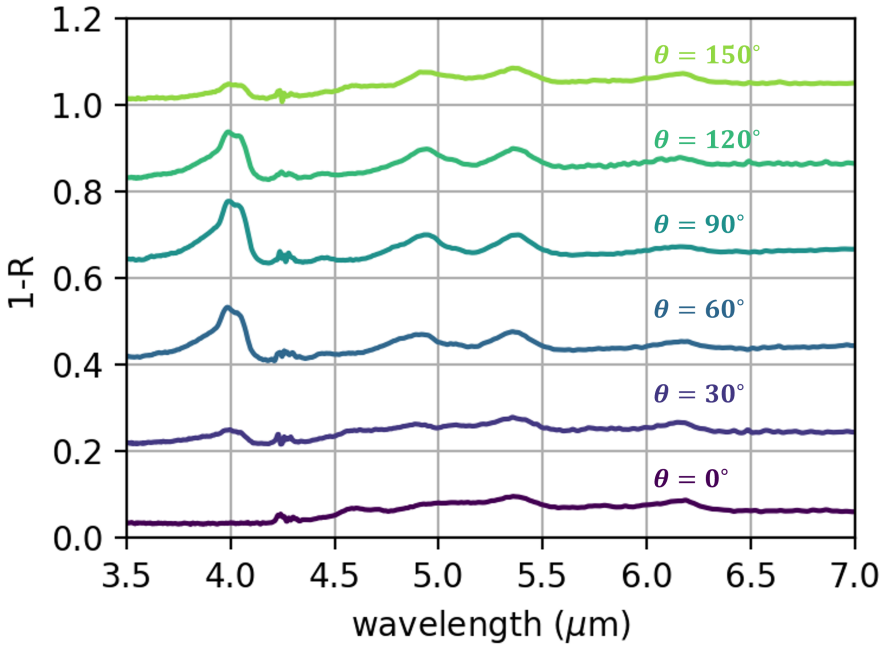

Figure 6.17: Results of polarized reflection measurement of the NTTD. Spectra for various polarization angles θ are separated by 0.2 for clarity.

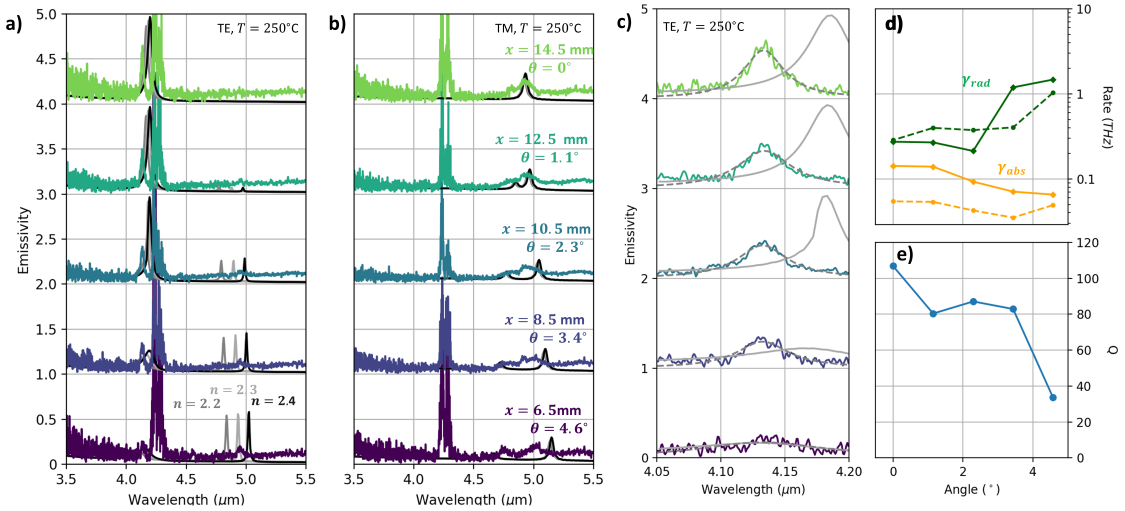

Figure 6.18: Spatially-filtered emissivity measurements of NTTD at 250°C. a) Measured emissivity in TE polarization at various iris positions along with simulated emissivity spectra assuming n =2.2, 2.3, and 2.4. b)Measured emissivity in TM polarization at various iris positions along with simulated emissivity spectra assuming n =2.2, 2.3, and 2.4. c) Short wavelength TE peak. Dashed lines are fits to Eqn 6.2 and solid line is simulation assuming $n = 2.3$. d) Parameters γ_{abs} and γ_{rad} at various angles. Dashed (solid) line indicates fit to experimental (simulated) spectrum. e) Measured quality factor Q at various angles.

slight difference in geometry between the device and simulation.

The resonance near 4.1 μm appears particularly strong. A zoomed spectrum is shown in Figure 6.18c. As the quality factor Q is of great interest for tunability, we use this peak to determine the quality of our device. We assume the peak near 4.1 μm has the shape [90]

$$E(\lambda) = \frac{4\gamma_{abs}\gamma_{rad}}{(\omega - \omega_0)^2 + (\gamma_{rad} + \gamma_{abs})^2} \tag{6.2}$$

where ω_0 is the frequency of peak emissivity, γ_{abs} is the absorption rate, and γ_{rad} is the radiative coupling. The fit is shown with dashed lines in Figure 6.18c while the simulated data using $n = 2.3$ is shown for comparison with the solid line. We find the quality factor with $Q = \omega_0/2(\gamma_{abs} + \gamma_{rad})$. At near-normal incidence ($x = 14.5\mu$m), this peak is located at $\lambda_0 = 4.12\mu$m ($\nu_0 = 73$ THz) with an width of $2(\gamma_{abs} + \gamma_{rad}) = 688$ GHz. This corresponds to a Q of 106.

Improvements to the Q can be made by lowering γ_{rad} or γ_{abs}. Clearly, γ_{rad} and γ_{abs} are symmetric in Eqn. 6.2, so we need a way to distinguish the two. As the emission

moves off-normal, we would expect the radiative coupling to increase due to the increased symmetry breaking. As can be seen in Figure 6.18d, we observe this behavior in one of the fit parameters.

From this data, we can obtain an estimate of the emitted intensity. The emissivity peaks at about $E = 0.55$ at a wavelength λ_0 =4.1 μm or $\nu_0 = 73$ THz). A Q of 106 means the FWHM is 73 THz/106≈ 688 GHz. According to Ref. **??**, the intensity is given by

$$I = \int d\Omega \int d\nu \, (0.55) \frac{c}{4\pi} \frac{8\pi\nu^2}{c^3} \frac{h\nu}{e^{h\nu/kT} - 1} \approx (0.001) \left[(688 \times 10^9)(0.55) 4\pi \frac{8\pi\nu_0^2}{c^3} \frac{h\nu_0}{e^{h\nu_0/kT} - 1} \right] = 2.5\text{mW/m}^2. \tag{6.3}$$

Here, we take the solid angle integral to be is taken over the solid angle of the iris used a circle roughly 1° in radius giving $\Omega = ((1°)(2\pi/360°))^2\pi \approx 0.001$ str. The frequency integral an intregral of the peak. The frequency integral we estimate as a rectangle with its center at $\nu_0 = 73$ THz and width $FWHM = \nu_0/106 = 688$ GHz. At $T = 250°$ C, yielding the intensity of roughly $I = 2.5$ mW/m^2 and a power of $P = 2.5\text{mW/m}^2 \times (4\text{ mm})^2 = 40$ nW for our 4 mm pattern. Raising the temperature to 300° C would roughly double the intensity to $I = 4.8$ mW/m^2 while raising to 500° C would bring this to $I = 23.6$ mW/m^2 and a power 376 nW.

6.3.3 Tunable Dimerized Gratings

We now turn to the main result of this part of the thesis, the measurement of the TTD 1. The fabrication of this device is described in Section 6.2.3. Measurements were taken using the reflection and emission setups described in Section 6.3.1. The sample was placed on a sample carrier and wirebonded. The carrier was then hooked up to a Keithley 2410 for gating and a Keithley 2400 for source-drain measurements of the graphene.

The first measurement was a reflection measurement to assess whether the BIC mode is visible. Such a mode was visible in the NTTD (Section 6.3.2), but with the change in Silicon deposition procedure, it is prudent to check that this is still the case. Figure 6.19 shows the measurement of 1-R. Two peaks in the data at 5.4 μm and 6.1 μm indicate the possibility of

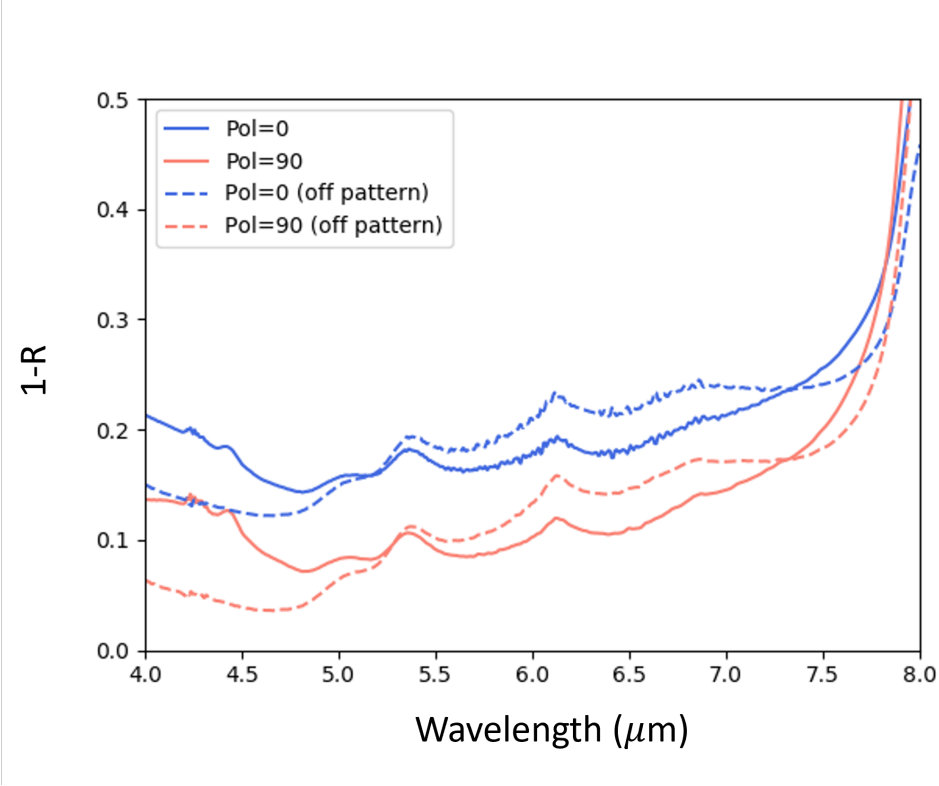

Figure 6.19: Reflection measurements of TTD 1.

BIC modes. However, these modes are not polarization dependent. In addition, they appear off of the pattern as well. There is no evidence that they are BIC modes.

The next measurement was an unpurged gated thermal emission measurement at a temperature $T = 150°\text{C}$. The graphene resistance as a function of gate voltage V_G is shown in Figure 6.20a. The variation in resistance shows that the capacitor is working as expected. Gated resistance is shown in Figure 6.20b. The resistance begins at 500 GΩ and reduces significantly as the experiment progresses. Total emission and emissivity are shown in 6.20c-d, respectively. There is no evidence of BIC modes, let alone changes in the emission spectrum with gate voltage.

With no evidence for BIC modes or gate-dependent spectra, the focus turned to analyzing the measurement setup. Perhaps the alignment was poor, or the temperature too low. Performing a spatially filtered emission measurement (Section 6.3.1) would show angular dependence of the structure. The spatial filtering measurement is shown in Figure 6.21a.

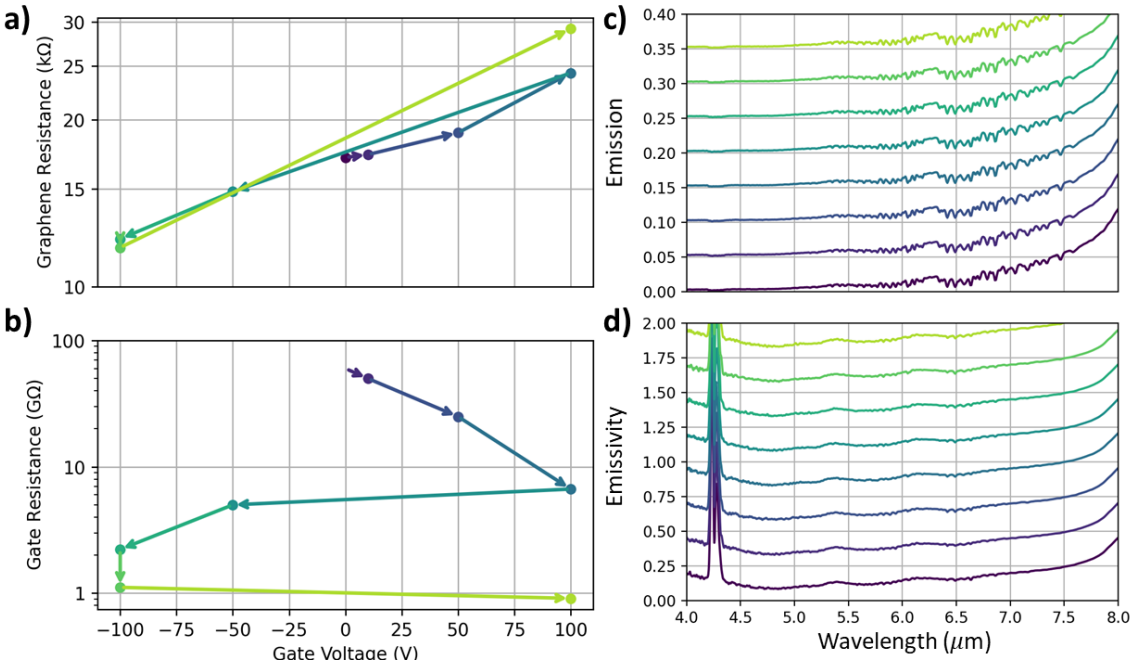

Figure 6.20: Gated emission measurements of TTD 1. a) Graphene resistance as a function of gate voltage V_G. Source-drain voltage of 100 mV was used. b) Gate resistance as a function of gate voltage V_G. First data point $V_G = 0$ is not included since resistance is undefined at that point. c) Total emission in arbitrary units as a function of gate voltage. Colors correspond to the different gate voltages as shown in a and b. d) Emissivities calculated by normalizing spectra in c to blackbody. CO_2 absorption is visible at 4.2 μm.

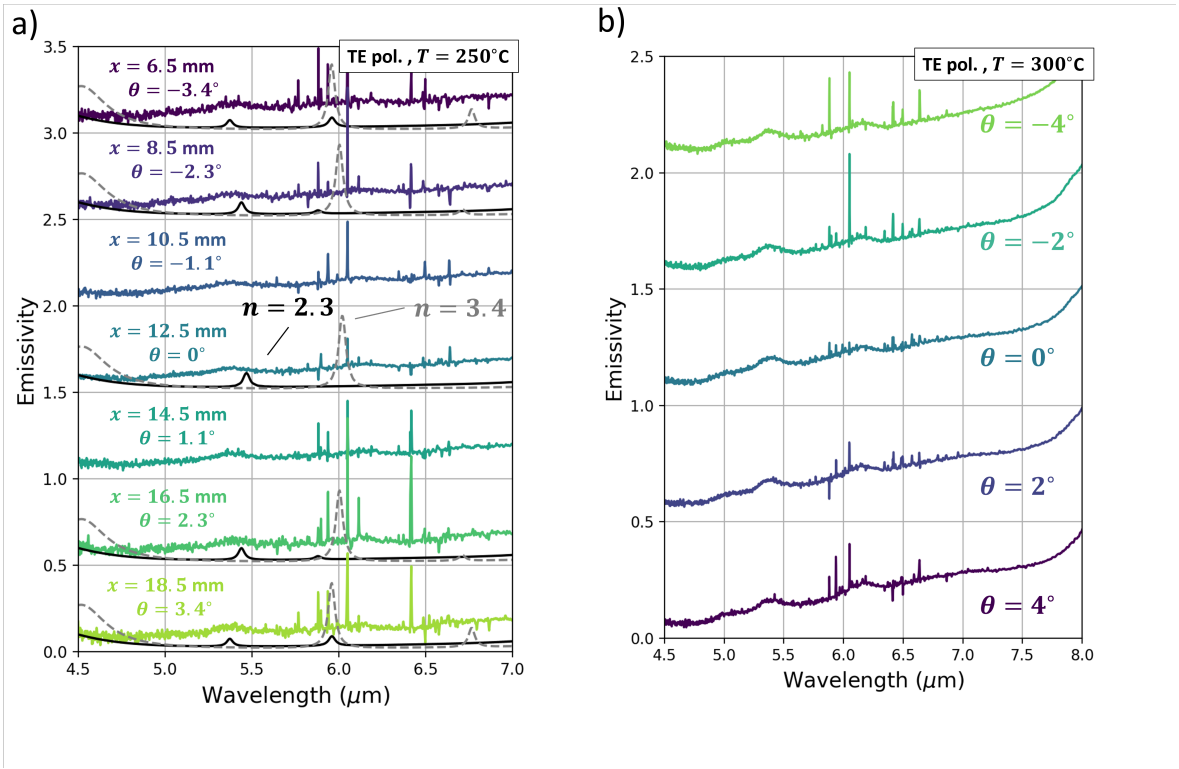

Figure 6.21: Emission measurements of TTD 1. a) Emission spectra in spatially filtered measurement. Simulated spectra shown in gray.

No evidence of changes to the spectra are apparent in this figure. In addition, perhaps the sample was pointed too far off the center. We tried rotating the sample stage to various degrees at a higher temperature ($T = 300°$ C). The results of this are shown in Figure 6.21b. As seen in Figure 6.21a, the simulated spectra show weak peaks when assuming $n = 2.3$. It seems that the base level of emission is too high to detect these peaks. In contrast, when $n = 3.4$, the peaks are shifted to nearly 6.0 μm and much stronger reaching emissivities of almost 0.5. Most likely, γ_{rad} is different from that in the initial design simply due to the change in index. Redesigning the structure such that $\gamma_{rad} \approx \gamma_{abs}$ ought to make the peak more visible.

Another sample (TTD 2) was fabricated with altered dimensions in order to account for the lower index. See Section 6.2.3 for information on the fabrication of this sample. The index of Si was assumed to be $n_{Si} = 2.6$ during the optimization, even though the NTTD suggested that the index could be as low as $n_{Si} = 2.3$. This was due to a miscommunication.

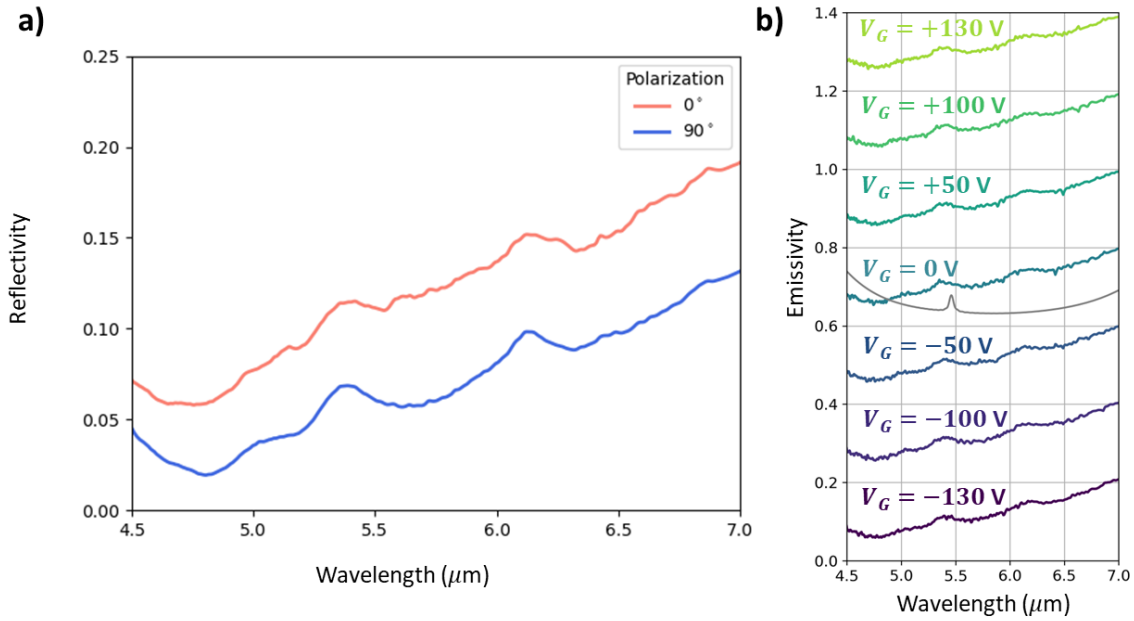

Figure 6.22: FTIR measurements of TTD 2. a) Reflectivity measurement of TTD 2. There is some evidence of polarization dependent modes at 5.6 μm and 6.2 μm. b) Gate-dependent emission measurements of TTD 2. Polarization is TE and temperature is 250° C. The single gray plot is the theoretical emission spectrum assuming $n_{si} = 2.3$.

Figure 6.22a and b show the result of the reflection and emissivity measurements of this device. In reflection mode, we observe a possible polarization dependence at 5.6 μm and 6.2 μm. Gate-dependent emissivity measurements were performed next. Measurements were performed in TE mode at 250°C. A mode is visible at 5.4 μm, but there is little evidence of gate-dependence. The graphene resistance was monitored during the measurement. At gate voltage magnitudes of roughly 130 V, the graphene resistance significantly increased stopping the measurement from proceeding further.

In Figure 6.22b, it appears the mode magnitude is below the background signal. A more careful measurement setup may be required. For example, it has been shown that there are conditions in which the background emission of the instrument hides signals below a certain threshold.[115] A characterization of the FTIR may reveal the mode hiding below the background.

6.4 Conclusions

In this section, we have described the progress toward the creation of a narrowband frequency-modulated thermal emitter. We showed that a metasurface based on BIC modes could theoretically be a viable path forward for the creation of this device. Evaporated silicon patterned into DHCGs was shown to support BIC modes. It was also shown that it is possible to fabricate a metasurface of patterned silicon on graphene. Further measurements of these device are required.

Chapter 7

Conclusions, Recommendations, & Future Work

7.1 Conclusions

We have demonstrated design, fabrication, and measurement of tunable narrowband MIR thermal emitter based on dimerized gratings. However, much work remains to improve this device.

7.2 Future Work

7.2.1 Fabrication Changes

The deposition of silcon on top of graphene is the most challenging part of making this device. Improvements could be made to the silicon deposition by using atomic layer deposition. As discussed in Section 6.2.3, the surface roughness appears to play a crucial role in silicon deposition on graphene. Smoothing out the substrate and using thinner Si may allow one to use the Transfer Si method for silicon deposition.

As we saw in Section 6.1.1, the wavelength of choice is primarily limited by the spacer material which inevitably introduces loss at longer wavelengths due to a phonon. This limits the operating wavelength to $< 5\mu$m for Si_3N_4, $< 7\mu$m for SiO_2, and about $< 9\mu$m for Al_2O_3 and TiO_2. For free space optical communication, it is critical to push the operating wavelength into the atmospheric transmission window at 8-14 μm. Potential replace-

ments for these spacer materials include ytterbium trifluoride (YbF_3) and lanthanum fluoride (LaF_3).Both materials have extremely low dispersion, low refractive indices ($n < 1.5$) and low loss ($k < 0.03$) up to 12 μm. [116] These materials are already used in UV optics to make lens coatings and can be readily evaporated. In order to incorporate these materials into a device, it would remain to measure the dielectric breakdown voltage.

7.2.2 Trace Gas Sensing

Once the thermal emitter has been fabricated, it would remain to demonstrate its applicability to trace gas sensing. As described in Section 4.1, trace gas sensing is a primary application of QCLs and ICLs which this device would look to replace. An absorption line of a gas at frequency f_a with HWHM $f_{1/2}$ is chosen and the device output frequency f_0 is designed to roughly match the absorption line such that $f_0 \approx f_a$. The output frequency (or wavelength) of the emitter source is then modulated at a frequency f_m. Wavelength modulation spectroscopy (WMS) and one- and two-tone frequency modulation spectroscopy (FMS) are the potential methods that would be used for this application.[57, 58]

In WMS, the frequency is modulated slowly such that $f_m \ll f_{1/2}$.[57] The instantaneous center frequency of the emitter is then

$$f(t) = f_0 + m\sin(2\pi f_m t) \tag{7.1}$$

where m if the *modulation index*. In contrast, FMS methods assume $f_m > f_{1/2}$. One-tone FMS often requires high detector bandwidth >150 MHz, while two-tone FMS is much lower at <10 MHz. At these frequencies, the phase of the electric field cannot be assumed to be constant, and an amplitude modulation occurs.[57]

Here, we provide an estimate of the modulation frequency for our device. Since the device is a parallel-plate capacitor, the modulation will be limited by the RC time-constant. The graphene resistance is on the order of R_G =10 kΩ and the back-gate resistance is reliably on the order of $R_B = 1$ GΩ. Since $R_G \ll R_B$, we may ignore R_B. The capacitance can be estimated as $C = \kappa\epsilon_0 A/d$ where $\kappa \approx 3.6$ is the dielectric constant of the SiO_2, $A \approx (4\text{mm})^2$ is

the graphene area, and $d \approx 2\mu$m is the spacer thickness. This yields a capacitance of roughly $C \approx 100$ pF. The time constant is then $\tau = 10\text{k}\Omega \times 100\text{pF} = 100$ ns. The maximum frequency of operation would then roughly be $f_m = 1/\tau = 10$ MHz. This matches well with previously reported modulation frequencies of graphene capacitor devices. [13] Even modulation speeds of up to 20 GHz have been theorized.[74]. This device ought to be capable of performing all types of WMS and FMS methods. It may even be possible to perform WMS by rotating the sample quickly, since this only uses modulation frequencies of 1 kHz. Therefore, the emitter ought to be more than capable of performing at the required modulation frequencies for this application.

The signal-to-noise ratio (SNR) is given by S/N, and determines the level of absorption that one can detect. In terms of the root-mean-squared quantiites, the SNR is given by [57]

$$S/N = \frac{\overline{\langle i_s(t) \rangle}}{\sqrt{\bar{i_s^2} + \bar{i_e^2} + \bar{i_A^2} + \bar{i_{ex}^2}}} \tag{7.2}$$

The numerator is the signal reaching the detector, and the denominator is a quadrature sum of the noise components: laser-induced detector shot noise, detector-preamplifier thermal noise (Johnson noise), residual amplitude modulation (RAM) noise, and laser excess noise, respectively. The time-averaged signal current of the detector is proportional to the power reaching the detector P by $\overline{\langle i_s(t) \rangle} = \frac{e\eta}{h\nu_0} P$.[117] Expressions for S are given in Ref. [57].

The mean-squared laser-excess noise current is given by

$$\bar{i_{ex}^2} = \left(\frac{e\eta}{h\nu_0}\right)^2 \frac{\Delta f}{f^b} \sigma_{ex}^2 \tag{7.3}$$

where Δf is the detection bandwidth, f is the detection frequency, $\sigma_e x$ is the laser excess noise at 1-Hz bandwidth and 1-Hz bandwidth and b is an exponent that is typically equal to 1. Also known as *flicker noise*, this is the $1/f$ noise that generally motivates the use of lock-in detectors. The term *low-frequency* usually refers to the regime where this noise dominates. Typically, the origin of this noise is difficult to determine, and it would be a useful project for someone to characterize this noise term for the tunable thermal emitter.

The detector shot noise comes from the Poissonian distribution of photons hitting the detector. A spectroscopic system dominated by this term is often called "quantum-limited".[118] The functional form is given by

$$\bar{i_s^2} = 2e\frac{e\eta}{h\nu_0}\langle P_0\rangle\left(1+\frac{M^2}{2}\right)^N \Delta f \tag{7.4}$$

where N is the number of tones used for modulation (1 or 2). This noise dominates at sufficiently high powers and is unlikely to limit our device.[58]

The Johnson noise of the preamplifier is independent of frequency. Assuming a load resistor $R_L = 50\Omega$ and room-temperature operation $T_eff = 295$ K to avoid needing to cool the detector, we estimate

$$\bar{i_e^2} = \frac{4kT_{eff}}{R_L}\Delta f \approx \left(3.25\times 10^{-22}\right)\Delta f. \tag{7.5}$$

Typically the detector bandwidth is 1 Hz$< \Delta f <$10 Hz, so we expect about 100-1000 pA^2 of noise.

During modulation, the amplitude of the emitter signal will inevitably vary slightly. The variation in intensity is proportional to[57]

$$I \propto (1+2M\sin(\omega_m t) \tag{7.6}$$

This leads to a noise floor known as RAM noise. The RAM noise is given by

$$= \left(\frac{e\eta}{h\nu_0}\right)^2 2R^2(M)\sigma_p^2 \tag{7.7}$$

where $R(M)$ is a function defined in Ref. [57] and σ_p is the standard deviation of the laser output power. Notice that this is independent of frequency and power, and is therefore a form of white noise. For an emitter that does not modulate in intensity whatsoever, $M = 0$ and this noise will be zero. In the future, it may be beneficial to design a tunable thermal emitter which exhibits no amplitude modulation.

For WMS and FMS techniques, powers of at least the μW range are required.[58] As calculated in Section 6.3.2, the intensity of the measured device was determined to be 2.5

mW/m^2 at 250° C, or 40 nW over the entire 16 mm^2 area. This assumed a 1° cone of emission and a bandwidth of 688 GHz. Since absorption HWHMs in the MIR tend to be in the 100 MHz range, a 3 order magnitude reduction in emitter bandwidth is required to reach this level.[57] BIC modes have demonstrated linewidths at this level ($Q \sim 18,000$ at 1.5 μm or a linewith of about 100 MHz) but still carry room for improvement.[100] However, a 3 order of magnitude reduction in bandwidth would reduce the power proportionally if the emitter is kept at the same temperature. Either the area or temperature would need to increase.

If one plans to make a low-SWaP spectrometer with this device, the most important regime to consider will be that of low power and low frequency. A narrowband emitter based on thermal emission is limited by the blackbody spectrum, and μW powers are the most optimistic regime of power, even for large patterned areas and high temperatures. In addition, a cheap spectroscopy system must use a cheap detector, which typically has a bandwidth in the range of <10 MHz. Fortunately, absorbance detection in the range of 10^{-7} has been measured with powers and modulation frequencies in this range.[58]

7.2.3 Free-Space Optical Communication

Free-space optical communication (FSOC) is another area which this device may replace. Bits are encoded into the amplitude or frequency of the emitter. Pulse amplitude modulation (PAM) keying, in which the amplitude is used for keying, has been shown to operate at Gb/s data transfer rates with QCLs in the lab.[66] A different type of encoding would be more appropriate for this emitter. A 1 could be the higher frequency, and a 0 the lower frequency. This is known as *frequency shift keying*. Due to the close spacing of the resonant frequencies, this emitter would be most appropriate for *continuous phase frequency shift keying*.[119] This is in contrast to binary frequency shift keying, which keeps a constant phase and requires the emitter frequency to be some multiple of the carrier frequency.

Part III

Dynamic band structure and capacitance effects in scanning tunneling spectroscopy of bilayer graphene

This part is reproduced from

Holdman GR, Krebs ZJ, Behn WA, Smith KJ, Watanabe K, Taniguchi T, et al. Dynamic band structure and capacitance effects in scanning tunneling spectroscopy of bilayer graphene. Appl Phys Lett. 2019 Oct 28;115(18):181601.

with the permission of AIP Publishing.

7.3 Abstract

We develop a fully self-consistent model to describe scanning tunneling spectroscopy (STS) measurements of Bernal-stacked bilayer graphene (BLG), and we compare the results of our model to experimental measurements. Our results show that the STS tip acts as a top gate that changes the BLG bandstructure and Fermi level, while simultaneously probing the voltage-dependent tunneling density of states (TDOS). These effects lead to differences between the TDOS and the local density of states (LDOS); in particular, we show that the bandgap of the BLG appears larger than expected in STS measurements, that an additional feature appears in the TDOS that is an artifact of the STS measurement, and that asymmetric charge distribution effects between the individual graphene layers are observable via STS.

Chapter 8

Main Text

Bilayer graphene (BLG) has been shown to display a rich electronic structure that is strongly dependent on both the electrostatic environment and the relative layer orientation. For example, transverse electric fields in Bernal-stacked BLG can induce a continuously tunable bandgap,[120] while introducing a relative twist angle between the individual graphene sheets has been shown to promote correlated electron behavior such as superconductivity and Mott-like insulation. [121–125] Furthermore, at certain temperatures and carrier densities, electrons in BLG exhibit hydrodynamic flow. [126–128] These effects are, however, often sensitive to local perturbations which can alter the nature of novel electronic states, and obfuscate them in spatially averaged measurements; a complete understanding of BLG behavior, therefore, requires the development of local probes that can correlate electronic structure with crystal orientation, atomic defects, and charged impurities.

Scanning tunneling spectroscopy (STS) provides a promising pathway for understanding the role of disorder in BLG at atomic length scales. STS measurements of BLG on SiO_2 and hexagonal boron nitride (hBN) have already been used to probe a range of properties including quasiparticle dispersion,[129] gate-induced gap formation, [129–131] localized bound or scattering states, [130, 132] and Landau level splittings that indicate correlated electron behavior. [130] The dynamic electronic structure of BLG, however, complicates the STS data. In particular, the BLG bandstructure is sensitive to electric fields applied perpendicular to the sample, which can both open a bandgap and change the carrier density. [120,

133–136] In STS measurements, the perpendicular fields change as the tip voltage is varied, leading to differences between the local density of states (LDOS) and the tunneling density of states (TDOS). Understanding how to reconcile those differences in STS measurements is important when extracting physical BLG parameters such as bandgap, carrier density, or signatures of correlated electron behavior.

In previous STS measurements, the effect of the changing electric field from the tip has been observed as instantaneous charging events where either a localized state [132] or Landau level [130] of the BLG was pushed across the Fermi level due to tip-induced doping. In those results, and in other reports, [131] the effect of tip induced changes in carrier density, and the effect of the back gate on the BLG band gap were considered. However, a full description requires a model that includes the tip's effect on the transverse field as well. In this study, we apply techniques from previously developed theoretical models of BLG in an electric field [137–139] to calculate how the electronic structure of the BLG changes with tip voltage, and how those changes affect the TDOS. We find that STS measurements of the BLG gap are expected to overestimate the width of the bandgap, and that an extra feature is introduced in the TDOS that is related to the BLG bandgap crossing the Fermi energy. These calculations also show how interlayer capacitance phenomena can be observed in STS measurements, and that – due to offsetting effects – the dependence of the charge neutral point on back gate voltage is not significantly altered by tip gating. We compare those calculations to experimental STS spectra taken from a BLG/hBN device at 4.5K and find good quantitative agreement.

A schematic of an STS measurement of BLG is shown in Fig. 8.1(a). We assume the radius of curvature of the STM tip (> 100 nm) is much larger than the tip-sample distance ($\lesssim 1$ nm), so that the tip can be modeled as a flat plate. [140] In this geometry, the tip acts as a top gate with voltage set to $-V_S$ (V_S is the sample bias) while a back gate voltage V_B is also applied to the doped silicon under the hBN/SiO_2 layer. These gates induce a potential V_1 (V_2) on the top (bottom) layer of the BLG which may be combined into a symmetric and antisymmetric combination, $V_\pm = (V_1 \pm V_2)/2$. Physically, V_+ represents

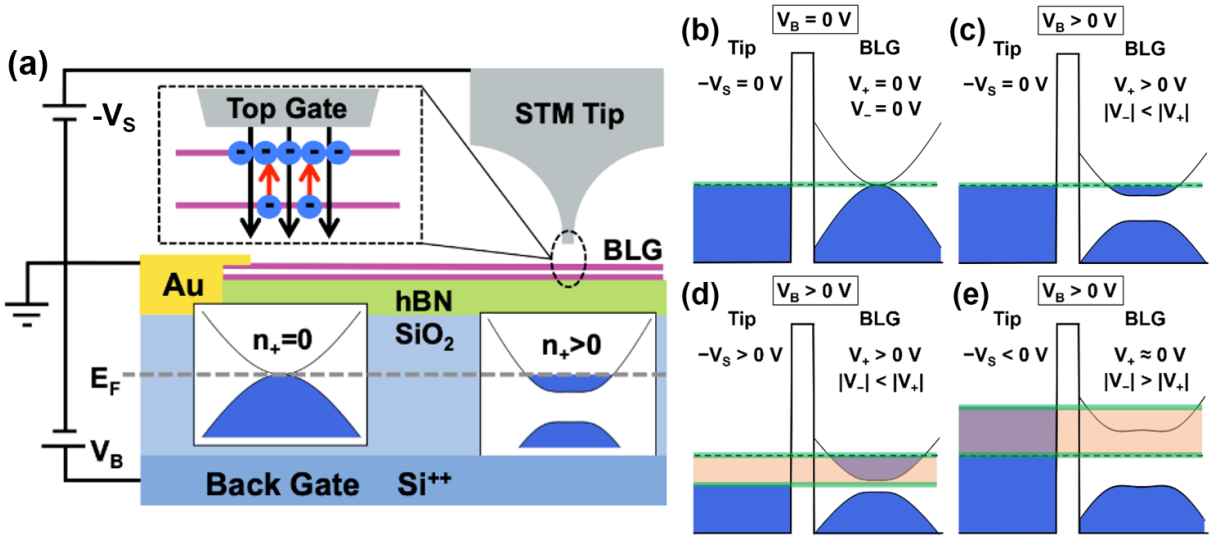

Figure 8.1: (a) Schematic of the STM setup with -$V_S \neq V_B = 0$ V. A nonzero tunneling bias applied to the STM tip both locally dopes the sample and opens a bandgap. (b)-(e) Tunneling scenarios in selected electrostatic environments. Solid blue indicates filled electron states, orange shading indicates tunneling states, while green indicates states that are measured in a dI/dV_S measurement at the given V_S.

the local electrostatic potential of the BLG patch under the STM tip, and V_- is half of the electrostatic potential difference between the layers. Since the sample is grounded, the electrochemical potential is zero, $\Phi = \epsilon_F - eV_+ = 0$, with ϵ_F denoting the local Fermi level. For $\epsilon_F \neq 0$, the sample may be doped to a carrier density $n_+ = n_1 + n_2$, where n_i is the carrier density on layer i. In general, $n_1 \neq n_2$, and we denote the carrier layer asymmetry by $n_- = n_1 - n_2$.

The bandstructure of BLG is dependent on the interlayer potential difference V_-, and a nonzero value of V_- opens up a bandgap with magnitude [138]

$$\Delta_g = \frac{2\gamma_1 e|V_-|}{\sqrt{\gamma_1^2 + 4e^2|V_-|^2}}, \tag{8.1}$$

where $\gamma_1 = 0.35$ eV is the interlayer hopping potential of BLG.[137, 141] The relationship between n_+ and the Fermi level is also dependent on the interlayer potential energy $u = -2eV_-$. For low temperatures ($k_BT \ll \epsilon_F$), it can be shown that [137]

$$\epsilon_F^2 = \frac{(\pi\hbar^2 v_F^2 n_+)^2 + \gamma_1^2 u^2}{4(\gamma_1^2 + u^2)}. \tag{8.2}$$

When the sample is undoped – that is, ϵ_F lies within the bandgap – the BLG is insulating

and the system can be described by two gate electrodes filled with dielectric media. If the BLG is doped, however, the accumulated charge will establish equilibrium with the applied voltages to create an inter-sheet polarization field that partially offsets the applied field. An application of Gauss' law gives the local potential of the sample just underneath the tip as

$$V_+ = \frac{d_1 d_2}{\epsilon_0 d_2 + \epsilon_2 d_1}\left(\frac{\epsilon_0}{d_1}(-V_S - V_-) + \frac{\epsilon_2}{d_2}(V_B + V_-) - e n_+\right), \tag{8.3}$$

and the bare, unscreened potential difference is given by

$$V_-^{ext} = \left(\frac{4\epsilon_0}{d} + \frac{\epsilon_0}{d_1} + \frac{\epsilon_2}{d_2}\right)^{-1}\left(\frac{\epsilon_0}{d_1}(-V_S - V_+) - \frac{\epsilon_2}{d_2}(V_B - V_+)\right). \tag{8.4}$$

where ϵ_2, d_2 are the dielectric constant and thickness of the substrate, d_1 is the tip height above the top BLG sheet, and d is the intersheet spacing of the BLG.

In our model we self-consistently solve the equation $V_- = V_-^{ext}(V_+) + \frac{d_{eff}}{\epsilon_{eff}} e n_-(V_+, V_-)$ for every pair of $V_{(S,B)}$, where V_-^{ext} is the unscreened interlayer potential difference, and $\frac{d_{eff}}{\epsilon_{eff}}$ is the prefactor of Eq. 8.4. This gives the carrier density and bandstructure of the BLG as a function of V_S, allowing us to compute the tunneling spectra dI/dV_S (see Supplementary Online Materials). The free parameters used in our self-consistent model are the tip height d_1, the tip-sample work function difference ΔW_{t-s}, and the back gate voltage offset due to substrate-induced doping $V_{B,0}$. We note that while it is justified to model the tip as a parallel plate in the electrostatic equations, d_1 is not necessarily equal to the true tunneling distance, since sharp protrusions may have a negligible contribution to the tip capacitance.

Figures 8.1(b-e) illustrate how the bandstructure of intrinsic BLG changes with varying $V_{(S,B)}$, and how those changes result in several key features in the TDOS. When the applied voltages are zero (Fig. 8.1(b)), the BLG is charge neutral and the Fermi levels of the tip and sample align. For the case when $V_B > 0$ (Fig. 8.1(c)), the BLG becomes n-doped and a bandgap opens due to a transverse electric field from the back gate. If a positive tip bias is also applied ($-V_S > 0$) while keeping the same $V_B > 0$ (Fig. 8.1(d)), an opposing electric field from the tip further dopes the BLG, and also partially closes the bandgap by reducing the transverse electric field. Changes in the tip voltage lead to changes in the states available

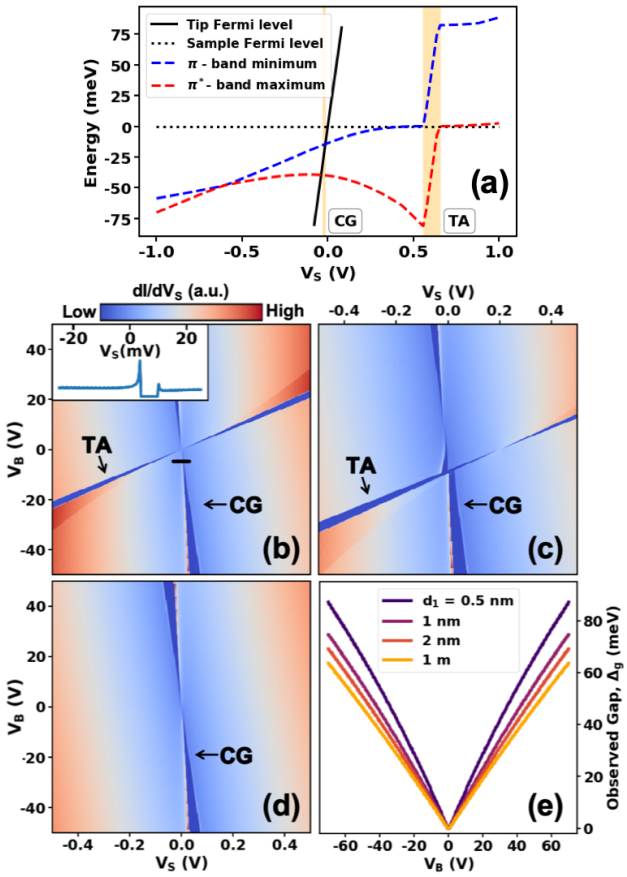

Figure 8.2: (a) Energies of BLG bandstructure features as a function of sample bias V_S for $V_B = 20$ V, $d_1 = 2$ nm, $d_2 = 285$ nm, and $\Delta W_{t-s} = 0$. CG and TA occur within the indicated regions when the tip and sample Fermi levels, respectively, are aligned with the BLG bandgap. (b)-(d) Theoretical dI/dV_S for the following model parameters: (b) $d_1 = 2$ nm, $d_2 = 285$ nm, $\Delta W_{t-s} = 0$, $V_{B,0} = 0$. Inset is a linecut along the black line at $V_B = -5$ V; (c) $d_1 = 2$ nm, $d_2 = 285$ nm, $\Delta W_{t-s} = -0.2$ eV, $V_{B,0} = 0$; (d) $d_1 = 1$ m, $d_2 = 285$ nm, $\Delta W_{t-s} = 0$ eV, $V_{B,0} = 0$. (e) Width of the CG as a function of back gate voltage V_B for different d_1.

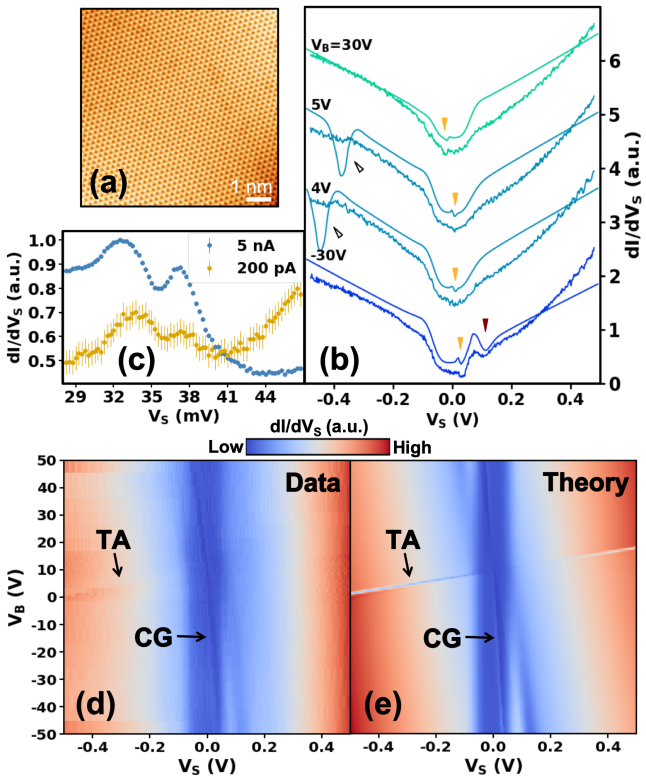

Figure 8.3: (a) STM constant-current topographic image of BLG ($I = 100$ pA, $V_S = -500$ mV). (b) Experimental (lower) and theoretical (upper) dI/dV_S tunneling spectra at four back gate voltages: -30, +4, +5, and +30 V. Curves are offset for clarity. Yellow (red) arrows indicate mid-gap point E_D in the elastic (inelastic) signal. Hollow arrows point to TA. (c) dI/dV_S measurements of the elastic CG as seen within the phonon gap at high (5 nA) and low (200 pA) tunneling current setpoints. ($V_B = 31$ V and V_S setpoint is -150 mV; data taken from a different set of measurements) (d) Experimental dI/dV_S gate map taken at a fixed location on the BLG flake (setpoint is $I = 3$ nA, $V_S = 700$ mV). Back gate resolution within the range V_B = 0-20 V is 1 V, otherwise it is 5 V. (e) Simulated dI/dV_S gate map fit to parameters that match data (see text).

for tunneling, yielding a nonzero dI/dV_S signal. We identify contributions from both the tip and sample Fermi levels – with the latter being caused by tip-induced band bending. If the tip Fermi level aligns with the BLG bandgap, no additional states are available at the lowest energies, which creates a minimum in the TDOS which we call the conventional gap (CG) feature. Meanwhile, a negative tip bias ($-V_S < 0$, Fig. 8.1(e)) will both widen the bandgap and decrease the carrier density of the BLG. In certain cases, the sample Fermi level can be pushed into the bandgap, again reducing the number of tunneling states and creating another minimum in the TDOS which we call the tunneling anomaly (TA).

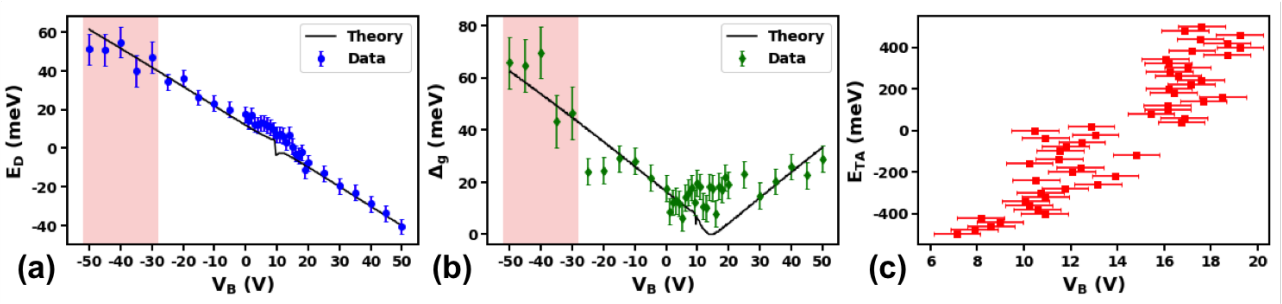

Figure 8.4: (a) The mig-gap points E_D from Fig. 8.3(d,e). Experimental values in the white (red) region are the minima in the elastic (inelastic) part of the spectrum. Inelastic values have had the 63 meV phonon energy subtracted. (b) CG width extracted from a fit to elastic (inelastic) tunneling spectra given in white (red) region. (c) Position of the TA, found by applying a piecewise fit function along V_B axis.

For a fixed back gate voltage of $V_B = 20$ V, this behavior is shown quantitatively in Fig. 8.2(a), where we plot the band minima/maxima as a function of sample bias. The CG is observed when the tip Fermi level aligns with the bandgap of BLG, while the TA is attributed to the sample Fermi level moving through the bandgap due to tip gating. We note that the underlying cause of the TA is similar to the mechanism of negative differential resistance (NDR) in other spectroscopic studies of atoms and molecules on insulating or semiconducting surfaces, as well as 2D materials. [142–152] In those studies, the tip-induced band bending pushes the Fermi level through a molecular resonance, leading to charge-induced changes in the conductivity, while in this work the band bending pushes the BLG into an insulating state underneath the STM tip.

The gate-dependent dI/dV_S spectra calculated using our full self-consistent model are shown in Fig. 8.2(b-d) for different choices of tip height and work function, and geometrical parameters consistent with a typical hBN/SiO_2 substrate. These results show that when fully accounting for the capacitive effects of the tip, the spectra exhibit several key features. First, the TA appears in the spectrum as a local minimum that disperses with V_B having slope opposite to the CG. The TA is visible for small tip-sample distances (Fig. 8.2(b,c)), but disappears when the tip is far from the sample (Fig. 8.2(d)), demonstrating that this feature is due to the electrostatic influence of the tip. Second, the CG appears as a narrow dip that occurs between two sharp peaks that are due to the van Hove singularities (vHs) at

the conduction and valence band edges of the BLG (inset Fig. 8.2(b)). Our calculation shows asymmetry in the vHs peaks due to the broken layer symmetry in the presence of an electric field as well as preferential tunneling into the top layer of the BLG.[138] These predictions are consistent with previous STS measurements of Bernal stacked BLG, [130] as well as recent measurements performed on twisted bilayer samples. [124, 125, 153, 154] Third, as shown in Fig. 8.2(e), the apparent energy width of the CG is tip height dependent, such that for $V_B = 50$ V, it appears as a 65, 55, and 51 meV gap for tip heights of 0.5, 1, and 2 nm, respectively. Fourth, there is an asymmetric increase in the dI/dV_S signal on either side of the TA due to vHs on the band edge. As described above, this effect is stronger on one side due to the asymmetric occupation of charge on the layers, a phenomenon related to near-layer capacitance enhancement (NLCE), which has previously been observed in transport measurements. [133, 139]

To compare our predictions to experimental measurements, we took STS measurements on exfoliated BLG samples at 4.5K and at $< 10^{-11}$ mbar. Six separate experiments were performed on four BLG/hBN samples and two BLG/SiO_2 samples, all of which showed results consistent with the data shown here, with some variation attributed to microscopic changes in the STM tip and charge puddles in the SiO_2 (see Supplementary Online Materials). The thickness of the hBN layers in all devices were optically estimated to be around 100 nm (on 285 nm SiO_2) through comparison with samples measured by atomic force microscopy. Measurements were carried out with chemically etched STM tips made of Pt/Ir alloy. The differential conductance signal was obtained using a lock-in amplifier with a modulation amplitude of 0.25-7 mV and frequency of 200-700 Hz. Before taking data on the BLG, the spectroscopic integrity of the STM tip was verified by acquiring dI/dV_S spectra on an Au(111) surface. [155]

Figure 8.3(a) shows a topographic image of the BLG surface. Point spectroscopy measurements using the same STM tip are given in Fig. 8.3(b) for a few gate voltages, alongside simulated spectra calculated with our self-consistent model for $d_1 = 5.5$ nm, $W_t = 4.45$ eV, and $V_{B,0} = -12$ V. The calculated spectra also include the effects of the known inelastic

tunneling channel due to a phonon mode with energy $E_{\rm ph} = 63$ meV (see Supplementary Online Materials).[156] For gate voltages $-50 \leq \mathrm{V}_B \leq 50$ V, the experimentally measured and calculated dI/dV_S spectra are shown side-by-side in Fig. 8.3(d,e). These results show strong quantitative agreement. We observe a narrow CG within the elastic signal (the central dark blue region where $|V_S| < E_{\rm ph}$) and a broadened inelastic CG signal that is shifted in energy by the phonon. Furthermore, we identify the TA as a narrow feature that has a strong dependence on the applied gate voltage and the NLCE asymmetry predicted in the model. A highly resolved spectroscopic measurement of the elastic CG is shown in Fig. 8.3(c) for two different tunneling setpoints of 5 nA and 200 pA, representing a tip height change of 1.5 Å. These data show two peaks of differing heights which we attribute to the vHs on the band edges. We measure a decrease in the peak spacing of 1 ± 1 meV as the tip retracts, which is consistent with Fig. 2(e), where we show that increases in tip height should decrease the bandgap. For a change in tip height of only 1.5 Å, the change in observed bandgap is expected to be small for large (¿2 nm) electrostatic distances, and is thus at the edge of our detection limit.

Unlike the CG, the energetic position of the TA is not shifted by inelastic tunneling, which is consistent with the predicted spectra. Within our model and fitting procedure, the CG and TA slopes are able to be simultaneously matched with the data, however, the theory predicts a more pronounced, gap-like TA. This discrepancy may be experimental in nature, due to thermal broadening in our 4.5 K STM, and broadening due to the lock-in modulation voltage. Another possibility is the breakdown of Eq. 8.2 near the TA, where the sample approaches charge-neutrality and one can no longer safely assume $k_B T \ll \epsilon_F$. Measurements of the TA obtained with smaller modulation voltages and different tip heights are shown in Fig. S6 in the Supplementary Online Materials.

We plot in Fig. 8.4 the CG and TA positions as a function of applied gate voltage, as well as the CG width. The CG position (E_D) and width (Δ_g) were obtained by fitting points around the minimum in each spectrum to a piece-wise fit (see Supplementary Online Materials). The TA, meanwhile, appears as a discontinuity in our sample bias-dependent line

cuts, and its position (E_{TA}) was determined based on the location of this discontinuity. These experimentally extracted parameters are compared to theoretical values from the results of Fig. 8.3(e). Interestingly, the experimentally measured CG width Δ_g never drops to zero, hovering around 10-25 meV. This result is in disagreement with our model – which predicts the CG gap to close regardless of the fitting parameters – but is consistent with previous STS measurements of BLG.[129, 130] This discrepancy offers evidence for the appearance of gapped broken symmetry states when the applied electric field approaches zero, which are predicted to have an energy gap ranging from a few meV up to 30 meV. [157–159] However, it is also possible that this gap is caused by substrate interactions. In particular, the underlying hBN may apply a periodic potential to the BLG, which can create a persistent bandgap. [160–162] Finally, we note that our model uses a flat-plate capacitor model for the STM tip, while in reality it has some finite curvature which can create a localized potential well that confines the quasiparticles in the BLG such that a quantum dot is formed underneath the tip. [132, 163] This quantization effect can also create persistent energy gaps in the STS spectrum.

In conclusion, we have demonstrated that a fully self-consistent electrostatic model for STS measurements of BLG is required to replicate many features of the dI/dV_S spectrum. In particular, we show that the STM tip can act as a top gate which simultaneously modifies the carrier density and bandstructure of BLG. These effects are observable as a tunneling anomaly in the spectrum that has a gate-dependent slope that is opposite to that of the conventional band gap in BLG, and an overestimation of the BLG bandgap in TDOS measurements. Furthermore, the spectrum contains features related to the unique capacitative behavior of BLG, which can be understood through our electrostatic model. More generally, this work demonstrates the importance of considering tip-gating effects in STS experiments of 2D materials that are known to have electronic properties that depend on an applied perpendicular electric field, including twisted bilayer graphene [164, 165] and some transition metal dichalcogenides. [166–168] These results show that electrostatic models that include the effect of the varying tip voltage are necessary to relate the dI/dV_S spectrum to the

electronic structure of such materials.

See Supplementary Online Resources for additional information about our model and experiment.

This research was performed using the compute resources and assistance of the UW-Madison Center For High Throughput Computing (CHTC) in the Department of Computer Sciences. The authors gratefully acknowledge use of facilities and instrumentation supported by NSF through the University of Wisconsin Materials Research Science and Engineering Center (DMR-1720415). K.W. and T.T. acknowledge support from the Elemental Strategy Initiative conducted by the MEXT, Japan, A3 Foresight by JSPS and the CREST (JP-MJCR15F3), JST.

Chapter 9

Supporting Information

9.1 Electrostatic equations

When the BLG is insulating ($|V_+| < |V_-|$), the entire space between the top and back electrodes can be viewed as three dielectric slabs in series. We can then solve for electric potential V_+ at the midpoint between the BLG layers, and half the layer potential difference, V_-. The expressions are

$$V_+ = \frac{(\epsilon_0^2 d_2 + \epsilon_0\epsilon_2 d/2)(-V_S) + (\epsilon_0\epsilon_2 d_1 + \epsilon_0\epsilon_2 d/2)V_B}{\epsilon_0^2 d_2 + \epsilon_0\epsilon_2 d_1 + \epsilon_0\epsilon_2 d}, \tag{S1}$$

$$V_- = \frac{1}{2}\frac{\epsilon_0\epsilon_2 d}{\epsilon_0^2 d_2 + \epsilon_0\epsilon_2 d_1 + \epsilon_0\epsilon_2 d}(-V_S - V_B), \tag{S2}$$

where d is the interlayer BLG spacing and d_1 (d_2) is the distance between the top (bottom) BLG layer and the top (bottom) electrode, ϵ_2 is the dielectric constant of the substrate, and ϵ_0 is the vacuum permittivity. When the BLG is in a metallic/conducting state, we should view the the two BLG layers as parallel conducting plates. An application of Gauss' law shows that the local potential of the sample just underneath the tip is given by:

$$V_+ = \frac{d_1 d_2}{\epsilon_0 d_2 + \epsilon_2 d_1}\left(\frac{\epsilon_0}{d_1}(-V_S - V_-) + \frac{\epsilon_2}{d_2}(V_B + V_-) - en_+\right). \tag{S3}$$

Now, if we neglect the charge asymmetry of the two BLG layers, we obtain for the bare, unscreened potential difference

$$V_-^{ext} = \left(\frac{4\epsilon_0}{d} + \frac{\epsilon_0}{d_1} + \frac{\epsilon_2}{d_2}\right)^{-1}\left(\frac{\epsilon_0}{d_1}(-V_S - V_+) - \frac{\epsilon_2}{d_2}(V_B - V_+)\right). \tag{S4}$$

To calculate the polarization field generated within the BLG, we use probability difference $\Delta P(k) = |\psi_t(k)|^2 - |\psi_b(k)|^2$ of finding an electron of wavenumber k on the top or bottom layer,[139]

$$\Delta P(k) = |\psi_t|^2 - |\psi_b|^2 = \frac{2eV_-}{\sqrt{(p^2/m)^2 + 4e^2V_-^2}}. \tag{S5}$$

Starting with the unscreened value V_-^{ext} we determine the screened value V_- by numerically solving the self-consistency equation [137]

$$V_- = V_-^{ext}(V_+) + \left(\frac{4\epsilon_0}{d} + \frac{\epsilon_0}{d_1} + \frac{\epsilon_2}{d_2}\right)^{-1} en_-(V_+, V_-), \tag{S6}$$

where the carrier density difference between layers n_- is computed via an integral of $\Delta P(k)$ over occupied states in the Brillouin zone. Note, ΔP does not directly depend on V_+, but n_- does via changes in occupation of states, i.e. changes to the limits of the integral. The primary effect of charge screening is to partially close the bandgap of BLG. Once V_+ and V_- are known, we use standard formulae to compute the tunneling current I as a function of V_S and V_B, [140] and calculate the TDOS by taking the derivative with respect to V_S.

9.2 Gate offsets and tunneling current formulae

The tip-sample work function difference $\Delta W_{t-s} = W_t - W_s$ causes measurable effects. We use a BLG work function of $W_s = 4.6$ eV[156] and fit to the tip work function W_t. In addition, a back gate voltage offset $V_{B,0}$ is present due to charge impurities in the substrate. Both of these parameters can be incorporated into the electrostatic equations by making the substitutions $-V_S \to -V_S - \Delta W_{t-s}/e$ and $V_B \to V_B + V_{B,0}$.

After computing the equilibrium values of $V_\pm$ with the modified electrostatic equations, we have enough information to compute the tunneling current. This is because V_- determines the DOS of BLG, $\rho_s(\epsilon_F + \epsilon, u)$, through the interlayer potential difference $u = -2eV_-$, and V_+ determines the Fermi level. In order to compare our theoretical TDOS directly to experimental spectra, it is necessary to include inelastic tunneling effects. Inelastic tunneling is primarily due to a phonon in graphene having energy $E_{ph} \approx 63$ meV and a width of 17 meV. [156, 169, 170] These effects can be included by adding an extra tunneling channel

to the TDOS that replicates the elastic channel, but is approximately 8 times stronger, broadened by the phonon width, and offset away from $V_S = 0$ by E_{ph}. Thus, at sample biases $|V_S| < E_{ph}$, the elastic channel dominates, while for sample biases $|V_S| > E_{ph}$, the tunneling signal is largely inelastic.

At zero temperature, for a tip with a constant DOS, the expression for elastic tunneling current takes the form

$$I_{el}(V_S) \propto \int_0^{eV_S} \rho_S(\epsilon_F + \epsilon, u) \exp\left(\frac{k_{el}(\epsilon - \frac{1}{2}eV_S)s}{\overline{\phi}}\right) d\epsilon, \tag{S7}$$

and for the inelastic tunneling current,

$$I_{in}(V_S) \propto \begin{cases} \int_0^{eV_S+\hbar\omega} \rho_S(\epsilon_F + \epsilon, u) \exp\left(\frac{k_{in}(\epsilon - \frac{1}{2}eV_S)s}{\overline{\phi}}\right) d\epsilon, & V_S > -\hbar\omega \\ \int_0^{eV_S-\hbar\omega} \rho_S(\epsilon_F + \epsilon, u) \exp\left(\frac{k_{in}(\epsilon - \frac{1}{2}eV_S)s}{\overline{\phi}}\right) d\epsilon, & V_S < \hbar\omega \\ 0, & \text{otherwise} \end{cases}. \tag{S8}$$

where $-V_S$ is the tip bias, $\hbar\omega$ is the phonon energy, k_{el}, k_{in} are the inverse decay length of electrons into the vacuum, and $\overline{\phi}$ is the average work function of the tip and sample.

Because the STM tip is closer to the top layer of the BLG flake, tunneling preferentially involves states weighted to the top layer. The precise ratio of tunneling currents due to the top and bottom layers depends on the decay length of electronic wavefunctions into the vacuum, but we do not attempt to calculate this here. Instead, we capture qualitatively this preferential tunneling effect by only including top layer tunneling current in the presented TDOS calculations. Mathematically, for each pair (V_S, V_B) and corresponding equilibrium (V_+, V_-), we multiply the tunneling current found via the previous formulae by an asymmetry factor

$$A(V_S, V_+, V_-) = \frac{n_1(V_+ + V_S, V_-) - n_1(V_+, V_-)}{n_+(V_+ + V_S, V_-) - n_+(V_+, V_-)}, \tag{S9}$$

which captures the fraction of tunneling states that are weighted to the top BLG layer. Here, n_1 is the (signed) number density of charge carriers on the top layer, and n_+ is the total number density on both layers.

9.3 Sample Fabrication

Heterostructures were prepared by viscoelastically transferring exfoliated BLG flakes onto exfoliated hBN crystals. [171] The thickness of the hBN layer was optically estimated to be 95 nm through comparison with samples measured by atomic force microscopy. The BLG/hBN stack was subsequently placed onto a SiO_2/Si substrate by evaporating the polymer in high vacuum at 300 °C. Electrical contact to the BLG was established using electron beam lithography followed by evaporation of Cr/Au leads. The sample was then mounted on a STM sample plate making use of sapphire spacers to keep the Si back gate electrically isolated. The Au leads and Si back gate were wedge bonded with Al wire to individual contact pads on the sample plate which connect to external BNC cables. A Keithley 2400 source supplied the back gate voltage. All BLG samples were annealed at 300 °C in UHV for about 12 hours to ensure a clean surface before measurement.

9.4 Effect of tip gating on charge neutrality

While our electrostatic model predicts that an STS experiment significantly overestimates the BLG bandgap for large tip-sample capacitances, the effect on the charge neutrality energy is less pronounced. The dispersion of charge neutrality E_D with back gate voltage is shown in Fig. 9.1 for a few different tip heights. For example, with back gate $V_B = -50$ V, at $d_1 = 1$ m we find $E_D = -51$ meV, whereas for $d_1 = 0.5$ and 1 nm, we have $E_D = -48$ and -49 meV, respectively. For large back gate voltages and small tip heights, the energy of charge neutrality can be underestimated by at least a few meV.

9.5 Extracting CG and TA

In the elastic signal, the charge neutrality energy E_D at a given back gate voltage was first estimated by finding the minimum in each sample bias dI/dV_S linecut. Then, a neighborhood of 15 points around this minimum was fitted to a piecewise linear-parabolic-linear function minimizing the chi-squared value. The energy E_D was recorded as the center of the parabolic

piece, whereas the the gap width Δ_g was determined by the difference between the optimal linear-parabolic transition points. See Fig. 9.2(a) for an example fit.

In the inelastic signal, the previous fit is rendered ineffective due to strong phonon broadening. A double-Gaussian plus linear background fit was used instead, where the difference between Gaussian peaks was interpreted as Δ_g, and the midpoint between them E_D. Figure 9.2(b) shows one such fit.

The TA energy E_{TA} was most easily picked out in the gate voltage dI/dV_S linecuts as a step-like feature. We fit a linear-linear piecewise function to a 10 V gate interval around where the TA was perceived to occur by-eye, and the optimal linear-linear transition point was deemed E_{TA}. Figure 9.2(c) shows an example fit.

9.6 STS of BLG/SiO_2

We also report STS measurements of a BLG/SiO_2 device. We highlight a number of similarities between Fig. 3 in the main text and Fig. 9.3. First, the 126 meV wide vertical blue region indicates that phonon-enhanced tunneling is still present for this system. A gap with negative slope can be seen as well, with a gap width that grows with more positive back gate voltages. The gap width here is consistently wider than in the hBN case. Between $V_B = -5$ and 5 V, there is a very shallow linear feature with positive slope, resembling the TA. We observe that the gate-dependent spectra for BLG/SiO_2 has more structure than for BLG/hBN/SiO_2.

9.7 Tip Anomaly Observation

For the majority of our gate sweeps, the tip anomaly appeared as a faint linear discontinuity with slope opposite that of the conventional gap. The data shown in Fig. 9.4 is an example of this not presented in the main text. In Fig. 9.5, we zoom-in to the same gate range in our data (Fig. 3 of the main article), and take a derivative with respect to the gate voltage in order to highlight the discontinuous nature of the TA. The purple diagonal feature represents

a single "step", and is characteristic of near-layer capacitance effects. We do not observe a true peak in the dI/dV_S signal, which would be indicative of quantum dot states induced by the STM tip rather than near-layer capacitance.

9.8 STS Measurements of Bilayer Graphene Near the Quantum Dot Regime and tip-height dependent measurements of the TA

While this work has focused on tip-induced changes in BLG electronic structure within a flat-plate capacitor model, previous work has shown that the spherical shape of the STM tip can induce localized potential wells in BLG/hBN systems due to the ionization of defects in the hBN.[132] These potential wells can cause quantization of the BLG bandstructure, leading to the formation of quantum dots beneath the STM tip, which cause sharp spectroscopic resonances in the STS spectrum due to charging of the quantum dot. Furthermore, previous STS measurement of surface 2DEGs have shown that the spherical shape of the STM tip can induce a localized quantum dot in the 2DEG that follows the position of the tip, and changes its energetic structure as the tip voltage is varied.[163] We found that measurements performed with some STM tips showed behavior similar to what was described in those works, and we attribute those results to the small spherical radius of the STM tip used in those measurements, for which the flat-plate model is not representative. Nevertheless, the basic qualitative behavior predicted in this work could also be observed in the small-tip curvature regime. As an example, Fig. S6 shows spectroscopic data taken from an BLG/hBN sample with a different STM tip from the tip used in the manuscript. These data also show the CG and TA spectroscopic features, but for a narrow range of V_G values near $V_G \sim 32$ V sharp resonances appear that are strongly gate-dependent, and show behavior similar to what was observed in Velasco et. al. An analysis of the TA and CG features in these data show a strong agreement with our theoretical model. In particular Fig. S6 (b) and (c) show a clear gap-like TA feature that shows a dependence on V_G that changes by nearly an order of magnitude as the tunneling setpoint is changed from 2 nA to 600 pA — representing an

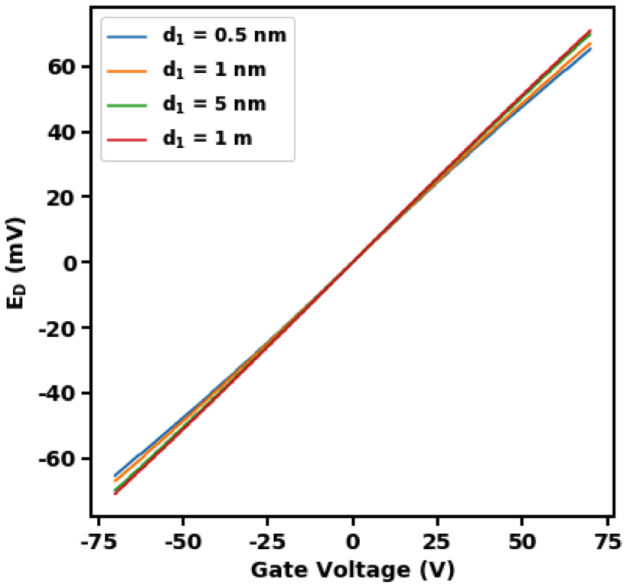

Figure 9.1: Energy of charge neutrality (i.e. location of the middle of the CG) as a function of back gate voltage for a range of tip-sample distances.

$\sim$0.5 Å change in tip height.

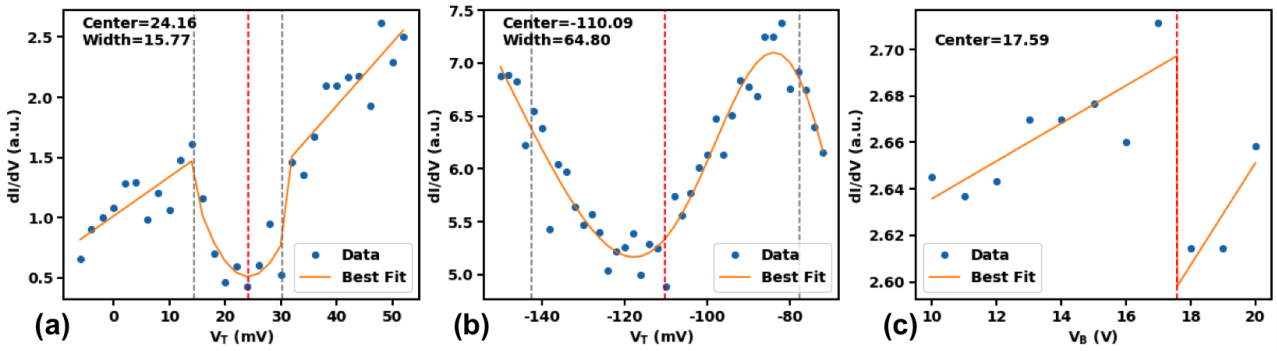

Figure 9.2: The three fits used to quantify the experimental conventional gap and tip anomaly: (a) linear-parabolic-linear fit for the CG in the elastic signal. (b) Double-Gaussian plus linear background fit for the CG in the elastic signal. (c) Linear-linear fit for the TA.

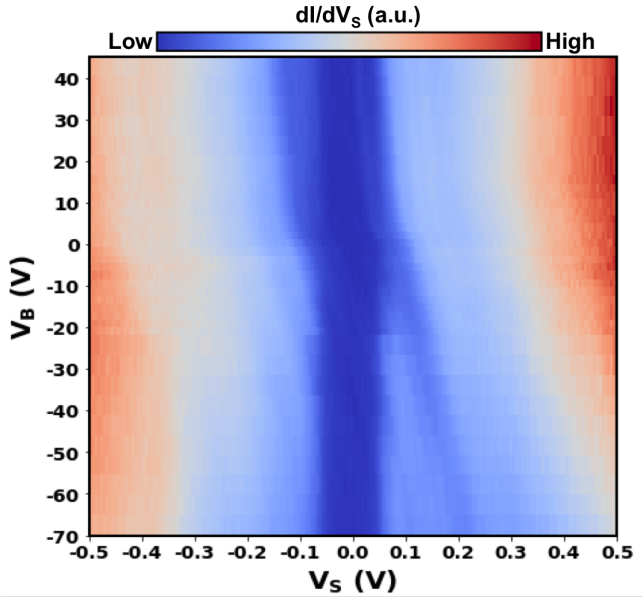

Figure 9.3: Experimental gate-dependent tunneling spectra of a BLG/SiO_2 sample.

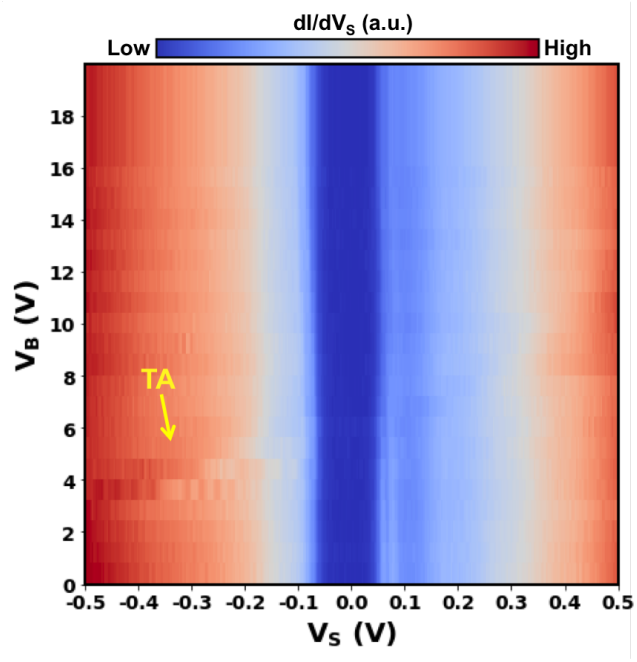

Figure 9.4: Experimental gate-dependent tunneling spectra of a BLG/hBN/SiO_2 sample exhibiting the TA.

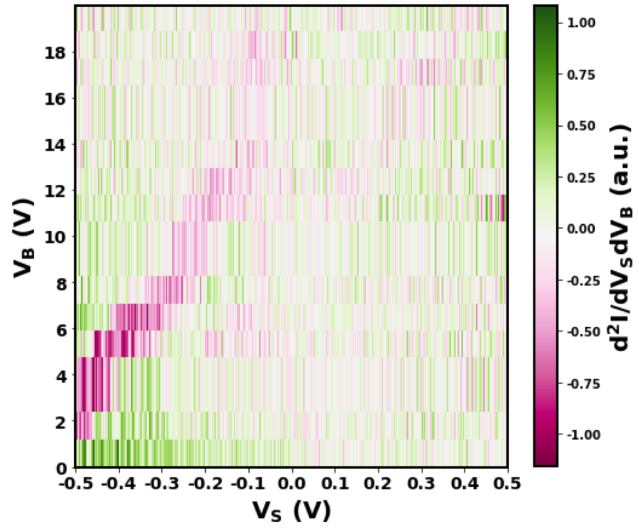

Figure 9.5: Derivative with respect to V_B of the TDOS near the TA in Fig. 3(d) of the main text. The large negative slope indicates that the TA is a discontinuous step down, rather than a peak (a peak would also have a large positive slope).

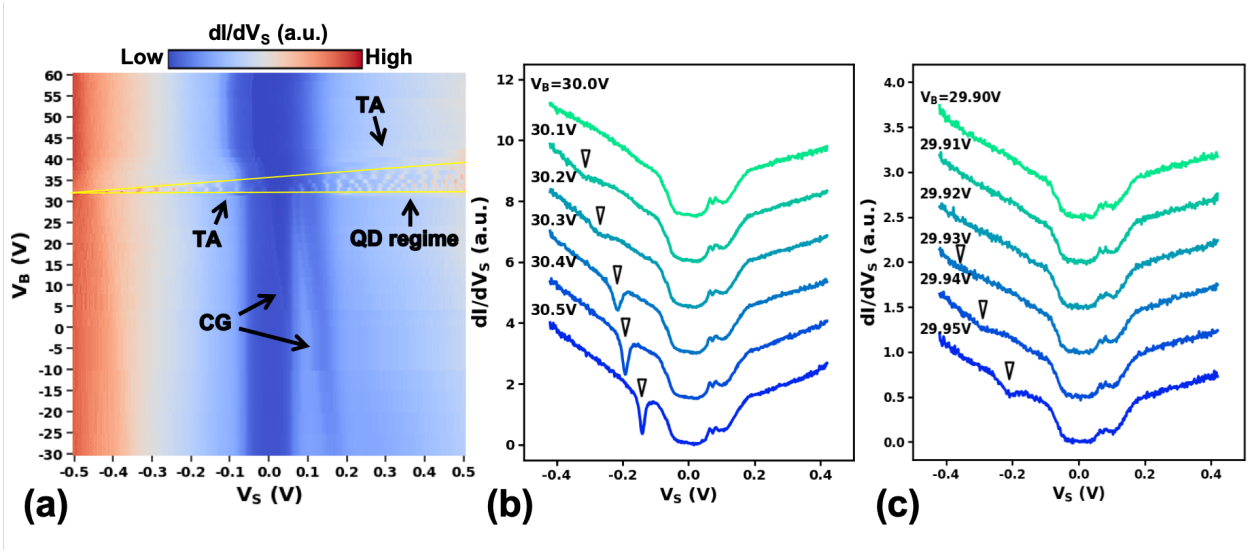

Figure 9.6: (a) Experimental dI/dV_S spectra over a range of gate voltages, using setpoints -650 mV and 4 nA for the sample bias and tunneling current, respectively, and a lock-in amplitude of 1 mV. As the gate is decreased from $V_B = 42$ to 30 V, narrow spectral peaks enter at positive sample biases and disperse towards negative biases. The TA is identified at the edges of this quantum dot tunneling regime. (b) dI/dV$_S$ curves at a high tunneling setpoint (2 nA) for a few choice back gate voltages which best show the TA dispersion. Hollow arrows point to the location of the TA at each gate voltage. (c) dI/dV$_S$ curves for a low tunneling setpoint (600 pA, further from the surface by around 0.5 Å). Again, the hollow arrows point to the TA, which disperses much faster than in (b).

Bibliography

[1] J. A. Schuller, E. S. Barnard, W. Cai, Y. C. Jun, J. S. White, and M. L. Brongersma, "Plasmonics for extreme light concentration and manipulation," *Nature Materials*, vol. 9, no. 3, p. 193, Mar. 2010, ISSN: 14761122. DOI: 10.1038/nmat2630.

[2] B. Slovick, Z. G. Yu, M. Berding, and S. Krishnamurthy, "Perfect dielectric-metamaterial reflector," *Physical Review B*, vol. 88, no. 16, p. 165 116, Oct. 2013, ISSN: 1098-0121, 1550-235X. DOI: 10.1103/PhysRevB.88.165116.

[3] *Photonic crystals: molding the flow of light*, 2nd ed. Princeton University Press, 2008, ISBN: 978-0-691-12456-8.

[4] H.-T. Chen, A. J. Taylor, and N. Yu, "A review of metasurfaces: Physics and applications," *Reports on Progress in Physics*, vol. 79, no. 7, p. 076 401, Jul. 2016, ISSN: 0034-4885, 1361-6633. DOI: 10.1088/0034-4885/79/7/076401.

[5] J. B. Pendry, A. J. Holden, D. J. Robbins, and W. J. Stewart, "Magnetism from conductors and enhanced nonlinear phenomena," *IEEE Transactions on Microwave Theory and Techniques*, vol. 47, no. 11, 2075–2084, Nov. 1999, ISSN: 0018-9480. DOI: 10.1109/22.798002.

[6] D. G. Baranov, Y. Xiao, I. A. Nechepurenko, A. Krasnok, A. Alù, and M. A. Kats, "Nanophotonic engineering of far-field thermal emitters," *Nature Materials*, vol. 18, no. 9, 920–930, Sep. 2019, ISSN: 1476-1122, 1476-4660. DOI: 10.1038/s41563-019-0363-y.

[7] J.-J. Greffet, R. Carminati, K. Joulain, J.-P. Mulet, S. Mainguy, and Y. Chen, "Coherent emission of light by thermal sources," *Nature*, vol. 416, no. 6876, 61–64, Mar. 2002, ISSN: 1476-4687. DOI: 10.1038/416061a.

[8] M. A. Kats *et al.*, "Vanadium dioxide as a natural disordered metamaterial: Perfect thermal emission and large broadband negative differential thermal emittance," *Physical Review X*, vol. 3, no. 4, p. 041 004, Oct. 2013. DOI: 10.1103/PhysRevX.3.041004.

[9] T. Inoue, A. Ji, M. De Zoysa, T. Asano, and S. Noda, "Electrical wavelength switching of thermal emitters based on quantum wells and photonic crystals," in *2016 Conference on Lasers and Electro-Optics (CLEO)*, Jun. 2016, 1–2.

[10] F. Yi, E. Shim, A. Y. Zhu, H. Zhu, J. C. Reed, and E. Cubukcu, "Voltage tuning of plasmonic absorbers by indium tin oxide," *Applied Physics Letters*, vol. 102, no. 22, p. 221 102, Jun. 2013, ISSN: 0003-6951. DOI: 10.1063/1.4809516.

[11] G. Kafaie Shirmanesh, R. Sokhoyan, R. A. Pala, and H. A. Atwater, "Dual-gated active metasurface at 1550 nm with wide (¿300°) phase tunability," *Nano Letters*, vol. 18, no. 5, 2957–2963, May 2018, ISSN: 1530-6984, 1530-6992. DOI: 10.1021/acs.nanolett.8b00351.

[12] A. Forouzmand, M. M. Salary, G. Kafaie Shirmanesh, R. Sokhoyan, H. A. Atwater, and H. Mosallaei, "Tunable all-dielectric metasurface for phase modulation of the reflected and transmitted light via permittivity tuning of indium tin oxide," *Nanophotonics*, vol. 8, no. 3, 415–427, Mar. 2019, ISSN: 2192-8614. DOI: 10.1515/nanoph-2018-0176.

[13] Y. Yao *et al.*, "Broad electrical tuning of graphene-loaded plasmonic antennas," *Nano Letters*, vol. 13, no. 3, 1257–1264, Mar. 2013, ISSN: 1530-6984. DOI: 10.1021/nl3047943.

[14] Y. Yao *et al.*, "Wide wavelength tuning of optical antennas on graphene with nanosecond response time," *Nano Letters*, vol. 14, no. 1, 214–219, Jan. 2014, ISSN: 1530-6984. DOI: 10.1021/nl403751p.

[15] G. R. Holdman *et al.*, "Dynamic band structure and capacitance effects in scanning tunneling spectroscopy of bilayer graphene," *Applied Physics Letters*, vol. 115, no. 18, p. 181 601, Oct. 2019, ISSN: 0003-6951. DOI: 10.1063/1.5127078.

[16] *Breakthrough initiatives*, https://breakthroughinitiatives.org/initiative/3, 2021. [Online]. Available: https://breakthroughinitiatives.org/initiative/3, (accessed: 07.11.2021).

[17] H. A. Atwater *et al.*, "Materials challenges for the starshot lightsail," *Nature Materials*, vol. 17, no. 1010, 861–867, Oct. 2018, ISSN: 1476-4660. DOI: 10.1038/s41563-018-0075-8.

[18] J. Siegel, A. Y. Wang, S. G. Menabde, M. A. Kats, M. S. Jang, and V. W. Brar, "Self-stabilizing laser sails based on optical metasurfaces," *ACS Photonics*, Jun. 2019. DOI: 10.1021/acsphotonics.9b00484. [Online]. Available: https://doi.org/10.1021/acsphotonics.9b00484.

[19] O. Ilic and H. A. Atwater, "Self-stabilizing photonic levitation and propulsion of nanostructured macroscopic objects," *Nature Photonics*, vol. 13, no. 4, 289–295, Apr. 2019, ISSN: 1749-4885, 1749-4893. DOI: 10.1038/s41566-019-0373-y.

[20] O. Ilic, C. M. Went, and H. A. Atwater, "Nanophotonic heterostructures for efficient propulsion and radiative cooling of relativistic light sails," *Nano Letters*, vol. 18, 5583––5589, 2018. DOI: 10.1021/acs.nanolett.8b02035.

[21] M. M. Salary and H. Mosallaei, "Photonic metasurfaces as relativistic light sails for doppler-broadened stable beam-riding and radiative cooling," *Laser & Photonics Reviews*, vol. 14, no. 8, p. 1 900 311, Aug. 2020, ISSN: 1863-8880, 1863-8899. DOI: 10.1002/lpor.201900311.

[22] W. Jin, W. Li, M. Orenstein, and S. Fan, "Inverse design of lightweight broadband reflector for relativistic lightsail propulsion," *ACS Photonics*, vol. 7, no. 9, 2350–2355, Sep. 2020, ISSN: 2330-4022, 2330-4022. DOI: 10.1021/acsphotonics.0c00768.

[23] H. Rogne, P. J. Timans, and H. Ahmed, "Infrared Absorption in Silicon at Elevated Temperatures," *Applied Physics Letters*, vol. 69, no. 15, pp. 2190–2192, 1996. DOI: 10.1063/1.117161. eprint: https://doi.org/10.1063/1.117161. [Online]. Available: https://doi.org/10.1063/1.117161.

[24] J. Degallaix *et al.*, "Bulk optical absorption of high resistivity silicon at 1550 nm," *Opt. Lett.*, vol. 38, no. 12, pp. 2047–2049, 2013. DOI: 10.1364/OL.38.002047. [Online]. Available: http://ol.osa.org/abstract.cfm?URI=ol-38-12-2047.

[25] A. D. Bristow, N. Rotenberg, and H. M. van Driel, "Two-Photon Absorption and Kerr Coefficients of Silicon for 850–2200nm," *Applied Physics Letters*, vol. 90, no. 19, p. 191 104, 2007. DOI: 10.1063/1.2737359. eprint: https://doi.org/10.1063/1.2737359. [Online]. Available: https://doi.org/10.1063/1.2737359.

[26] R. Kitamura, L. Pilon, and M. Jonasz, "Optical constants of silica glass from extreme ultraviolet to far infrared at near room temperature," *Applied Optics*, vol. 46, p. 8118, 2007. DOI: 10.1364/ao.46.008118.

[27] M. A. Green, "Self-Consistent Optical Parameters of Intrinsic Silicon at 300K Including Temperature Coefficients," *Solar Energy Materials and Solar Cells*, vol. 92, no. 11, pp. 1305–1310, 2008, ISSN: 0927-0248. DOI: https://doi.org/10.1016/j.solmat.2008.06.009. [Online]. Available: https://www.sciencedirect.com/science/article/pii/S0927024808002158.

[28] D. K. Schroder, R. N. Thomas, and J. C. Swartz, "Free Carrier Absorption in Silicon," *IEEE Journal of Solid-State Circuits*, vol. 13, no. 1, pp. 180–187, Feb. 1978, ISSN: 1558-173X. DOI: 10.1109/JSSC.1978.1051012.

[29] F. A. Johnson, "Lattice absorption bands in silicon," *Proceedings of the Physical Society*, vol. 73, no. 2, 265–272, Feb. 1959, ISSN: 0370-1328. DOI: 10.1088/0370-1328/73/2/315.

[30] E. J. Wollack, G. Cataldo, K. H. Miller, and M. A. Quijada, "Infrared properties of high-purity silicon," *Optics Letters*, vol. 45, no. 17, p. 4935, Sep. 2020, ISSN: 0146-9592, 1539-4794. DOI: 10.1364/OL.393847.

[31] H. Lee *et al.*, "Chemically etched ultrahigh-q wedge-resonator on a silicon chip," *Nature Photonics*, vol. 6, no. 6, 369–373, Jun. 2012, ISSN: 1749-4885, 1749-4893. DOI: 10.1038/nphoton.2012.109.

[32] R. Couderc, M. Amara, and M. Lemiti, "Reassessment of the Intrinsic Carrier Density Temperature Dependence in Crystalline Silicon," *J. Appl. Phys.*, vol. 115, no. 9, p. 093 705, 2014. DOI: 10.1063/1.4867776. eprint: https://doi.org/10.1063/1.4867776. [Online]. Available: https://doi.org/10.1063/1.4867776.

[33] O. J. Edwards, "Optical absorption coefficients of fused silica in the wavelength range 0.17 to 3.5 microns from room temperature to 980° c," NASA, Technical Note D-3257, 1966.

[34] A. Dvurechensky, V. Petrov, and V. Yu Reznik, "Spectral emissivity and absorption coefficient of silica glass at extremely high temperatures in the semitransparent region," *Infrared Physics*, vol. 19, no. 3, pp. 465–469, 1979, ISSN: 0020-0891. DOI: https://doi.org/10.1016/0020-0891(79)90060-5. [Online]. Available: https://www.sciencedirect.com/science/article/pii/0020089179900605.

[35] C. Tan and J. Arndt, "Temperature dependence of refractive index of glassy sio2 in the infrared wavelength range," *Journal of Physics and Chemistry of Solids*, vol. 61, no. 8, pp. 1315–1320, 2000, ISSN: 0022-3697. DOI: https://doi.org/10.1016/S0022-3697(99)00411-4. [Online]. Available: https://www.sciencedirect.com/science/article/pii/S0022369799004114.

[36] J. E. Sipe, "New green-function formalism for surface optics," *Journal of the Optical Society of America B*, vol. 4, no. 4, p. 481, Apr. 1987, ISSN: 0740-3224, 1520-8540. DOI: 10.1364/JOSAB.4.000481.

[37] N. Kulkarni, P. Lubin, and Q. Zhang, "Relativistic spacecraft propelled by directed energy," *The Astronomical Journal*, vol. 155, no. 4, p. 155, Mar. 2018, ISSN: 1538-3881. DOI: 10.3847/1538-3881/aaafd2.

[38] Z. Manchester and A. Loeb, "Stability of a light sail riding on a laser beam," *The Astrophysical Journal*, vol. 837, no. 2, p. L20, Mar. 2017, ISSN: 2041-8213. DOI: 10.3847/2041-8213/aa619b.

[39] G. A. Swartzlander, "Radiation pressure on a diffractive sailcraft," *Journal of the Optical Society of America B*, vol. 34, no. 6, p. C25, Jun. 2017, ISSN: 0740-3224, 1520-8540. DOI: 10.1364/JOSAB.34.000C25.

[40] J. Cai, Y. Ishikawa, and K. Wada, "Strain induced bandgap and refractive index variation of silicon," *Optics Express*, vol. 21, no. 6, 7162–7170, Mar. 2013, ISSN: 1094-4087. DOI: 10.1364/OE.21.007162.

[41] W. B. Jackson, N. M. Johnson, and D. K. Biegelsen, "Density of gap states of silicon grain boundaries determined by optical absorption," en, *Applied Physics Letters*, vol. 43, no. 2, 195–197, Jul. 1983, ISSN: 0003-6951, 1077-3118. DOI: 10.1063/1.94278.

[42] A. R. Davoyan, J. N. Munday, N. Tabiryan, G. A. Swartzlander, and L. Johnson, "Photonic materials for interstellar solar sailing," *Optica*, vol. 8, no. 5, pp. 722–734, May 2021. DOI: 10.1364/OPTICA.417007. [Online]. Available: http://www.osapublishing.org/optica/abstract.cfm?URI=optica-8-5-722.

[43] W. Jin, C. Guo, M. Orenstein, and S. Fan, "Adaptive four-level modeling of laser cooling of solids," *arXiv:2109.02702 [cond-mat, physics:physics]*, Sep. 2021, arXiv: 2109.02702. [Online]. Available: http://arxiv.org/abs/2109.02702.

[44] P. R. Wray, M. P. Su, and H. A. Atwater, "Design of efficient radiative emission and daytime cooling structures with si 3 n 4 and sio 2 nanoparticle laminate films," *Optics Express*, vol. 28, no. 24, p. 35 784, Nov. 2020, ISSN: 1094-4087. DOI: 10.1364/OE.408845.

[45] J. Brewer *et al.*, "Multi-scale photonic emissivity engineering for relativistic lightsail thermal regulation," *arXiv:2106.03558 [astro-ph, physics:physics]*, Sep. 2021, arXiv: 2106.03558. [Online]. Available: http://arxiv.org/abs/2106.03558.

[46] A. M. Morsy and M. L. Povinelli, "Coupled metamaterial optical resonators for infrared emissivity spectrum modulation," *Opt. Express*, vol. 29, no. 4, pp. 5840–5847, Feb. 2021. DOI: 10.1364/OE.414713. [Online]. Available: http://www.osapublishing.org/oe/abstract.cfm?URI=oe-29-4-5840.

[47] B.-U. Sohn, J. W. Choi, D. K. T. Ng, and D. T. H. Tan, "Optical nonlinearities in ultra-silicon-rich nitride characterized using z-scan measurements," *Scientific Reports*, vol. 9, no. 1, p. 10 364, Dec. 2019, ISSN: 2045-2322. DOI: 10.1038/s41598-019-46865-7.

[48] S. Singhal, "Thermodynamic analysis of the high-temperature stability of silicon nitride and silicon carbide," *Ceramurgia International*, vol. 2, no. 3, pp. 123–130, 1976, ISSN: 0390-5519. DOI: https://doi.org/10.1016/0390-5519(76)90022-3. [Online]. Available: https://www.sciencedirect.com/science/article/pii/0390551976900223.

[49] M. Pradhan, R. Garg, and M. Arora, "Multiphonon infrared absorption in silicon," *Infrared Physics*, vol. 27, no. 1, pp. 25–30, 1987, ISSN: 0020-0891. DOI: https://doi.org/10.1016/0020-0891(87)90046-7. [Online]. Available: https://www.sciencedirect.com/science/article/pii/0020089187900467.

[50] M. S. Vitiello, G. Scalari, B. Williams, and P. D. Natale, "Quantum cascade lasers: 20 years of challenges," EN, *Optics Express*, vol. 23, no. 4, 5167–5182, Feb. 2015, ISSN: 1094-4087. DOI: 10.1364/OE.23.005167.

[51] H. I. Schiff, G. I. Mackay, and J. Bechara, "The use of tunable diode laser absorption spectroscopy for atmospheric measurements," *Research on Chemical Intermediates*, vol. 20, no. 3–5, 525–556, Jan. 1994, ISSN: 0922-6168, 1568-5675. DOI: 10.1163/156856794X00441.

[52] M. Sigrist, R. Bartlome, D. Marinov, J. Rey, D. Vogler, and H. Wächter, "Trace gas monitoring with infrared laser-based detection schemes," *Applied Physics B*, vol. 90, no. 2, 289–300, Feb. 2008, ISSN: 0946-2171, 1432-0649. DOI: 10.1007/s00340-007-2875-4.

[53] F. Capasso, "Band-gap engineering: From physics and materials to new semiconductor devices," *Science*, vol. 235, no. 4785, 172–176, 1987, ISSN: 0036-8075.

[54] J. Faist, F. Capasso, D. L. Sivco, C. Sirtori, A. L. Hutchinson, and A. Y. Cho, "Quantum cascade laser," *Science*, vol. 264, no. 5158, 553–556, 1994, ISSN: 0036-8075.

[55] M. Beck, D. Hofstetter, T. Aellen, J. Faist, and e. al, "Continuous wave operation of a mid-infrared semiconductor laser at room temparature," *Science; Washington*, vol. 295, no. 5553, 301–5, Jan. 2002, ISSN: 00368075.

[56] R. V. Kochanov, I. E. Gordon, L. S. Rothman, P. Wcisło, C. Hill, and J. S. Wilzewski, "Hitran application programming interface (hapi): A comprehensive approach to working with spectroscopic data," en, XVIIIth Symposium on High Resolution Molecular Spectroscopy (HighRus-2015), Tomsk, Russia, vol. 177, 15–30, 2016, ISSN: 0022-4073. DOI: 10.1016/j.jqsrt.2016.03.005.

[57] J. A. Silver, "Frequency-modulation spectroscopy for trace species detection: Theory and comparison among experimental methods," en, *Applied Optics*, vol. 31, no. 6, p. 707, Feb. 1992, ISSN: 0003-6935, 1539-4522. DOI: 10.1364/AO.31.000707.

[58] D. S. Bomse, A. C. Stanton, and J. A. Silver, "Frequency modulation and wavelength modulation spectroscopies: Comparison of experimental methods using a lead-salt diode laser," en, *Applied Optics*, vol. 31, no. 6, p. 718, Feb. 1992, ISSN: 0003-6935, 1539-4522. DOI: 10.1364/AO.31.000718.

[59] K. Namjou *et al.*, "Sensitive absorption spectroscopy with a room-temperature distributed-feedback quantum-cascade laser," en, *Optics Letters*, vol. 23, no. 3, p. 219, Feb. 1998, ISSN: 0146-9592, 1539-4794. DOI: 10.1364/OL.23.000219.

[60] A. A. Kosterev *et al.*, "Thermoelectrically cooled quantum-cascade-laser-based sensor for the continuous monitoring of ambient atmospheric carbon monoxide," en, *Applied Optics*, vol. 41, no. 6, p. 1169, Feb. 2002, ISSN: 0003-6935, 1539-4522. DOI: 10.1364/AO.41.001169.

[61] L. Menzel *et al.*, "Spectroscopic detection of biological no with a quantum cascade laser:" en, *Applied Physics B*, vol. 72, no. 7, 859–863, May 2001, ISSN: 0946-2171, 1432-0649. DOI: 10.1007/s003400100562.

[62] A. A. Kosterev *et al.*, "Transportable automated ammonia sensor based on a pulsed thermoelectrically cooled quantum-cascade distributed feedback laser," en, *Applied Optics*, vol. 41, no. 3, p. 573, Jan. 2002, ISSN: 0003-6935, 1539-4522. DOI: 10.1364/AO.41.000573.

[63] L. Tao, K. Sun, M. A. Khan, D. J. Miller, and M. A. Zondlo, "Compact and portable open-path sensor for simultaneous measurements of atmospheric n_2o and co using a quantum cascade laser," en, *Optics Express*, vol. 20, no. 27, p. 28 106, Dec. 2012, ISSN: 1094-4087. DOI: 10.1364/OE.20.028106.

[64] T. Plank, E. Leitgeb, P. Pezzei, and Z. Ghassemlooy, "Wavelength-selection for high data rate free space optics (fso) in next generation wireless communications," in *2012 17th European Conference on Networks and Optical Communications*, IEEE, Jun. 2012, 1–5, ISBN: 978-1-4673-0951-6. DOI: 10.1109/NOC.2012.6249909. [Online]. Available: http://ieeexplore.ieee.org/document/6249909/.

[65] J. J. Liu, B. L. Stann, K. K. Klett, P. S. Cho, and P. M. Pellegrino, "Mid and long-wave infrared free-space optical communication," in *Laser Communication and Propagation through the Atmosphere and Oceans VIII*, A. M. van Eijk, S. Hammel, and J. P. Bos, Eds., SPIE, Sep. 2019, p. 1, ISBN: 978-1-5106-2959-2.

[66] X. Pang *et al.*, "Gigabit free-space multi-level signal transmission with a mid-infrared quantum cascade laser operating at room temperature," *Optics Letters*, vol. 42, no. 18, p. 3646, Sep. 2017, ISSN: 0146-9592, 1539-4794. DOI: 10.1364/OL.42.003646.

[67] C. Colvero, M. Cordeiro, and J. von der Weid, "Real-time measurements of visibility and transmission in far-, mid- and near-ir free space optical links," *Electronics Letters*, vol. 41, no. 10, p. 610, 2005, ISSN: 00135194. DOI: 10.1049/el:20050668.

[68] K. Du *et al.*, "Wavelength-tunable mid-infrared thermal emitters with a non-volatile phase changing material," en, *Nanoscale*, vol. 10, no. 9, 4415–4420, Mar. 2018, ISSN: 2040-3372. DOI: 10.1039/C7NR09672K.

[69] X. Liu and W. J. Padilla, "Dynamic manipulation of infrared radiation with mems metamaterials," en, *Advanced Optical Materials*, vol. 1, no. 8, 559–562, Aug. 2013, ISSN: 21951071. DOI: 10.1002/adom.201300163.

[70] X. Liu, T. Tyler, T. Starr, A. F. Starr, N. M. Jokerst, and W. J. Padilla, "Taming the blackbody with infrared metamaterials as selective thermal emitters," *Physical Review Letters*, vol. 107, no. 4, p. 045 901, Jul. 2011. DOI: 10.1103/PhysRevLett.107.045901.

[71] N. Papasimakis *et al.*, "Graphene in a photonic metamaterial," *Optics Express*, vol. 18, no. 8, p. 8353, Apr. 2010, ISSN: 1094-4087. DOI: 10.1364/OE.18.008353.

[72] L. Ju *et al.*, "Graphene plasmonics for tunable terahertz metamaterials," *Nature Nanotechnology*, vol. 6, no. 10, 630–634, Oct. 2011, ISSN: 1748-3395. DOI: 10.1038/nnano.2011.146.

[73] Z. Li and N. Yu, "Modulation of mid-infrared light using graphene-metal plasmonic antennas," *Applied Physics Letters*, vol. 102, no. 13, p. 131 108, Apr. 2013, ISSN: 0003-6951. DOI: 10.1063/1.4800931.

[74] Y. Yao *et al.*, "Electrically tunable metasurface perfect absorbers for ultrathin mid-infrared optical modulators," *Nano Letters*, vol. 14, no. 11, 6526–6532, Nov. 2014, ISSN: 1530-6984. DOI: 10.1021/nl503104n.

[75] R. L. Olmon *et al.*, "Optical dielectric function of gold," *Physical Review B*, vol. 86, no. 23, p. 235 147, Dec. 2012. DOI: 10.1103/PhysRevB.86.235147.

[76] A. Majumdar, J. Kim, J. Vuckovic, and F. Wang, "Electrical control of silicon photonic crystal cavity by graphene," en, *Nano Letters*, vol. 13, no. 2, 515–518, Feb. 2013, ISSN: 1530-6984, 1530-6992. DOI: 10.1021/nl3039212.

[77] X. Gan *et al.*, "High-contrast electrooptic modulation of a photonic crystal nanocavity by electrical gating of graphene," en, *Nano Letters*, vol. 13, no. 2, 691–696, Feb. 2013, ISSN: 1530-6984, 1530-6992. DOI: 10.1021/nl304357u.

[78] R.-J. Shiue *et al.*, "Thermal radiation control from hot graphene electrons coupled to a photonic crystal nanocavity," *Nature Communications*, vol. 10, no. 1, Dec. 2019, ISSN: 2041-1723. DOI: 10.1038/s41467-018-08047-3. [Online]. Available: http://www.nature.com/articles/s41467-018-08047-3.

[79] R. Shankar *et al.*, "Electro-optic tuning of mid-infrared photonic crystal cavities using graphene," in *CLEO: 2013*, OSA, 2013, CTu1F.5, ISBN: 978-1-55752-972-5. DOI: 10.1364/CLEO_SI.2013.CTu1F.5. [Online]. Available: https://www.osapublishing.org/abstract.cfm?URI=CLEO_SI-2013-CTu1F.5.

[80] S. Edalatpour and M. Francoeur, "The thermal discrete dipole approximation (t-dda) for near-field radiative heat transfer simulations in three-dimensional arbitrary geometries," en, *Journal of Quantitative Spectroscopy and Radiative Transfer*, vol. 133, 364–373, Jan. 2014, ISSN: 00224073. DOI: 10.1016/j.jqsrt.2013.08.021.

[81] G. Kirchhoff, "Ueber das verhältniss zwischen dem emissionsvermögen und dem absorptionsvermögen der körper für wärme und licht," *Annalen der Physik und Chemie*, vol. 185, no. 2, 275–301, 1860, ISSN: 00033804, 15213889. DOI: 10.1002/andp.18601850205.

[82] J. D. Jackson, *Classical Electrodynamics*, 3rd. New York, NY: Wiley, 1999.

[83] P. J. Hesketh, J. N. Zemel, and B. Gebhart, "Polarized spectral emittance from periodic micromachined surfaces. ii. doped silicon: Angular variation," *Physical Review B*, vol. 37, no. 18, 10803–10813, Jun. 1988, ISSN: 0163-1829. DOI: 10.1103/PhysRevB.37.10803.

[84] J. Hildenbrand *et al.*, "Fast transient temperature operating micromachined emitter for mid-infrared optical gas sensing systems: Design, fabrication, characterization and optimization," *Microsystem Technologies*, vol. 16, no. 5, 745–754, May 2010, ISSN: 0946-7076, 1432-1858. DOI: 10.1007/s00542-010-1049-1.

[85] A. Tittl *et al.*, "A switchable mid-infrared plasmonic perfect absorber with multispectral thermal imaging capability," *Advanced Materials*, vol. 27, no. 31, 4597–4603, Aug. 2015, ISSN: 09359648. DOI: 10.1002/adma.201502023.

[86] A. H. Castro Neto, F. Guinea, N. M. R. Peres, K. S. Novoselov, and A. K. Geim, "The electronic properties of graphene," *Reviews of Modern Physics*, vol. 81, no. 1, 109–162, Jan. 2009. DOI: 10.1103/RevModPhys.81.109.

[87] Y. Song, W. Fang, A. L. Hsu, and J. Kong, "Iron (iii) chloride doping of cvd graphene," *Nanotechnology*, vol. 25, no. 39, p. 395 701, Sep. 2014, ISSN: 0957-4484. DOI: 10.1088/0957-4484/25/39/395701.

[88] J. A. Kong, *Electromagnetic wave theory*. EMW Publishing, 2000, ISBN: 978-0-9668143-9-2.

[89] S. G. Johnson, M. Ibanescu, M. A. Skorobogatiy, O. Weisberg, J. D. Joannopoulos, and Y. Fink, "Perturbation theory for maxwell's equations with shifting material boundaries," *Physical Review E*, vol. 65, no. 6, p. 066 611, Jun. 2002. DOI: 10.1103/PhysRevE.65.066611.

[90] L. Verslegers, Z. Yu, P. B. Catrysse, and S. Fan, "Temporal coupled-mode theory for resonant apertures," EN, *JOSA B*, vol. 27, no. 10, 1947–1956, Oct. 2010, ISSN: 1520-8540. DOI: 10.1364/JOSAB.27.001947.

[91] J. Y. Kim *et al.*, "Full 2 tunable phase modulation using avoided crossing of resonances," *Nature Communications*,

[92] J. von Neumann and E. Wigner, "Über merkwürdige diskrete eigenwerte," *Phys. Z.*, vol. 30, 465–467, 1929.

[93] C. W. Hsu, B. Zhen, A. D. Stone, J. D. Joannopoulos, and M. Soljačić, "Bound states in the continuum," *Nature Reviews Materials*, vol. 1, no. 9, 1–13, Jul. 2016, ISSN: 2058-8437. DOI: 10.1038/natrevmats.2016.48.

[94] A. C. Overvig, S. C. Malek, M. J. Carter, S. Shrestha, and N. Yu, "Selection rules for quasibound states in the continuum," *Physical Review B*, vol. 102, no. 3, Jul. 2020, ISSN: 2469-9950, 2469-9969. DOI: 10.1103/PhysRevB.102.035434.

[95] A. C. Overvig, S. Shrestha, and N. Yu, "Dimerized high contrast gratings," *Nanophotonics*, vol. 7, no. 6, 1157–1168, Jun. 2018, ISSN: 2192-8614. DOI: 10.1515/nanoph-2017-0127.

[96] C. W. Hsu *et al.*, "Observation of trapped light within the radiation continuum," en$_U$*S*, *MIT web domain*, Jul. 2013, ISSN: 0028-0836. [Online]. Available: https://dspace.mit.edu/handle/1721.1/110846.

[97] S. Campione *et al.*, "Broken symmetry dielectric resonators for high quality factor fano metasurfaces," *ACS Photonics*, vol. 3, no. 12, 2362–2367, Dec. 2016. DOI: 10.1021/acsphotonics.6b00556.

[98] A. Tittl *et al.*, "Imaging-based molecular barcoding with pixelated dielectric metasurfaces," en, *Science*, vol. 360, no. 6393, 1105–1109, Jun. 2018, ISSN: 0036-8075, 1095-9203. DOI: 10.1126/science.aas9768.

[99] F. Yesilkoy *et al.*, "Ultrasensitive hyperspectral imaging and biodetection enabled by dielectric metasurfaces," en, *Nature Photonics*, vol. 13, no. 6, 390–396, Jun. 2019, ISSN: 1749-4885, 1749-4893. DOI: 10.1038/s41566-019-0394-6.

[100] Z. Liu *et al.*, "High- q quasibound states in the continuum for nonlinear metasurfaces," en, *Physical Review Letters*, vol. 123, no. 25, p. 253 901, Dec. 2019, ISSN: 0031-9007, 1079-7114. DOI: 10.1103/PhysRevLett.123.253901.

[101] A. Kodigala, T. Lepetit, Q. Gu, B. Bahari, Y. Fainman, and B. Kanté, "Lasing action from photonic bound states in continuum," en, *Nature*, vol. 541, no. 7636, 196–199, Jan. 2017, ISSN: 0028-0836, 1476-4687. DOI: 10.1038/nature20799.

[102] V. Karagodsky, F. G. Sedgwick, and C. J. Chang-Hasnain, "Theoretical analysis of subwavelength high contrast grating reflectors," *Optics Express*, vol. 18, no. 16, p. 16 973, Aug. 2010, ISSN: 1094-4087. DOI: 10.1364/OE.18.016973.

[103] J. M. Foley, S. M. Young, and J. D. Phillips, "Symmetry-protected mode coupling near normal incidence for narrow-band transmission filtering in a dielectric grating," *Physical Review B*, vol. 89, no. 16, p. 165 111, Apr. 2014. DOI: 10.1103/PhysRevB.89.165111.

[104] J. M. Foley, S. M. Young, and J. D. Phillips, "Narrowband mid-infrared transmission filtering of a single layer dielectric grating," *Applied Physics Letters*, vol. 103, no. 7, p. 071 107, Aug. 2013, ISSN: 0003-6951, 1077-3118. DOI: 10.1063/1.4818735.

[105] B. Zeng, A. Majumdar, and F. Wang, "Tunable dark modes in one-dimensional "diatomic" dielectric gratings," *Optics Express*, vol. 23, no. 10, p. 12 478, May 2015, ISSN: 1094-4087. DOI: 10.1364/OE.23.012478.

[106] J. Kischkat *et al.*, "Mid-infrared optical properties of thin films of aluminum oxide, titanium dioxide, silicon dioxide, aluminum nitride, and silicon nitride," *Applied Optics*, vol. 51, no. 28, 6789–6798, Oct. 2012, ISSN: 2155-3165. DOI: 10.1364/AO.51.006789.

[107] W. W. Salisbury, *Absorbent body for electromagnetic waves*, Jun. 1952.

[108] S. Thongrattanasiri, F. H. L. Koppens, and F. J. García de Abajo, "Complete optical absorption in periodically patterned graphene," *Physical Review Letters*, vol. 108, no. 4, p. 047 401, Jan. 2012, ISSN: 0031-9007, 1079-7114. DOI: 10.1103/PhysRevLett.108.047401.

[109] M. S. Jang *et al.*, "Tunable large resonant absorption in a midinfrared graphene salisbury screen," *Physical Review B*, vol. 90, no. 16, p. 165 409, Oct. 2014. DOI: 10.1103/PhysRevB.90.165409.

[110] J. Park, S. Kim, D. W. Nam, H. Chung, C. Y. Park, and M. S. Jang, "Free-form optimization of nanophotonic devices: From classical methods to deep learning," *Nanophotonics*, vol. 0, no. 0, Jan. 2022, ISSN: 2192-8614, 2192-8606. DOI: 10.1515/nanoph-2021-0713.

[111] Y. Zhang, L. Zhang, and C. Zhou, "Review of chemical vapor deposition of graphene and related applications," en, *Accounts of Chemical Research*, vol. 46, no. 10, 2329–2339, Oct. 2013, ISSN: 0001-4842, 1520-4898. DOI: 10.1021/ar300203n.

[112] S. A. Scott and M. G. Lagally, "Elastically strain-sharing nanomembranes: Flexible and transferable strained silicon and silicon–germanium alloys," *Journal of Physics D: Applied Physics*, vol. 40, no. 4, R75–R92, Feb. 2007, ISSN: 0022-3727. DOI: 10.1088/0022-3727/40/4/R01.

[113] J. C. Spear, J. P. Custer, and J. D. Batteas, "The influence of nanoscale roughness and substrate chemistry on the frictional properties of single and few layer graphene," en, *Nanoscale*, vol. 7, no. 22, 10021–10029, 2015, ISSN: 2040-3364, 2040-3372. DOI: 10.1039/C5NR01478F.

[114] H. Yang, A. Jin, Q. Luo, J. Li, C. Gu, and Z. Cui, "Electron beam lithography of hsq/pmma bilayer resists for negative tone lift-off process," *Microelectronic Engineering*, Proceedings of the Micro- and Nano-Engineering 2007 Conference, vol. 85, no. 5, 814–817, May 2008, ISSN: 0167-9317. DOI: 10.1016/j.mee.2008.01.006.

[115] Y. Xiao *et al.*, "Guidelines for measurement of thermal emission," *arXiv:1911.03591 [physics]*, Nov. 2019, arXiv: 1911.03591. [Online]. Available: http://arxiv.org/abs/1911.03591.

[116] T. Amotchkina, M. Trubetskov, D. Hahner, and V. Pervak, "Characterization of e-beam evaporated ge, ybf 3 , zns, and laf 3 thin films for laser-oriented coatings," *Applied Optics*, vol. 59, no. 5, A40, Feb. 2020, ISSN: 1559-128X, 2155-3165. DOI: 10.1364/AO.59.000A40.

[117] M. Gehrtz, E. A. Whittaker, and G. C. Bjorklund, "Quantum-limited laser frequency-modulation spectroscopy," en, *Journal of the Optical Society of America B*, vol. 2, no. 9, p. 1510, Sep. 1985, ISSN: 0740-3224, 1520-8540. DOI: 10.1364/JOSAB.2.001510.

[118] G. C. Bjorklund and E. A. Whittaker, "High sensitivity frequency modulation spectroscopy and the path to single molecule detection," en, *The Journal of Physical Chemistry A*, vol. 125, no. 39, 8519–8528, 2021, ISSN: 1089-5639, 1520-5215. DOI: 10.1021/acs.jpca.1c05752.

[119] L. W. Couch, *Digital and analog communication systems*, en, 8th ed. Upper Saddle River, N.J: Pearson, 2013, ISBN: 978-0-13-291538-0.

[120] Y. Zhang *et al.*, "Direct observation of a widely tunable bandgap in bilayer graphene," *Nature*, vol. 459, pp. 820–823, 2009.

[121] Y. Cao *et al.*, "Correlated insulator behaviour at half-filling in magic-angle graphene superlattices," *Nature*, vol. 556, pp. 80–84, 2018.

[122] Y. Cao *et al.*, "Unconventional superconductivity in magic-angle graphene superlattices," *Nature*, vol. 556, pp. 43–50, 2018.

[123] M. Yankowitz *et al.*, "Tuning superconductivity in twisted bilayer graphene," *Science*, vol. 363, pp. 1059–1064, 2018.

[124] A. Kerelsky *et al.*, "Magic angle spectroscopy," *Nature*, vol. 572, 95–100, 2019.

[125] Y. Choi *et al.*, "Imaging electronic correlations in twisted bilayer graphene near the magic angle," *arXiv:1901.02997*, 2019.

[126] A. Lucas and S. Das Sarma, "Electronic hydrodynamics and the breakdown of the wiedemann-franz and mott laws in interacting metals," *Phys. Rev. B*, vol. 97, p. 245 128, 2018.

[127] D. A. Bandurin *et al.*, "Negative local resistance caused by viscous electron backflow in graphene," *Science*, vol. 351, pp. 1055–1058, 2016.

[128] J. Crossno *et al.*, "Observation of the Dirac fluid and the breakdown of the Wiedemann-Franz law in graphene," *Science*, vol. 351, pp. 1058–1061, 2015.

[129] M. Yankowitz *et al.*, "Band structure mapping of bilayer graphene via quasiparticle scattering," *APL Mater.*, vol. 2, p. 092 503, 2014.

[130] G. M. Rutter, S. Jung, N. N. Klimov, D. B. Newell, N. B. Zhitenev, and J. A. Stroscio, "Microscopic polarization in bilayer graphene," *Nat. Phys.*, vol. 7, pp. 649–655, 2011.

[131] A. Deshpande, W. Bao, Z. Zhao, C. Lau, and B. LeRoy, "Mapping the dirac point in gated bilayer graphene," *App. Phys. Lett.*, vol. 95, p. 243 502, 24 2009.

[132] J. Velasco Jr *et al.*, "Visualization and control of single-electron charging in bilayer graphene quantum dots," *Nano letters*, vol. 18, no. 8, pp. 5104–5110, 2018.

[133] A. Young *et al.*, "Electronic compressibility of layer-polarized bilayer graphene," *Phys. Rev. B*, vol. 85, p. 235 458, 2012.

[134] S. Jung *et al.*, "Direct probing of the electronic structures of single-layer and bilayer graphene with a hexagonal boron nitride tunneling barrier," *Nano Lett.*, vol. 17, pp. 206–213, 2017.

[135] J. Oostinga, H. Heersche, X. Liu, A. Morpurgo, and L. Vandersypen, "Gate-induced insulating state in bilayer graphene devices," *Nat. Mater.*, vol. 7, pp. 151–157, 2 2008.

[136] S. de la Barrera and R. Feenstra, "Theory of resonant tunneling in bilayer-graphene/hexagonal-boron-nitride heterostructures," *Appl. Phys. Lett.*, vol. 106, p. 093 115, 2015.

[137] D. Abergel, E. Hwang, and S. Das Sarma, "Compressibility of graphene," *Phys. Rev. B*, vol. 83, p. 085 429, 2011.

[138] E. McCann, "Asymmetry gap in the electronic band structure of bilayer graphene," *Phys. Rev. B*, vol. 74, p. 161 403, 2006.

[139] A. Young and L. Levitov, "Capacitance of graphene bilayer as a probe of layer-specific properties," *Phys. Rev. B*, vol. 84, p. 085 441, 2011.

[140] C. J. Chen, *Introduction to Scanning Tunneling Microscopy*, 2nd ed. Oxford University Press, 2008.

[141] E. McCann and M. Koshino, "The electronic properties of bilayer graphene," *Rep. Prog. Phys.*, vol. 76, p. 056 503, 2013.

[142] L Esaki and P. Stiles, "New type of negative resistance in barrier tunneling," *Physical Review Letters*, vol. 16, no. 24, p. 1108, 1966.

[143] X. Tu, G. Mikaelian, and W. Ho, "Controlling single-molecule negative differential resistance in a double-barrier tunnel junction," *Physical review letters*, vol. 100, no. 12, p. 126 807, 2008.

[144] M Grobis, A Wachowiak, R Yamachika, and M. Crommie, "Tuning negative differential resistance in a molecular film," *Applied Physics Letters*, vol. 86, no. 20, p. 204 102, 2005.

[145] N. P. Guisinger, N. L. Yoder, and M. C. Hersam, "Probing charge transport at the single-molecule level on silicon by using cryogenic ultra-high vacuum scanning tunneling microscopy," *Proceedings of the National Academy of Sciences*, vol. 102, no. 25, pp. 8838–8843, 2005.

[146] J. Repp, G. Meyer, S. M. Stojković, A. Gourdon, and C. Joachim, "Molecules on insulating films: Scanning-tunneling microscopy imaging of individual molecular orbitals," *Physical Review Letters*, vol. 94, no. 2, p. 026 803, 2005.

[147] Z. Lu, R. Khangura, M. Dharma-Wardana, M. Z. Zgierski, and D. Ritchie, "Molecular electronics, negative differential resistance, and resonant tunneling in a poled molecular layer on al/ lif electrodes having a sharp density of states," *Applied physics letters*, vol. 85, no. 2, pp. 323–325, 2004.

[148] C. Zeng, H. Wang, B. Wang, J. Yang, and J. Hou, "Negative differential-resistance device involving two c 60 molecules," *Applied Physics Letters*, vol. 77, no. 22, pp. 3595–3597, 2000.

[149] I.-W. Lyo and P. Avouris, "Negative differential resistance on the atomic scale: Implications for atomic scale devices," *Science*, vol. 245, no. 4924, pp. 1369–1371, 1989.

[150] J Gaudioso, L. Lauhon, and W Ho, "Vibrationally mediated negative differential resistance in a single molecule," *Physical review letters*, vol. 85, no. 9, p. 1918, 2000.

[151] J Chen, M. Reed, A. Rawlett, and J. Tour, "Large on-off ratios and negative differential resistance in a molecular electronic device," *science*, vol. 286, no. 5444, pp. 1550–1552, 1999.

[152] P Bedrossian, D. Chen, K Mortensen, and J. Golovchenko, "Demonstration of the tunnel-diode effect on an atomic scale," *Nature*, vol. 342, no. 6247, p. 258, 1989.

[153] Y. Xie *et al.*, "Spectroscopic signatures of many-body correlations in magic-angle twisted bilayer graphene," *Nature*, vol. 572, pp. 101–105, 2019.

[154] Y. Jiang *et al.*, "Charge order and broken rotational symmetry in magic-angle twisted bilayer graphene," *Nature*, pp. 1–5, 2019.

[155] W Chen, V Madhavan, T Jamneala, and M. Crommie, "Scanning tunneling microscopy observation of an electronic superlattice at the surface of clean gold," *Phys. Rev. Lett.*, vol. 80, no. 7, p. 1469, 1998.

[156] Y. Zhang *et al.*, "Giant phonon-induced conductance in scanning tunnelling spectroscopy of gate-tunable graphene," *Nat. Phys.*, vol. 4, p. 627, 8 2008.

[157] J. Jung, F. Zhang, and A. MacDonald, "Lattice theory of pseudospin ferromagnetism in bilayer graphene: Competing interaction-induced quantum hall states," *Phys. Rev. B.*, vol. 83, p. 115 408, 11 2011.

[158] R. Nandkishore and L. Levitov, "Dynamical screening and excitonic instability in bilayer graphene," *Phys. Rev. Lett.*, vol. 104, p. 156 803, 15 2010.

[159] R. Weitz, M. Allen, B. Feldman, J. Martin, and A. Yacoby, "Broken symmetry states in doubly gated suspended bilayer graphene," *Science*, vol. 330, pp. 812–816, 2010.

[160] A. Ramasubramaniam, D. Naveh, and E. Towe, "Tunable band gaps in bilayer graphene-bn heterostructures," *Nano Lett.*, vol. 11, pp. 1070–1075, 3 2011.

[161] M. Mucha-Kruczyński, J. Wallbank, and V. Fal'ko, "Heterostructures of bilayer graphene and *h*-bn: Interplay between misalignment, interlayer asymmetry, and trigonal warping.," *Phys. Rev. B*, vol. 88, p. 205 418, 2013.

[162] P. Moon and M. Koshino, "Electronic properties of graphene hexagonal boron nitride moire superlattice," *Phys. Rev. B*, vol. 90, p. 155 406, 2014.

[163] R Dombrowski, C. Steinebach, C. Wittneven, M Morgenstern, and R Wiesendanger, "Tip-induced band bending by scanning tunneling spectroscopy of the states of the tip-induced quantum dot on inas (110)," *Physical Review B*, vol. 59, no. 12, p. 8043, 1999.

[164] J. Lopes dos Santos, N. Peres, and A. Castro Neto, "Graphene bilayer with a twist: Electronic structure," *Phys. Rev. Lett.*, vol. 99, p. 256 802, 25 2007.

[165] L. Zou, H. Po, V. Vishwanath, and T. Senthil, "Band structure of twisted bilayer graphene: Emergent symmetries, commensurate approximants and wannier obstructions," *Phys. Rev. B*, vol. 98, p. 085 435, 8 2018.

[166] A. Ramasubramaniam, D. Naveh, and E. Towe, "Tunable band gaps in bilayer transition-metal dichalcogenides," *Phys. Rev. B*, vol. 84, p. 205 325, 20 2011.

[167] S. Wu *et al.*, "Electrical tuning of valley magnetic moment through symmetry control in bilayer mos¡sub¿2¡/sub¿," *Nat. Phys.*, vol. 9, p. 149, 3 2013.

[168] J. Ross *et al.*, "Electrical control of neutral and charged excitons in a monolayer semiconductor," *Nat. Commun.*, vol. 4, p. 1474, 1 2013.

[169] T. Wehling, I. Grigorenko, A. Lichtenstein, and A. Balatsky, "Phonon-mediated tunneling into graphene," *Phys. Rev. Lett.*, vol. 101, p. 216 803, 21 2008.

[170] V. Brar *et al.*, "Observation of carrier-density-dependent many-body effects in graphene via tunneling spectroscopy," *Phys. Rev. Lett.*, vol. 104, p. 036 805, 3 2010.

[171] L Wang *et al.*, "One-dimensional electrical contact to a two-dimensional material," *Science*, vol. 342, no. 6158, pp. 614–617, 2013.

[172] T. Christensen, *From Classical to Quantum Plasmonics in Three and Two Dimensions* (Springer Theses), en. Cham: Springer International Publishing, 2017, ISBN: 978-3-319-48561-4. DOI: 10.1007/978-3-319-48562-1. [Online]. Available: http://link.springer.com/10.1007/978-3-319-48562-1.

Appendix A: Graphene

A.1 Electronic Properties

Reference [172] is a great resource for understanding the optical properties of graphene. We include many of the most useful results here.

The charge carriers that move through graphene are known as "Dirac Fermions". They represent the collective motion of all electrons interfering with one another in such a way that they can be described as quasiparticles with a linear dispersion relation at low energies.

$$\epsilon = \pm \hbar v_F |k|$$

where $k = k_x + ik_y$ is the in-plane momentum. This is the result of taking the eigenvalues of the Dirac Fermion Hamiltonian

$$H = \hbar v_F (\sigma_x k_x + \sigma_y k_y) = \hbar v_F \begin{pmatrix} 0 & k^* \\ k & 0 \end{pmatrix}$$

We can obtain the carrier density $n = n_- - n_+$ from an integral over the density of states

$$n(\mu) = \int_{-\infty}^{\infty} \rho(\epsilon)[f(\epsilon - \mu, T) - f(-\epsilon - \mu, T)]d\epsilon$$

where the first term accounts for negative carriers and the second term accounts for holes. In reality, we only need to take the integral up to a cutoff $\pm 3\gamma_0$, since that is the largest value of energy in the first Brillouin zone.At zero temperature, and assuming linear band structure, the carrier density of graphene can be calculated by counting the number of states available in a circle of radius k_F around the Dirac point

$$N = g_s g_v \frac{\pi k_F^2}{(2\pi/L)^2} \implies n = \frac{k_F^2}{\pi} = \frac{(\epsilon_F/\hbar v_F)^2}{\pi} = \frac{\epsilon_F^2}{\hbar^2 v_F^2 \pi}$$

When $\omega < 2\epsilon_F/\hbar$ and $\omega < \omega_{Oph} \approx 0.2$ eV, the frequency is low enough that scattering time can be estimated from DC measurements τ_{DC}.

$$\tau_{DC} = \mu\frac{\hbar\sqrt{n\pi}}{ev_F} = \mu\frac{\epsilon_F}{ev_F^2}$$

Scattering time can be estimated by inverting the Drude conductivity equation, assuming $\omega\tau \gg 1$

$$\tau(\omega) = \frac{e^2\epsilon_F}{\pi\hbar\omega^2}\frac{1}{\mathrm{Re}\sigma(\omega,0)}$$

[Jablan et al. 2009]

A.2 Optical Properties

The optical conductivity $\overleftrightarrow{\sigma}(q,\omega)$ relates the surface current $\mathbf{K}(\omega)$ to an applied electric field $\mathbf{E}(\omega)$

$$\mathbf{K}(\omega) = \int \overleftrightarrow{\sigma}(q,\omega)\mathbf{E}(\omega)dq$$

Here, ω refers to the frequency and q refers to the scattering wavevector. In many cases, $\overleftrightarrow{\sigma}$ is isotropic, so the above equation can be reduced to a scalar equation

$$K(\omega) = \int \sigma(q,\omega)E(\omega)dq$$

The most general expression for the conductivity is given by the Kubo formula.

$$\sigma(q,\omega) = \frac{ie^2\omega}{q^2}\chi^0(q,\omega)$$

however, it is common to use simpler limiting cases of this expression.

The local conductivity is the one which is most familiar and it relates the surface current to the electric field linearly

$$\mathbf{K}(\omega) = \sigma(\omega)\mathbf{E}$$

It can be found from the nonlocal conductivity by taking the limit $\lim_{q\to 0}\sigma(q,\omega) = \sigma(\omega)$.

The optical properties of graphene are such that they allow for the formation of *plasmons.*[172]

The dispersion relation is the energy as a function of momentum $\omega(q)$. As described in Ref. [172], the TM dispersion relation for any two-dimensional material between two dielectrics can be derived by matching boundary conditions of fields decaying exponentially away from the material. The result is

$$\frac{\epsilon^-}{\sqrt{q^2-\epsilon^-(\omega/c)^2}}+\frac{\epsilon^+}{\sqrt{q^2-\epsilon^+(\omega/c)^2}}=\frac{\sigma(q,\omega)}{i\epsilon_0\omega}$$

where σ is the 2D conductivity. To find the dispersion relation requires numerically solving for ω given q.

At this point, one can choose two viewpoints. On one hand, the frequency ω can be chosen to be real and the wavevector is complex $q=q_1+iq_2$. On the other hand, the wavevector can be chosen to be real $q=q^*$ with the frequency complex $\omega=\omega_1+i\omega_2$. We will usually choose the latter, since we are interested in resonances with finite width.

As described in Ref. [172], we usually solve the dispersion relation in the nonretarded limit $q\gg k_0$ where it is given by

$$\omega=\frac{\sigma(q,\omega)}{2i\epsilon_0\bar{\epsilon}}q$$

Most of the time, σ is complicated, so we have to solve the above equation numerically. That is, given $q=q_1+iq_2$ find the value of ω such that

$$\boxed{1-\frac{\sigma(q,\omega)q}{2i\epsilon_0\bar{\epsilon}\omega}=0}$$

If losses are small ($q_2\ll q_1$), we solve

$$1-\frac{i\mathrm{Im}[\sigma(q,\omega)]}{2i\epsilon_0\bar{\epsilon}\omega}=0$$

Notice that since q is large, this is a highly nonlocal limit. Therefore for large enough q, we must use the nonlocal conductivity. But we can still make some good approximations in the regime of low q_1. Using the intraband approximation for the conductivity, we get

$$\omega = \frac{1}{\hbar}\sqrt{\frac{e^2\epsilon_F}{2\pi\epsilon_0\bar{\epsilon}}q}$$

Appendix B: Fabrication of Tunable Narrowband Infrared Thermal Emitter

Below is a list of tools required for fabrication of the tunable narrowband infrared thermal emitter described in Part II of this thesis.

- WET Spin-rinse-dryer (SRD)
- DEP Metal Evaporator
- CLAS Fiji ALD
- WET Solvent Bench
- FURN Reflectometer
- DEP Profilometer
- PKG DISCO Dicing saw
- ETCH PECVD
- CLAS E-Beam Spin Bench
- CLAS E-Beam Develop Bench
- EBL Electron beam lithography tool

Below is the full step-by-step procedure for creating the tunable narrowband infrared thermal emitter.

1. Obtain a 4" Si(100) wafer and clean it in the SRD
2. In Metal Evaporator, deposit the backreflector on the wafer
   (a) 2 nm of Ti at 0.2 Å/ s as an adhesion layer to the Si wafer
   (b) 150 nm of Au at 2.0 Å/ s as the backreflector itself
   (c) 2 nm of Ti at 0.2 Å/ s as an adhesion layer to the next layer
3. Deposit initial sublayers of the spacer layer
   (a) In ALD, deposit 10 nm (96 cycles) of thermal Al_2O_3

(b) In PECVD, deposit SiO_2 using *Si Oxide* recipe in the PECVD (810 sccm N_2O // 440 sccm 2% silane // RF Power: 36 W // Temperature: 250 C). Deposition rate is reported at 66 nm/min, but was measured to be 58 nm/min.

4. Dice wafer
   (a) Spin photoresist S1813 onto wafer
      i. Set hotplate to 115° C. Perform a dehydration bake once temperature reaches 100°
      ii. Deposit S1813 and spin at 4000 RPM (Recipe 9 at the time of this writing)
      iii. Bake at 115°C for 60 seconds
   (b) Dice in Disco Dicing Saw
   (c) At Liftoff Bench, strip photoresist
      i. Remove undesired edge pieces
      ii. Fill beakers with acetone and IPA
      iii. Remove a chip from mylar and drop in acetone for 10 seconds
      iv. Spray with acetone while moving chip from acetone to IPA
      v. Agitate chip in IPA
      vi. Remove and spray with N_2 until dry
5. On Reflectometer, measure SiO_2 thickness of each die
   (a) Turn on Reflectometer light and allow 20 minutes to warm up
   (b) Choose material stack *SiO_2 on Au*. Do not include the 10 nm of Al_2O_3, as it is optically insignificant.
   (c) Ensure fit parameters are correct, namely that the starting point for the SiO_2 thickness is roughly what is expected
   (d) Measure SiO_2 thickness of each chip
6. In RIE, etch spacer to target thickness using recipe *50CHF3* with the carbon platen. Etch rate is roughly 25 nm/min.
7. In ALD, deposit spacer capping layer of thermal Al_2O_3
8. Transfer a 5 mm x 7 mm sample of graphene to the die
9. Deposit Au bondpads
   (a) Obtain a hard mask and mask off the middle two columns of holes
   (b) Place sample on stage and tape the edges with kapton tape
   (c) Place the hard mask on the tape taking care to align the holes to be on the outer edges of the graphene. The tape will keep the mask lifted off the graphene.
   (d) Insert sample along with sources of Ti and Au
   (e) Evaporate 2 nm Ti
   (f) Evaporate 100 nm Au
   (g) Vent and remove items from chamber
10. Deposit protective hafnia layer on the graphene

(a) In Metal Evaporator, deposit Hf seed layer. Typical parameters are 90 mA current and 0.1 Å/s deposition rate.

(b) In ALD, deposit 5 nm (50 layers) thermal HfO_2

11. Electron Beam Lithography

(a) Spin HSQ/PMMA

i. Set hot plate to 180°C
ii. Spin PMMA 950 at 1500 RPM for 1 min
iii. Bake sample for 1 minute
iv. Allow to cool for 1 minute
v. Spin HSQ at 3000 RPM for 1 min

(b) Pattern on the EBL

(c) Develop the HSQ

i. 90 s in MF321
ii. 30 s in DI Water
iii. Rinse with IPA. Do not dunk, only spray

(d) In RIE, etch PMMA using recipe *50_10_10*. Etch rate is roughly 60 nm/min.

12. In Metal Evaporator, deposit Si grating

(a) Load sample onto sample holder and load sample holder into vacuum

(b) Place 16 copper wafer blanks on top of the sample holder as a thermal mass

(c) Pump down

(d) Deposit the Si at the highest rate possible (¡3.0 Å/s). This reduces the amount of "on" time so the sample doesn't get too hot

(e) Wait at least 30 minutes to cool. The Si will be highly strained and venting too early can quench it causing it wrinkle and buckle

(f) Vent

(g) Measure Si thickness in the profilometer

13. Lift off the Si

Appendix C: Emission Chamber Polarization

When operating in emission mode in the main chamber of the FTIR, the detector measures radiation emitted from the sample placed in the chamber. This radiation passes through the transmission mode optics and through the polarizer if one is present in the microscope. The relative orientation of polarizations between the chamber and the microscope was initially unknown.

In order to find the polarization offset ϕ an experiment was performed. A sample of carbon nanotubes was placed on a 200° C heating stage to act as a blackbody. Simulataneously, a polarizer was stood at the exit port of the main chamber with its orientation set to 90°. In this configuration, all radiation emitted from the chamber into the optics beyond was known to be vertically polarized. A second polarizer was placed in the microscope for calibration.

In the measurement software, the total emission amplitude can be measured. By rotating the microscope polarizer relative to the chamber polarizer, we can determine the polarization offset ϕ. The microscope polarizer was rotated every 15° for two full rotations of the polarizer while monitoring the total amplitude of the emission from the blackbody. Once the data was collected, it was fit to the function $a\cos^2(\theta + \phi)$ with $a = 773$ and $\phi = 37°$. This indicates that rotating the polarizer to 37° (127°) will view vertical (horizontal) polarization.

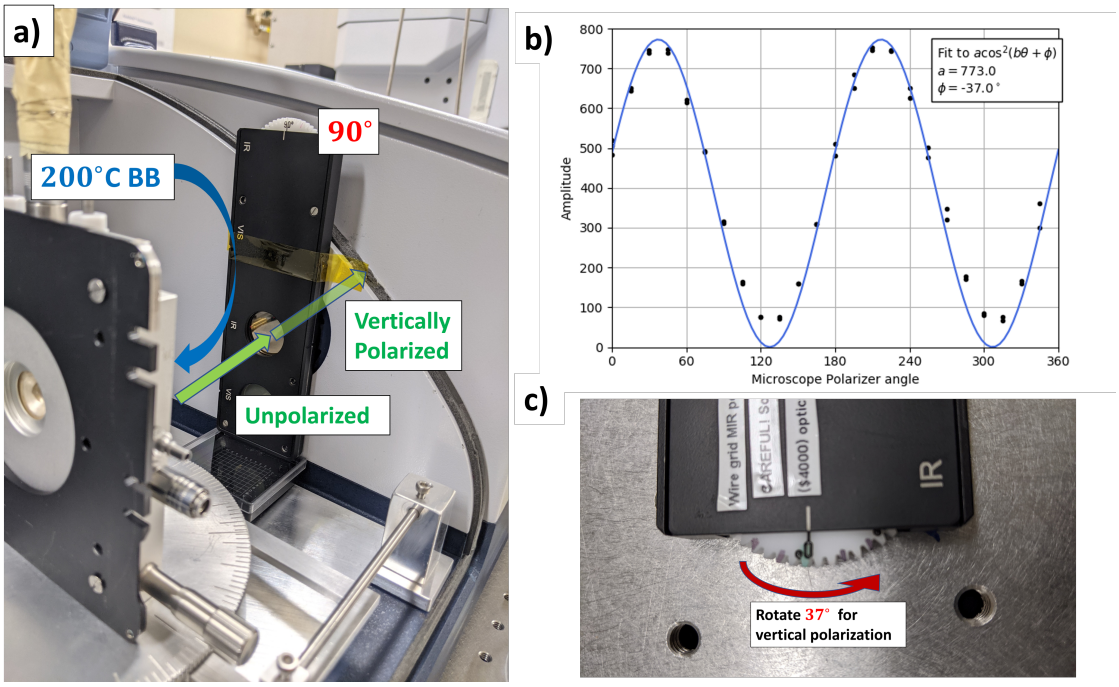

Figure C.1: a) Experimental setup. b) Total emission amplitude of a 200° C CNT sample as a function of microscope polarizer angle. A fit revealed the sample is maximized at $\theta = 37°$. c) The polarizer must be rotated 37° counter-clockwise to measure vertical polarization.